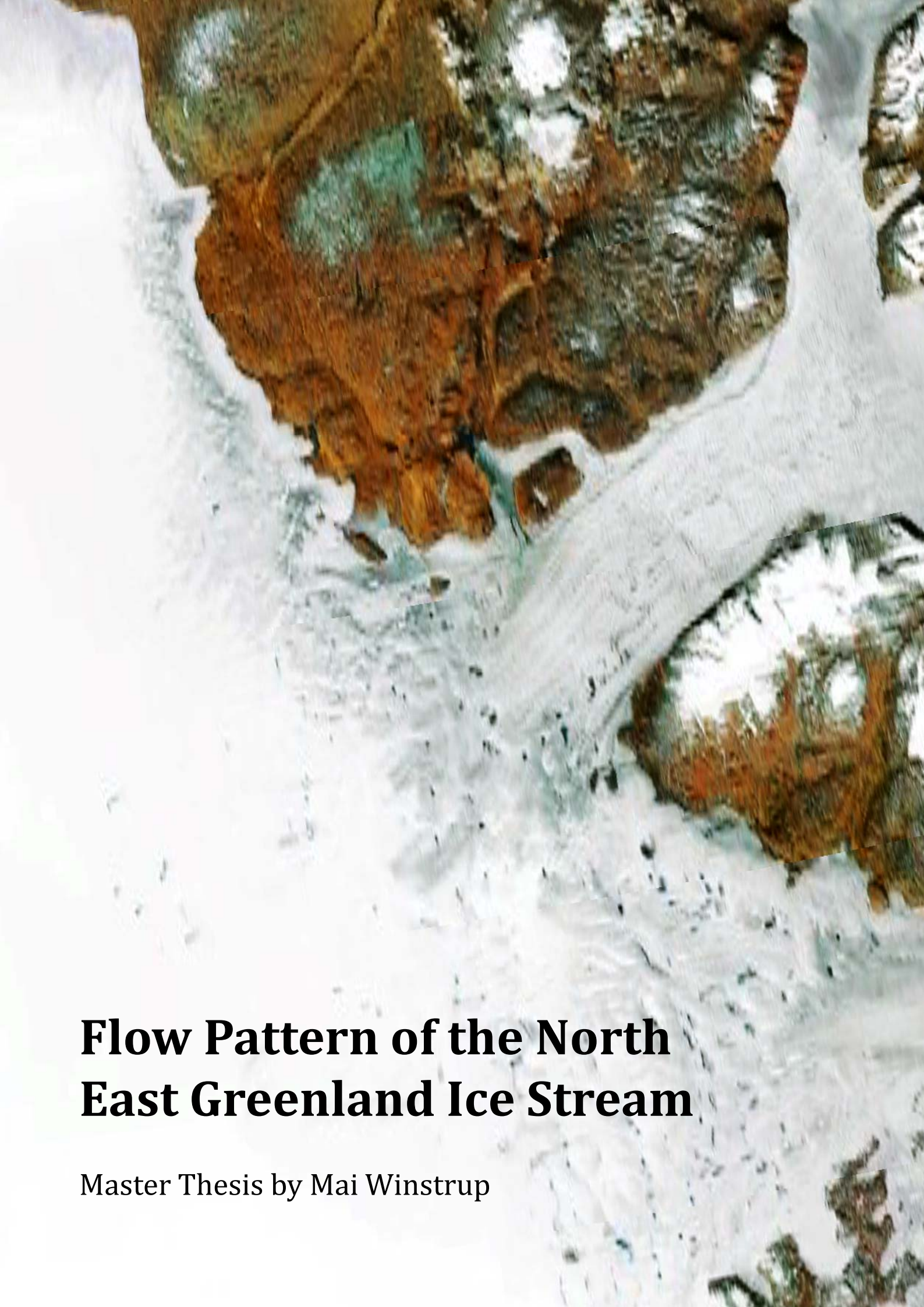

Flow Pattern of the North East Greenland Ice Stream

Master Thesis by Mai Winstrup

Front Cover: *Aerial photo of the marginal parts of the North East Greenland Ice Stream (Google Earth).*

Flow pattern of the North East Greenland Ice Stream

Master Thesis by
Mai Winstrup

Centre for Ice and Climate
Niels Bohr Institute
University of Copenhagen
Denmark

March 2008

Supervisor:
Christine Schøtt Hvidberg

Acknowledgements

First and foremost, I am grateful for the numerous stimulating discussions and helpful suggestions from Claus Nielsen, who has been a tremendous support throughout the work. I also wish to thank my supervisor, Christine Hvidberg, for fruitful ideas of how to tackle many different problems which occurred throughout the project. I am indebted to Hans Christian Steen-Larsen for a lot of helpful discussions on different aspects of Monte Carlo theory, and to Asbjørn Persson, who suggested many improvements to the manuscript. Furthermore, I would like to thank Ian Joughin, who provided surface velocity data from around the North East Greenland Ice Stream. Finally, I wish to thank my family for all their support and their interest in the progress of my work.

The work has been carried out at Centre for Ice and Climate at the Niels Bohr Institute, University of Copenhagen.

Mai Winstrup,
Copenhagen, March 2008

Dansk resumé

På detaljerede højdekort over Grønlands Indlandsis kan man se en markant vifteformet struktur, som strækker sig hele vejen fra den centrale del af iskappen ud til dens nordøstlige rand. Dette er den Nord Øst Grønlandske Isstrøm, der dræner en stor del af den grønlandske iskappe.

Ved hjælp af radio-ekko-data fra Kansas' is-gennemtrængende radar har vi dannet et profil af den indre lagdeling i isen langs med den Nord Øst Grønlandske Isstrøm. Hvert lag i profilet er en isokron, og lagene blev fulgt hen til NorthGRIP iskernen i Nordgrønland for at opnå en præcis datering af lagene. En simpel flydemodel blev herefter benyttet til at estimere akkumulationsrater, bundsmeltning og ændringer i flydemønsteret langs profilet ved hjælp af en Monte Carlo analyse. Resultatet var et bemærkelsesværdigt mønster af store og meget lokaliserede smelterater, som muligvis kan tilskrives lokale geotermiske varmekilder. Effekten af bundsmelting og bundtopografi på isstrømmens dynamik bliver diskuteret. Det er nødvendigt med en bedre forståelse af de fysiske processer, der kontrollerer flydemønsteret i isstrømme, for at disse kan inkorporeres i de nuværende isflydemodeller.

Abstract

A characteristic feature on surface elevation maps of the Greenland Ice Sheet is a large fan-like depression, which extends from the central part of the ice sheet and broadens symmetrically towards the north east. This feature is due to the North East Greenland Ice Stream, which is draining the inner part of the ice sheet into outlet glaciers at the margin.

By use of radio-echo data obtained by the Kansas ice-penetrating radar, we have composed a profile of the internal layering of the ice along the North East Greenland Ice Stream from Central Greenland to the ice fiord. Each layer in the profile is an isochrone, and the layers were traced to the NorthGRIP drilling site in Northern Greenland to obtain an accurate dating of the layers. A simple flow model was then used to estimate accumulation rate, basal melting and changes in flow pattern along the profile by a Monte Carlo analysis. A peculiar pattern of localized large basal melt rates was found, which may be attributed local geothermal heat sources. The effect of basal melting and basal topography on the dynamics of the ice stream is discussed. A better understanding of the physical processes controlling the behaviour of such ice streams might offer the possibility for future incorporation of the dynamics of ice streams into current ice sheet models.

Contents

Chapter 1

Introduction

During recent years, increasing attention has been drawn to the fact that we are living in a world with a changing climate. The Greenland and Antarctic ice sheets are playing a major role in the scientific as well as the public debate of global warming, both due to their significant influence on the Earth's climate system and due to their impact on future sea level rise.

Along with the increase in average temperature of the Earth, the global sea level has risen with an increasing trend during the last century. During the time period from 1993 to 2003, sea level rose with 3.1 mm per year (*Bindoff et al., 2007, p. 387*). About half the sea level rise is attributed the thermal expansion of the oceans, while the rest is due mainly to increased mass loss from mountain glaciers and ice caps.

The mass balance of the two large ice sheets in Greenland and Antarctica, which contain 70% of the world's freshwater resources, is essential when trying to predict future sea level rise. But whereas the mass balance of glaciers and small ice caps outside Greenland and Antarctica is relatively well-known (and in general negative), the current mass balance of the Greenland and Antarctic ice sheets is unclear. However, the latest investigations indicate that both of these large ice sheets exhibit a negative mass balance, although with a large variability on a yearly basis. According to the IPCC (Intergovernmental Panel on Climate Change), it is very likely that they each contributed with approximately 0.2 mm/yr to the global sea level rise in the period from 1993 to 2003 (*Lemke et al., 2007, p. 339*).

It is unknown how fast the large ice sheets in Greenland and Antarctica respond to climate changes. Many of the governing processes have response times of up to several tens of thousands of years due to the way a change at the surface only slowly propagates down into the ice, gradually affecting the flow pattern. Ice sheet models suggest that the inner part of the Greenland and Antarctic ice sheets are still adjusting

to the mass balance changes that occurred at the transition from the last glacial to the present interglacial. But evidence has mounted that has challenged the traditional view of the large ice sheets only responding slowly to climate changes.

Fast flowing outlet glaciers and ice streams have the possibility to speed up the process significantly. Ice streams can be depicted as the arteries of an ice sheet, as they are able to conduct mass over large distances within a relatively short period of time. Because of the vast amount of ice they carry, they play a major role in the discharge of ice from the ice sheet, and a climate-induced change in their efficiency is one possible mechanism by which ice sheets can quickly affect global sea level. They hence make the ice sheets much more vulnerable to the present changes in global temperature than previously thought.

The IPCC report states that the global sea level probably will have risen with somewhere between 18 and 59 cm before the year 2100 (compared to 1980) (*Meehl et al., 2007, p.750*). However, in this prediction the potentially large impact from the Greenland and Antarctic ice sheets is not even taken into account! Current ice sheet models are not able to adequately predict the mass discharge from these due to a lack in our understanding of the dynamics of fast ice flow in ice streams and outlet glaciers. Consequently, the modelled ice sheets are unable to respond as fast to climate changes as what is actually observed (*Lemke et al., 2007, p. 361*). This implies that the future sea level rise estimated by the IPCC may be greatly underestimated.

As we strive to better understand the present state and dynamics of the ice sheets, better knowledge of the dynamics of ice stream flow is of vital importance. Only with an improved understanding of the governing processes in these will ice sheet models be able to predict the future impact of the increasing temperatures on the Greenland and Antarctic ice sheets.

This thesis attempts to improve our understanding of the driving dynamics behind the North East Greenland Ice Stream, which is likely to play a major role in the discharge of the Greenland Ice Sheet. This is accomplished in two ways, firstly by an analysis of some of the existing data from the area, and secondly by employing an inverse method to obtain an estimate of the flow parameters along the ice stream.

Chapter 2

The North East Greenland Ice Stream

An ice stream is a region of an ice sheet where the ice flows significantly faster than in the surrounding areas. Strictly speaking, an ice stream has no visible rock boundaries, like an outlet glacier does, but in practice the two terms are often used interchangeably. Jakobshavn Isbræ, for instance, starts out as an ice stream and terminates as an outlet glacier. Ice streams are sizeable elongated features which may stretch for hundreds of kilometres. Typical ice stream velocities are above 100 m/yr, at least one order of magnitude greater than the surrounding ice.

While ice streams are relatively abundant on the Antarctic ice sheet, only two major ice streams exist in Greenland. These are Jakobshavn Isbræ and the North East Greenland Ice Stream. Jakobshavn Isbræ is situated in the western part of Greenland (see map in figure 2.1 A) and has by far the largest surface velocities, reaching more than 12.6 km/yr, i.e. almost 35 m/day (*Joughin et al., 2004*). It alone is estimated to drain about 7% of the Greenland Ice Sheet *(Rignot and Kanagaratnam, 2006*). The North East Greenland Ice Stream (in the following often shortened the NEGIS) is believed to drain approximately 15% of the Greenland Ice Sheet (*Ekholm et al., 1998*). But while the Jakobshavn Isbræ has been extensively studied, not much is known about the NEGIS, which was only discovered recently.

The existence of the North East Greenland Ice Stream was first observed by Fahnestock in 1993 (*Fahnestock et al., 1993*). Its discovery was due to the increasing number of satellite images (SAR images), which revealed a distinct feature in the north eastern part of Greenland with much higher local relief than the rest of the region, reduced ice thickness and different snowpack properties. The enhanced surface topography as well as the distinct edges of the feature proposed it to be dynamically generated by enhanced ice flow.

On present-day high-resolution maps of the topography of the Greenland Ice Sheet, like those in figure 2.1, the existence of the North East Greenland Ice Stream is apparent. It is a nearly straight fan-like depression, which originates in the central part of the ice sheet and broadens symmetrically towards the north eastern margin, feeding the Zachariæ Isstrøm, Nioghalvfjerdsfjorden and Storstrømmen outlet glaciers. It is more than 700 km long, and expands from an initial width of 15 km to a width of more than 60 km close to the coast.

As the NEGIS plays a major role for the drainage of the Greenland Ice Sheet, the processes governing this ice stream may be very important for predicting how the Greenland Ice Sheet will evolve during the coming years.

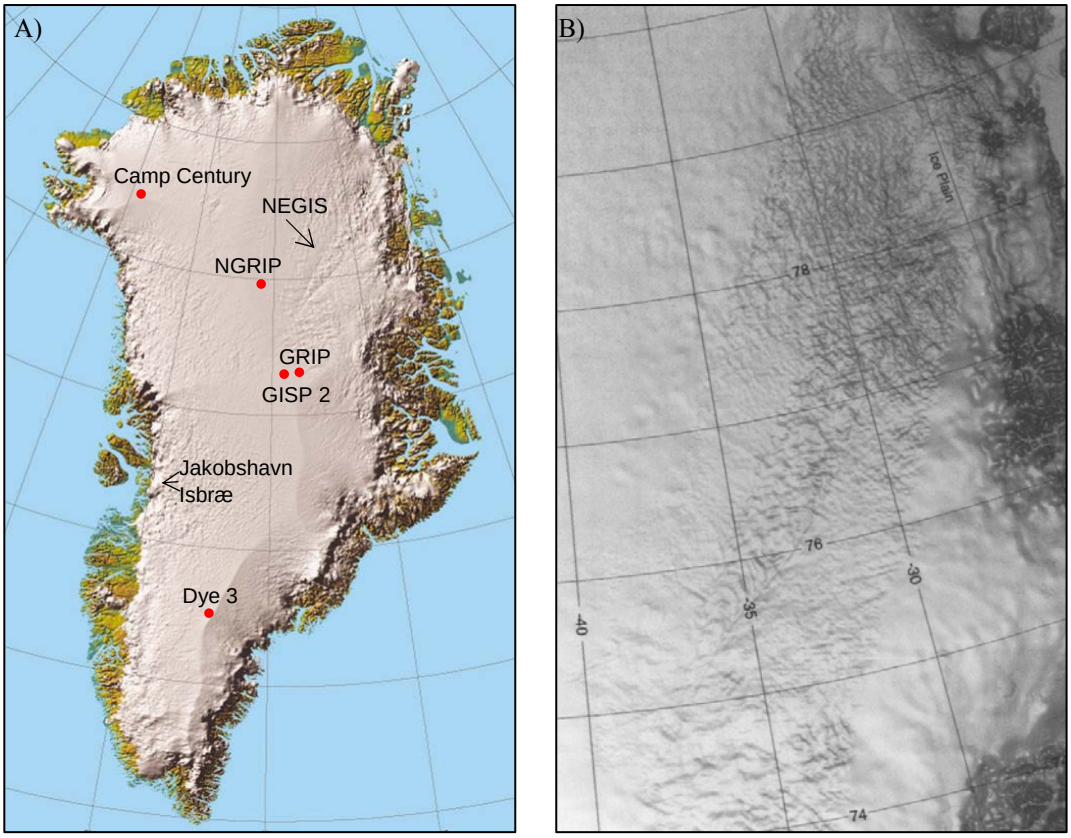

Figure 2.1: **A)** A shaded surface of the digital elevation model for Greenland. The locations of the North East Greenland Ice Stream and Jakobshavn Isbræ are marked. Also shown are the locations of major ice core drill sites. The North East Greenland Ice Stream originates less than 100 km away from the NorthGRIP drill site. Map by S. Ekholm, Danish National Survey and Cadastre. **B)** A close-up of the surface topography in the area around the North East Greenland Ice Stream. Map from *Ekholm, 1996*.

Chapter 3

Processes governing enhanced flow

3.1. Mechanisms of glacier flow

Glacier flow basically occurs through two mechanisms: Internal deformation of the ice and ice flow at the ice-bedrock interface. The latter is either due to sliding over the bedrock or deformation of the underlying geological substrate. The relative importance of these mechanisms depends on the given circumstances.

3.1.1. Internal deformation of ice

The mechanism so far best understood is the internal deformation of ice. As ice is a visco-plastic material, it gradually transforms under the influence of its own weight. It does so mainly by a process called creeping, which comprises of movement within the different ice crystals, movement and rotation of the crystals relative to each other, crystal growth, and dynamic recrystallization (*Paterson, 2001, p. 81*). The internal deformation rate is greatest close to the bed.

From numerous experiments, a flow law has been developed to deal with the deformation of glacier ice in response to the internal stress field. For the simplified case of simple shear, Glen's flow law relates the shear strain rate, $\dot{\varepsilon}_{ij}$, to the shear stress, τ_{ij}, in the following way:

$$\dot{\varepsilon}_{ij} = A\tau_{ij}^{n}, \qquad i,j \in \{x,y,z\}$$

In this equation, A is a constant, which amongst other factors depends on the temperature, crystal orientation and the impurity content of the ice, and n is usually taken to be equal to 3. Due to the temperature dependence of A, the deformation of glacier ice depends on its temperature. The warmer the ice, the more rapidly it flows. In general, increased impurity content also acts to increase the deformation rate.

By use of Glen's flow law, it is possible to obtain an expression for the surface velocity of the glacier or ice sheet. In case of deformation by simple shear and isotherm ice, the surface velocity is proportional to the fourth power of the ice thickness (*Paterson, 2001, p. 251*), which makes ice thickness a very important factor for ice flow due to internal deformation.

Where the temperature of the basal ice is below the pressure-melting point, internal deformation of the ice is by far the dominating process of glacier flow.

3.1.2. Basal motion

Ice is also able to move by ice flow at the bed. Basal motion is only important for glacier flow where the bottommost ice is at the pressure-melting point. Ice below the pressure-melting point adheres to the ground, which renders basal motion much more difficult.

When dealing with ice at the pressure-melting point, the bedrock will be covered by a thin film of water, which reduces the basal friction and may cause a decoupling of the ice sheet from the underlying geological substrate. This may allow the ice to slide column-wise over the bedrock, and hence speed up the flow velocities significantly. Basal sliding of ice at the pressure-melting point can also be accomplished by regelation flow and enhanced plastic flow (*Weertman, 1957*). In small glaciers, basal sliding often accounts for about half the ice flow (*Paterson, 2001, p. 135*).

In case of a sedimentary bed, also deformation of the sediments may give rise to high rates of basal flow. A layer of subglacial sediments, till, is often revealed beneath a retreating glacier, indicating that sedimentary beds are common. This till can potentially be very important for the ice flow, as it under certain circumstances is able to deform under the stimulus of much lower stresses than the ice. Observations have shown that deformation in a thin layer of till in some cases may be responsible for 90% of the glacier movement (*Paterson, 2001, p. 158*).

The subglacial processes governing enhanced basal flow are in many ways still unclear. Consequently, no consensus has yet emerged concerning the relative importance for ice flow of sliding along the ice-bed interface as opposed to the deformation of sediments.

3.1.3. Basal water: Impact and formation

Both basal sliding and deformation of basal sediments are promoted by the occurrence of water at the bed. High subglacial water pressure reduces the basal friction, enabling the ice sheet to decouple much more easily from the substrate, as

well as it is able to soften any underlying sediments, thereby making them more vulnerable to deformation. In fact, subglacial till is only able to deform appreciably if it is water saturated and maintains a high pore-water pressure (*Paterson, 2001, p. 159*).

While flow velocities caused by internal deformation of glacier ice typically is far below 100 m/yr, a lubricating layer of basal water may cause horizontal velocities of several km/yr (*van der Veen, 2007*). Hence, the supply and storage of water at the base of the ice sheet is of vital importance for the ice flow.

3.1.3.1. In situ formation of water

Melting of ice from the base of the ice sheet is one way by which water can be formed at the bed. Whether basal melting is possible at a specific location depends on the amount of available energy as well as the overburden pressure, which acts to lower the melting point temperature.

To a large extent, the available energy at the base of an ice sheet is due to geothermal heat, originating from deep within the interior of the Earth. As glacier ice is an excellent thermal insulator, the geothermal heat only slowly dissipates through the ice. The heat generated at the glacier bed is primarily used for warming the basal ice, and basal melting will occur if the pressure-melting point is reached. Basal melt water formed by an average geothermal heat flux amounts to several mm/yr (*Paterson, 2001, p.112*). Much larger melt rates are possible in geothermally active areas.

Where the sliding velocity is above 20 m/yr, frictional heat from sliding may also give rise to melt rates of several mm/yr (*Paterson, 2001, p.112*). Strain heating in areas with high strain rates is able to contribute even more significantly to the basal melting of ice. At Jakobshavn Isbræ, very high rates of deformation in a thick layer of temperate ice are believed to produce melt rates in excess of 0.5 m/yr (*Truffer and Echelmeyer, 2003*).

3.1.3.2. Water transportation

Water transported from the surroundings, either from the surrounding bed or from within the ice sheet, also acts to increase the amount of basal water in a specific area. The direction of water motion is primarily determined by the potential gradient caused by gravity. If the surface and bedrock slopes are comparable in magnitude, the water flows in direction of the largest surface slope. But where the surface is relatively flat, the importance of the bedrock slope increases, and the water preferentially follows the valley floors (*Paterson, 2001, p. 114*).

When the water flows over the bed, it may come across an area where the conditions no longer are to keep the water unfrozen, and it may freeze to the base of the ice sheet at a very different location than where it was formed. This can e.g. be envisioned to be the case when melt water flows towards the edge of the ice sheet, where it encounters a much smaller ice thickness. The associated lower basal temperature may not be sufficient to keep the water liquid, and the water will refreeze.

3.1.3.3. Surface melt water

Until recently, percolating water from surface melt was believed to refreeze in the upper, cold reaches of the large ice sheets. However, new observations by Zwally et al. (*Zwally et al., 2002*) have radically altered this view. At a location where the ice thickness exceeds 1200 m, they observed a speed-up of the flow velocities of the Greenland Ice Sheet initiating a couple of weeks after the commencement of the melt season, and ending simultaneously with the end of the melt season. Apparently, surface melt water was able to very quickly penetrate to the base of the ice sheet, where it acted to facilitate the basal flow.

Transportation of surface melt water to the base of the ice sheet provides a direct mechanism by which the ice sheet is able to rapidly respond to a climatic forcing. Surface melting occurs over more than 50% of the Greenland Ice Sheet, and with the rising summer temperatures, this area is increasing (*Mote, 2007*). However, it has not yet been proven whether the rapid migration of melt water to the bed is a widespread phenomenon.

3.1.4. Impact of bedrock geology

Basal geology also exerts a large influence on the ice flow. One of the major issues is whether the bed consists of consolidated hard rock or sediments. As already mentioned, a sedimentary substrate may deform, and does most prominently so when water saturated. Different geological substrates have different resistance to deformation and different degrees of porosity and permeability. A permeable substrate at the bed is able to remove water from the ice-bedrock interface by causing the water to drain away through the pore space of the sediments instead, hence decreasing the opportunities for basal motion.

Bedrock geology also has implications for the geothermal heat flux in the area. Factors influencing the geothermal heat flux are e.g. the occurrence of volcanic activity, the crustal thickness and the presence of radiogenic sources in the crust (*van der Veen et al., 2007*).

Due to the inaccessibility of the bedrock upon which the Greenland and Antarctic ice sheets rest, comprehensive data on their geologies (sediment properties, groundwater drainages etc.) is lacking. Nor is the magnitude and variation of the geothermal heat flux over the bedrock very well determined. A typical value for an old Precambrian shield, like the one Greenland is resting upon, is 42 mW/m^2 (*Huybrechts, 1996*). However, recent research suggests the presence of much larger geothermal heat fluxes in some areas in Central Greenland (*Fahnestock et al., 2001a*; *Dahl-Jensen et al, 2003*).

3.1.5. Impact of bedrock topography

Ice flowing over the bed is of course highly influenced by the bedrock topography. The vital importance of bedrock topography also for the onset of rapid flow can be appreciated from the fact that many of the outlet glaciers of the Greenland Ice Sheet overlie deep and narrow trenches in the bedrock. Jakobshavn Isbræ is situated in an only 6 km wide trough, incised 1500 m into the surrounding bedrock (*Clarke and Echelmeyer, 1996*). It is strongly believed that the presence of this narrow trench causes the onset of the ice stream.

Bedrock topography affects the ice flow in a variety of ways. The centimetre-scale roughness of the terrain influences the amount of sliding, as a smooth bed offers the least friction (*Paterson, 2001, p. 156*). Basal roughness on a larger scale influences the longitudinal stress gradients in the ice, and hence the ice flow by internal deformation. On an even larger scale, the basal topography determines the spatial pattern of ice flow. The largest velocities are recorded where glaciers are pushed through a mountain valley by the pressure of the ice sheet behind. Also, as mentioned in section 3.1.3.2, water flows in direction of the least gravitational potential, which often happens to be towards the bedrock valleys, thereby lubricating these areas.

The basal topography also changes the thickness of the ice, and a greater ice thickness increases the internal deformation rate. It also enhances the opportunities for basal motion as it lowers the pressure-melting point as well as increases the basal temperatures due to the insulating effect of the thicker ice. As a consequence, very favourable conditions for fast flow exist in bedrock valleys.

As an example, the canyon beneath Jakobshavn Isbræ gives rise to ice thicknesses of almost 2700 m. It is believed to have a 400 m thick layer of ice at the pressure-melting point at the base (*Iken et al., 1993*), and the large velocity of the ice stream is mainly attributed enhanced deformation in this basal layer (*Truffer et al., 2003*).

Another impact of bedrock topography is that the geothermal heat flux intensifies in valleys and diminishes on mountains (*van der Veen et al., 2007*). How much the geothermal heat flux is increased in a valley depends on the width of the valley and the steepness of the valley walls. When the trough is deep and narrow, the increase in heat flux is pronounced. Van der Veen estimates that a narrow trench like the one below Jakobshavn Isbræ may increase the local geothermal heat flux by as much as 100% (*van der Veen et al., 2007*). The increased geothermal heat flux will cause higher basal temperatures, or, if the ice is at the pressure melting point, increase the basal melt rates.

Over long timescales, this relation between the geothermal heat flux and basal topography is potentially a vital feedback mechanism, which acts to gather fast ice flow as well-defined features. Numerical models suggest that an initially rather modest basal depression may develop into a deep trench, as the surrounding bedrock is uplifted due to the greater ice load in the depression (*Oerlemans, 1984*). The resulting increase in heat flow in the deepened trench facilitates the ice flow, which in turn results in enhanced erosion and a further deepening of the trench.

Another positive feedback mechanism is due to the heat generated by internal deformation of the ice. Warm ice deforms more easily and hence flows faster. And the faster the ice flows, the more heat is generated, further increasing the temperatures and the deformation rates. Frictional heat provides an additional feedback mechanism, as its production also increases in areas with fast flow.

3.2. Ice stream flow along the NEGIS

Even though the North East Greenland Ice Stream and Jakobshavn Isbræ are among the main ice streams of the Greenland Ice Sheet, the mechanisms of the enhanced ice flow of the two features seem to be fundamentally different. Morphologically, the NEGIS is much closer to the Siple Coast ice streams in Antarctica, which drain about 1/3 of the West Antarctic Ice Sheet.

The NEGIS is seven times longer than Jakobshavn Isbræ, and has a much larger drainage basin, while being approximately similar in size to the Antarctic ice streams. Furthermore, the manifestation of distinct margins along the NEGIS is in common with several of the Antarctic ice streams. However, several differences are also present. The Siple Coast ice streams are heavily crevassed along most of their margins. The North East Greenland Ice Stream is not. The narrow and well-defined upper segment of the NEGIS is also unique: The onset of rapid flow occurs at one location, far inland and at low velocities. The rapid flow of the Siple Coast ice streams starts at a number of different locations. Also the straightness of the NEGIS is a remarkable feature whose counterpart is not found anywhere else.

3.2.1. The role of bed topography?

Similarly to Jakobshavn Isbræ, the North East Greenland Ice Stream is located along the axis of a fairly deep and well-defined topographic valley. The depth of the valley increases towards the margin, reaching almost 650 m. A shaded relief perspective plot of the valley is shown in figure 3.1 A. Velocity contours are superimposed, from which it is seen that the area of enhanced flow closely follows the trench.

The existence of the topographic valley may have great implications for the ice flow. The trench causes the ice thickness to increase with 15%, and Bamber et al. suggest this increase in ice thickness to be fully responsible for the enhanced flow in the area (*Bamber et al., 2003*). According to Glen's flow law in case of simple shear, an increased thickness of 15% translates into a 75% increase in the surface velocities (see section 3.1.1).

Still, this broad basin along the North East Greenland Ice Stream cannot really be compared to the deep trough carved into the bedrock below Jakobshavn Isbræ. And while it is commonly believed that the fast flow of Jakobshavn Isbræ is caused by the deep trench, it is difficult on basis of the broad topographic basin around the NEGIS to figure out the cause and effect relationship here. Such a broad basin may be responsible for the occurrence of the ice stream, but it may just as well be the result of enhanced erosion due to the presence of the ice stream.

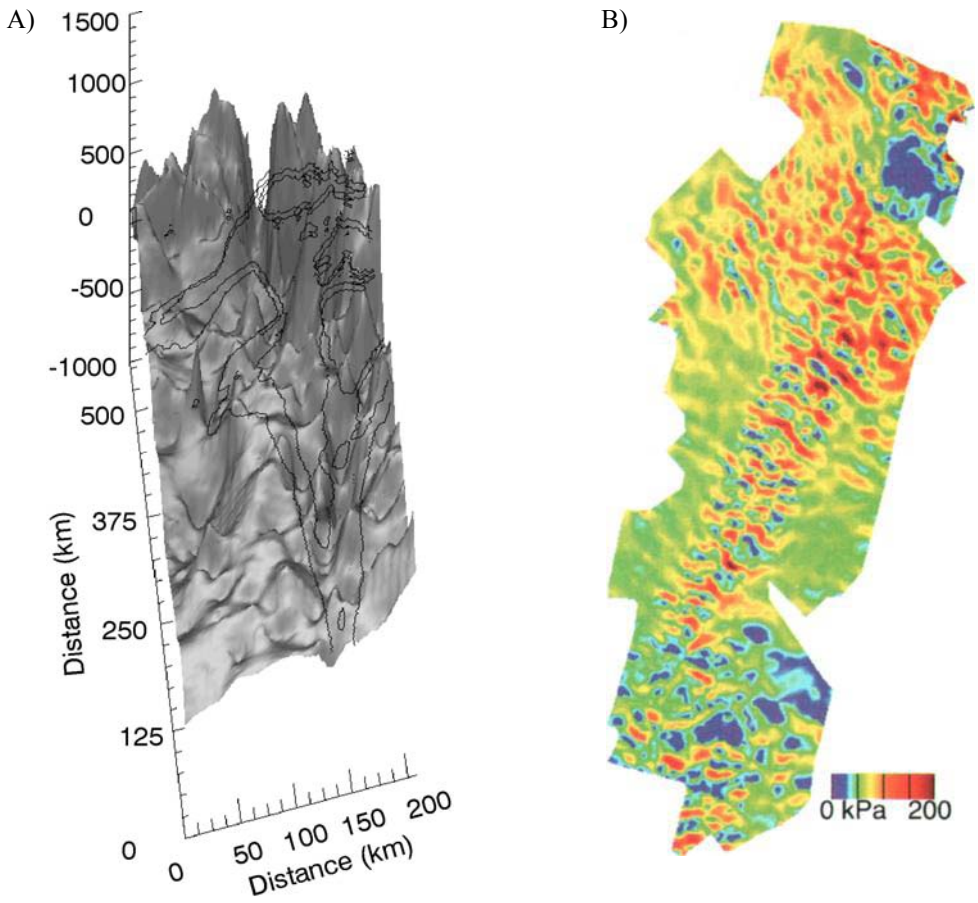

Figure 3.1: A) A shaded relief perspective plot of the valley along the NEGIS. The view is to the north east, i.e. down the trench towards the coast. Superimposed are a few balance velocity contours, indicating the location of the ice stream. Figure from *Bamber et al., 2003*. **B)** A map of the gravitational driving stress in the area around the NEGIS. Figure from *Joughin et al., 2001*.

3.2.2. A sedimentary bed?

From the basal shear stress, it is possible to infer how strongly the ice interacts with the bed in the area, and hence to which degree the ice stream flow is caused by deformation of a weak bed. To a first approximation, the basal shear stress is balanced by the driving stress, which depends on the ice thickness and the slope of the ice sheet surface. A map of the driving stress for the area around the North East Greenland Ice Stream is found in figure 3.1 B.

Along the upper part of the ice stream, the driving stress is around 30 kPa. It generally increases downstream along with the increase in surface velocity. Overlain on this pattern are many small oscillations caused by the undulating bedrock and

surface topography. Relatively close to the margin, and concurrently with a drastic increase in velocity, the driving stress reaches a peak of around 100 kPa, and then suddenly declines to a value of 10-40 kPa. At the same time, the ice sheet surface flattens and forms what may be termed an ice plain.

In general, the driving stress along the upper part of the NEGIS is much higher than the shear stress needed to deform till, and till deformation can hence be excluded as a major flow mechanism here. However, the decrease in driving stress combined with the increase in surface velocity along the very last part of the ice stream is very similar to the variation of driving stress along the Siple Coast ice streams, whose rapid motion is believed to be due to deformation of a thin layer of unconsolidated, saturated marine sediments (*Truffer and Echelmeyer, 2003*). It is therefore likely that the ice stream flow on the ice plain close to the margin is due to a deforming layer of sediments (*Joughin et al., 2001*; *Layberry and Bamber, 2001*).

3.2.3. Occurrence of basal melting?

There is a growing body of evidence of extensive basal melting in the area around the NEGIS, which may be the cause of the rapid flow. The indications arise from a variety of different sources.

3.2.3.1. RES imagery

Due to the different dielectric properties of ice and water, the radio-echo reflection is much smaller from a subglacial ice/bedrock interface as opposed to an ice/water interface. In principle, it is thus possible from the strength of the bedrock reflections to determine the areas where basal melting occurs. In practice, however, the task is quite complex, in particular in Greenland where no subglacial lakes seem to exist.

From an analysis of radio-echo images along the NEGIS, Layberry and Bamber (*Layberry and Bamber, 2001*) suggested basal melting to be very likely throughout the length of the ice stream. However, they were not able to properly account for the attenuation of the radar wave due to the changing ice thickness, and could therefore only give a qualitative guess. But even below the very thick ice upstream of the NEGIS as well as along the upper part of the NEGIS, they found very large reflections indicative of the presence of water. A similar conclusion was reached by Fahnestock et al. (*Fahnestock et al., 2001b*) (see figure 3.2).

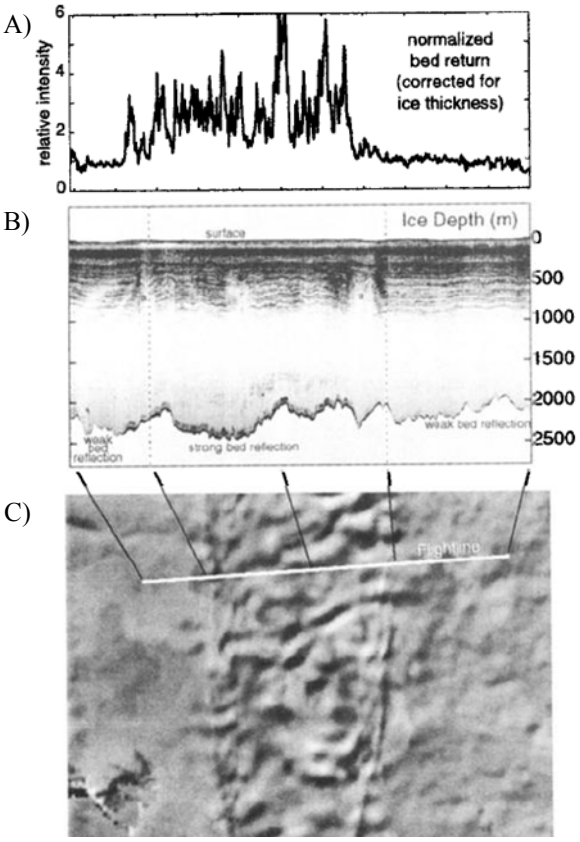

Figure 3.2: A) The relative strength of the bed reflection across the ice stream. A six-fold increase in reflection strength is found beneath the ice stream. **B)** Radio-echo image across the ice stream, from which the data in A are derived. **C)** Location of the radar image shown in B. The margins of the NEGIS are clearly seen. Figure from *Fahnestock et al., 2001b*.

3.2.3.2. Ice core data

Data from the NorthGRIP ice core is another example. The location of the ice core was chosen in order to obtain a full and undisturbed climate history for the Eem period. But while drilling, it was discovered that extensive basal melting took place in the area, and consequently the oldest layers had melted away. The basal melt rate established from the ice core data was 7.5 mm/yr, corresponding to a geothermal heat flux of 120 mW/m^2 (*Dahl-Jensen et al., 2003*).

3.2.3.3. Modelling efforts

Recent modelling of the mass balance along the ice ridge between GRIP and NorthGRIP by use of radio-echo layers (*Buchardt and Dahl-Jensen, 2007*; *Dahl-Jensen et al., 2003*), also predicts large basal melt rates in the area. The obtained melt rates along the ice ridge range from 0.4 to 1.1 cm/yr over a distance of less than 100 km. This corresponds to geothermal heat fluxes of 90 to 160 mW/m^2 (*Dahl-Jensen et al., 2003*).

An area of highly disturbed radio-echo layers is observed in RES images from along the ice ridge, see figure 3.3. This layering can only be explained by the occurrence of very high melt rates of more than 8 cm/yr, corresponding to a geothermal heat flux above 700 mW/m^2 (*D. Dahl-Jensen, pers. comm.*). The location of these strongly undulating layers is close to the origin of the North East Greenland Ice Stream. The onset of the NEGIS may hence be related to an area with very high basal melt rates.

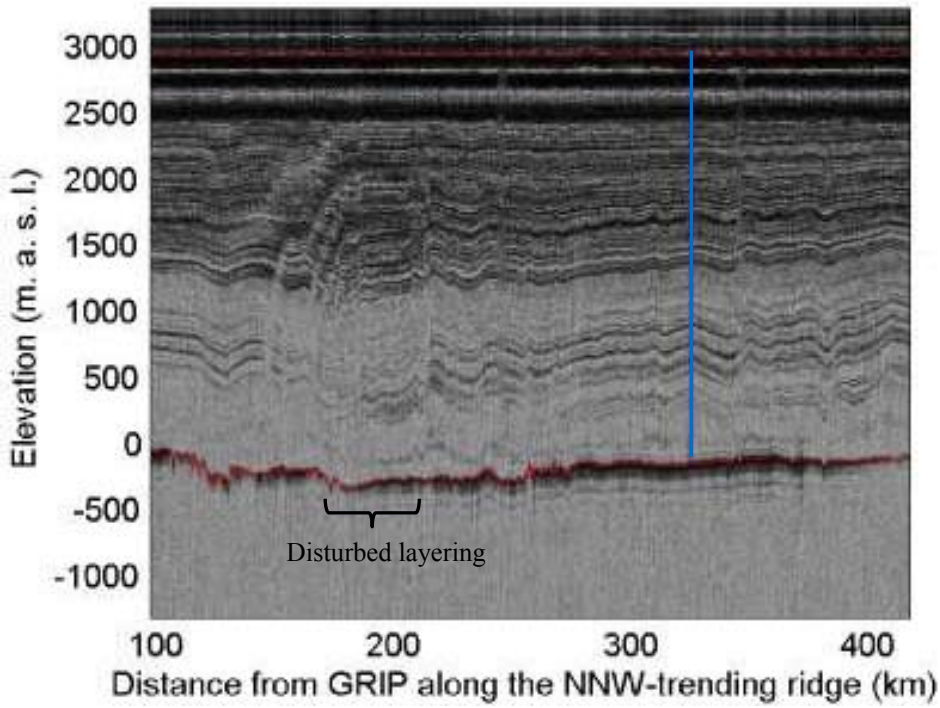

Figure 3.3: Radio-echo image along the ice ridge from GRIP to NGRIP. An area of highly disturbed internal layering is seen around 200 km from GRIP. The location of the NGRIP ice core is indicated with a blue line. Bedrock and surface are marked in red. Figure from Buchardt (*Buchardt, 2005*).

Also an analysis by Fahnestock suggests the presence of large basal melt rates along the North East Greenland Ice Stream (*Fahnestock et al., 2001a*). Employing a very simple one-dimensional model, he calculated the basal melt rates by use of the age-depth relationship expressed in the internal layering. The resulting basal melt rates in the area around the NEGIS are illustrated in figure 3.4. The basal melt rates were found to be above 15 cm/yr along the upper part of the NEGIS, and decreasing, yet still non-negligible, downstream. One can speculate that Fahnestock in his analysis made too many simplifications to determine the correct values for the basal melt rates. Nevertheless, his work is an indication that extensive basal melting does occur in the area around the NEGIS.

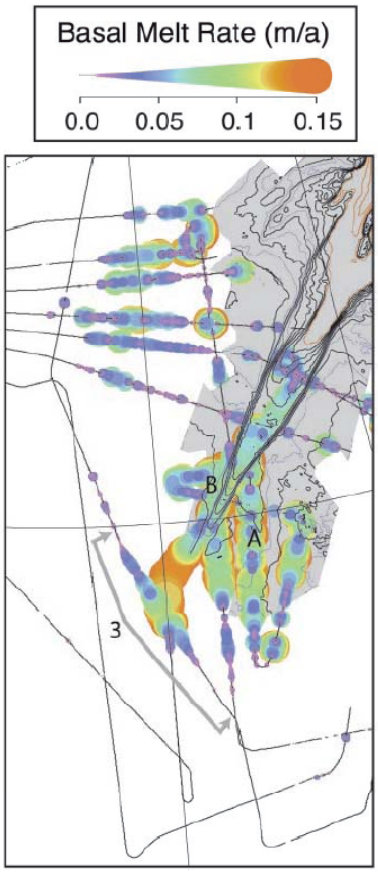

Figure 3.4: Basal melt rates calculated from radio-echo data in the area around the NEGIS. Both colour and size of the circles depend on the calculated melt rates, red and big being the largest. Areas with no or little melting (below 1 cm/yr) are shown with thin black lines. Superimposed are surface velocity contours in order to indicate the location of the ice stream. A denotes the location of the onset of the "southern tributary" to the ice stream (see section 4.3.3), which is found to coincide with an area of large basal melt rates. B is another area found to experience heavy melting. Figure from *Fahnestock et al., 2001*.

The existence of such extremely high melt rates must be caused by geothermal heat fluxes 15-30 times greater than the continental background. The origin of such large geothermal heat fluxes remains unidentified. Dahl-Jensen et al. suggest the reason for the high geothermal heat flux at the NGRIP drill site to be a thin top layer above the bedrock with distinct geological characteristics, and they propose it to be composed of sediments from a dry lake (*Dahl-Jensen et al., 2001*). Fahnestock speculates that volcanism may be an explanation. He bases this conjecture on magnetic anomalies in the area, and on the occurrence of a caldera-like structure on the bed south of the ice stream (*Fahnestock et al., 2001a*). The cutting edge research by Leftwich et al. (*Leftwich et al., 2007*) indicates that a hotspot may exist below the onset region of the North East Greenland Ice Stream. At this location, the Earth's crust seems to be very thin, thus permitting the warm mantle below to heat the ice, and thereby causing the large basal melt rates.

Chapter 4

Data description

4.1. Internal layering of an ice sheet

Since the early 1970s, data from airborne radio-echo sounding (RES) has been collected over large areas of the Greenland Ice Sheet (see figure 4.1). Radio-echo sounding provides us with a unique opportunity to get an insight into the spatial variation of the internal layering throughout the ice sheet. It thus represents an excellent supplement to the data available from ice cores, where the resolution and the abundance of available data may be high, but limited to a specific location. By combining RES imagery with data from ice cores, much information on the dynamics of the ice sheet can be obtained.

4.1.1. Radio-echo sounding

Radio-echo sounding operates through the emission of short pulses of high-frequency radio waves, usually from an airborne radar antenna. At radar frequencies, the dielectric absorption in ice of the electromagnetic energy is low, and glacier ice therefore appears almost transparent. While propagating through the air and subsequently into the ice (and possibly the bedrock), the radar waves are reflected off any boundaries separating media with different dielectric properties. The reflected waves reach a receiving antenna, which records their two-way travel time. From knowledge of the velocity of the radar waves in air (300 $m \cdot \mu s^{-1}$) and in ice (approximately 168 $m \cdot \mu s^{-1}$) (*Hempel et al., 2000*), these travel times can be converted to the depth of the respective boundaries of material with changing dielectric properties. Radar-wave reflecting horizons include the air-ice transition and the ice-bed transition, but internal layers in the ice also create reflections visible in RES imagery.

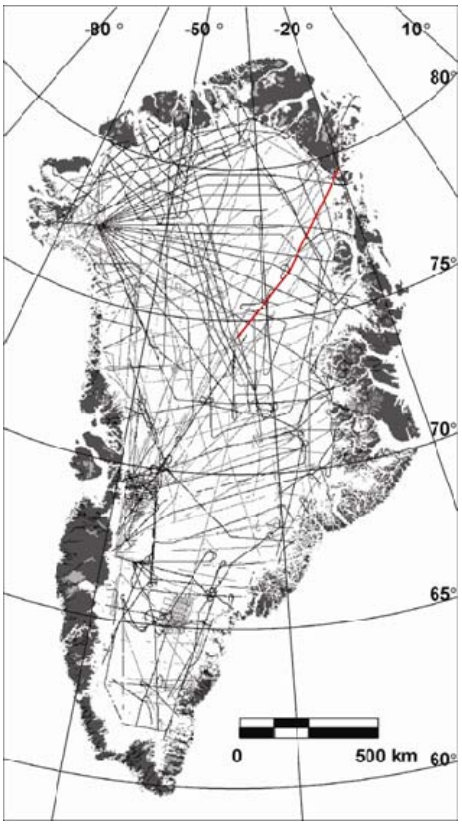

Figure 4.1: Flight-lines over Greenland from which RES data have been collected. The flight-lines shown in grey were flown by the Technical University of Denmark (DTU) in the 1970s, while the flight-lines in black were flown in the 1990s by the University of Kansas. The flight-line along the NEGIS, which we will consider in the following, is shown in red. It consists of three segments of flight-lines flown respectively on May 19 and May 25 1999. Figure from *Bamber et al., 2003*.

When using a constant electromagnetic propagation velocity to calculate the ice thickness and depths of the internal layers, these are underestimated due to higher velocities in the firn layer. By comparing the derived thickness with known ice thicknesses at ice core locations, it is possible to assert the magnitude of the firn correction. At the NGRIP drill site, the difference in thickness is found to be 12.5 m. This fits very well the figure of 10 m often mentioned in the literature to apply for Central Greenland (e.g. *Bogorodsky et al., 1985*; *Gogineni et al., 2001*).

The radio echogram used here was flown by the University of Kansas. Their depth-penetrating radio-echo sounding radar operates at a frequency of 150 MHz, and is capable of penetrating ice thicknesses of more than 4 km with a vertical resolution of 4.5 m (*Gogineni et al., 2001*). The average pixel size along the track is approximately 160 m.

4.1.2. Causes of the internal reflections

As a radio wave reflects off any boundary of dielectric contrast, the origin of the internal layering of the ice observed in radio-echo imagery must be due to dielectric boundaries within the ice sheet interior. The cause of these changes in dielectric

properties of the ice has been investigated by a number of researchers, and several explanations have been proposed.

Changes in ice density (due to ice lenses etc.) are believed to be responsible for some of the observed layers in the upper part of the ice sheet. However, density contrasts between adjacent layers are rapidly diminishing with depth, and once the densification process of firn into glacier ice has completed, only small fluctuations in density occur. These are not expected to be large enough to explain the reflections from the deep internal layers (e.g. *Millar, 1981*; *Fujita & Mae, 1994*).

From borehole measurements, it has been established that many of the deep reflectors coincide in depth with major changes in the acidity of the ice. Many researchers therefore believe the deep internal layering in RES images to be caused by the increased conductivity due to these acidic layers (e.g. *Hammer et al., 1980*; *Millar, 1981*; *Hempel et al., 2000*).

Changes in acidity are in turn highly correlated with climate changes. During the cold periods, the alkaline impurity content of the ice is amplified due to increased amounts of wind-borne calcium carbonate dust (*Jacobel and Hodge, 1995*). The alkaline impurity content neutralizes most of the acidic aerosols, and causes the ice to be slightly alkaline. Hence, only few RES layers are observed in the glacial ice.

In the Holocene ice, many of the prominent radio-echo layers can be attributed to layers with high levels of volcanic acids. Explosive volcanic eruptions are able to eject vast amounts of sulphuric acids into the atmosphere from where it is transported by the atmospheric circulation and subsequently incorporated in the snowfall (*Hammer, 1980*).

Another possible cause of the internal layering is small, but sharp, changes in crystal orientation fabrics down the ice column. This may cause contrasts in the dielectric permittivity large enough to produce detectable internal reflections. An analysis of the dielectric properties of ice performed by Fujita and Mae (*Fujita and Mae, 1994*) suggests that when using a radio-echo sounder operating at frequencies above 60 MHz (i.e. also for the radar used by the University of Kansas), the predominant cause of the deep internal reflectors is changes in ice fabric. The coincidence of the observed radio-echo layers with the depths of layers corresponding to ages of large volcanic eruptions, can then be explained by acid impurities and/or ash particles changing the mechanical properties of the ice, and hence the ice fabric pattern.

4.1.3. Isochronous layers?

Despite disagreements on the cause of the internal layering in RES imagery, there is general consensus of the layers being past deposition surfaces and thus isochrones, i.e. layers of the same age.

Indeed, the observed layering does obey to the rules for isochrones. As the ice flows within the ice sheet, the old surfaces will deform and maybe fold, but two layers will never cross each other. The deep internal layers of the ice sheets found in RES images can be traced continuously over large areas (in this thesis, the layers have been traced over a distance of more than 500 km), and no intersection of layers occurs. The layering will therefore in the rest of the thesis be assumed to represent isochronous surfaces within the ice sheet.

4.1.4. Basic processing of the RES images

The electromagnetic wave looses energy as it propagates down into the ice, and consequently only weak reflections are recorded from the lower layers. An example of a "raw" radio-echo image is shown in figure 4.2. Notice that the internal layering of the ice only is seen in the upper 1500 m.

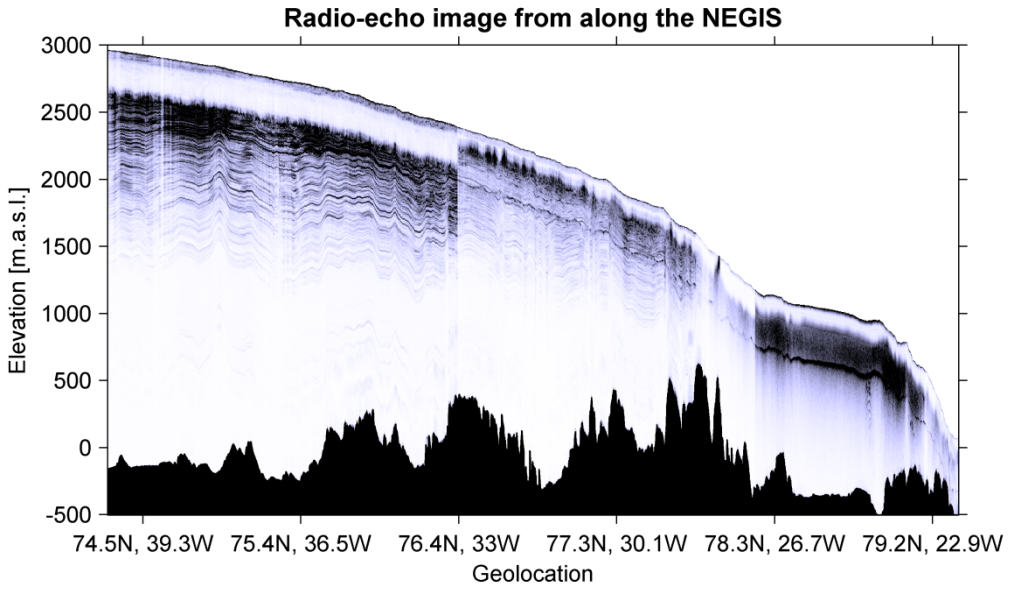

Figure 4.2: Raw radio echogram from along the North East Greenland Ice Stream. The layering is only visible down to a depth of approximately 1500 meters. The signal from the uppermost part of the ice sheet has been removed, as the sensitive receiver could not handle the high energies involved in reflections from layers here. A clear division of the image into three separate segments of flight-line is seen. The processed RES image is found in figure 4.5, p. 26 and in appendix II.

In order to improve the visibility of the deeper layers, a MatLab-routine has been used to gradually enhance the contrast of the RES image. Considering one place at a time, the return signal for every pixel is seen relative to the average value of the return signal in an area above and below the pixel (inspired by the method used by D. Dahl-Jensen, pers. comm.). In appendix I a more thorough description of the employed method is given. It is shown that in order to obtain the best possible layering in the resulting image, the distance over which the average is taken must be chosen approximately equal to the distance between the major layers (11 pixels).

4.1.5. Digitizing the layers

Though it may sound rather easy, it is important to recognize that it can be very difficult to digitize the layers correctly. On a small scale, a strong signal may suddenly disappear, while another layer in the neighbourhood takes over being the dominant one. In this case, it is hard to follow the correct layer, and not unwillingly make a shift to the new layer, which now shows up with the strongest signal.

Additionally, the textures of the layers change, and some layers suddenly seem to split up in two, leaving the person digitizing with the choice of which one to follow now. In these difficult cases, one can rely somewhat on the shape of the surrounding layers to help determine which layer is the right one to follow. The shape of the layers above and below the considered layer should remain approximately the same, or at least change in the same manner down the ice. Also the fine structure of the layering sequence is an important tool for correctly identifying the different layers.

The processed RES-image with its internal layering can be seen in figure 4.5, p. 26, and a larger version of the same figure is found in appendix II. The internal layering is visible along the first 500 km of the flight-line, and many more layers are present in this enhanced image than in the image derived from the raw radio-echo data (figure 4.2).

4.1.6. Uncertainty of the layer depths

The digitizing error is believed to be around one pixel, i.e. ±4.5 m. Furthermore, the conversion of the two-way travel time to depth of the layers on the RES imagery is itself a subject to uncertainty. As mentioned, the firn layer correction at the NGRIP drill site is 12.5 m, and this number is used to correct all layer depths along the profile. The uncertainty associated with this conversion is assumed to be in the order of 5 m. This takes into account that the correct firn correction may depend on the location along the flight-line, as the density-depth profile changes towards the margin.

In most of the remaining thesis, ice equivalent coordinates are used, i.e. the air-filled space in the firn layer is subtracted. At NGRIP, this is approximately 24 meters (*S. J. Johnsen, pers. comm.*). Under Greenlandic conditions, the transition from firn to ice takes place in the upper 60-80 meters of the ice sheet (*Paterson, 2001, table 2.2*), far above our uppermost layer. The firn-ice transition can thus be corrected for by simply subtracting 24 m from the different layer depths. This correction factor is also associated with some uncertainty, which is taken to be 1 m (*S. J. Johnsen, pers. comm.*).

As the three uncertainties are independent and can be assumed Gaussian, an estimate of the combined uncertainty is the three error estimates added in quadrature (*Taylor, 1997, p. 58*). Hence, the uncertainty of the layer depths is estimated to be about 7 m.

4.1.7. Dating the selected layers

As the internal layers in an ice sheet can be traced for over hundreds of kilometres, they can also be traced to ice core drill sites. From ice core data, a depth-age relationship for the drill site is known, which then, via the internal layering, can be extended to give an approximate depth-age relationship for the whole ice sheet. For the present purpose, ice core data is used from NorthGRIP, which is situated not far from the beginning of the flight-line. The timescale used is the GICC05 timescale (Greenland Ice Core Chronology 2005), which is based on multi-parameter counting of the annual layers down several ice cores, including the NorthGRIP ice core (*Andersen et al., 2006*).

The ages of the layers are found with some uncertainty. There is an uncertainty due to the digitalization of the layering around NGRIP (this error is set to be around 1 pixel, i.e. 4.5 m) and the depth estimates (1 m and 5 m), but there are also inherent uncertainties of the timescale (*Andersen et al., 2006*). The age estimates of the selected radio-echo layers and their resulting uncertainties are stated in table 1, along with an event, which may have caused their formation.

In figure 4.3 is shown a comparison between the depth of the traced radio-echo layers and the NGRIP δ^{18}O-profile. From this figure, as well as from table 1, it is clear that rapid climate events are indeed a major cause for the formation of radio-echo layers in the Greenland Ice Sheet. All the major climatic oscillations during the Holocene are among the most prominent radio-echo layers, and in the glacial ice, strong reflections are seen from the interstadial events puncturing the last glacial period. However, not all the layers can be explained by changes in climate. The two deepest layers do not seem to have a climatic counterpart.

GICC05 age (years b2k)	Age of concurrent climatic or volcanic event (years b2k)
4031 ± 44	Unknown volcano, Dated[1]: 4045 ± 8
4917 ± 52	Unknown volcano, Dated[2]: 4932 ± 6
7215 ± 60	Unknown volcano, Dated[2]: 7247 ± 14
8276 ± 73	8.2 ka ECM peak*, Dated[2]: 8236 ± 24
11260 ± 123	11.1 ka $\delta^{18}O$ anomaly, Dated[3]: 11270-11280
14612 ± 184	Onset of Greenland Interstadial 1 (GI-1) Dated[4]: 14680 ± 93
28651 ± 531	Onset of Greenland Interstadial 4 (GI-4), Dated[4]: 28900 ± 449
38053 ± 759	Onset of Greenland Interstadial 8 (GI-8), Dated[4]: 38220 ± 724
45310 ± 986	Unknown
52895 ± 1162	Unknown

Table 1: Ages of the traced layers as found from the depth-age relationship for NGRIP when using the GICC05 timescale. The approximate uncertainties (1σ) are given. Also mentioned are possible causes of the RES layers, found by comparing to volcanic and climatic records. The numbering of stadial events is according to *Walker et al., 1999*. GI-1 is also known as the Bølling-Allerød Interstadial. Ages are given relative to year 2000 AD (b2k). References: 1: *Clausen et al., 1997*. 2: *Vinther et al., 2006*. 3: *Rasmussen et al., 2007*. 4: *Andersen et al., 2006*. *This RES layer can also be attributed the 8.2 ka cold event (GH-8.2 event), which happens almost simultaneously (from 8300 b2k to 8140 (*Rasmussen et al., 2007*)).

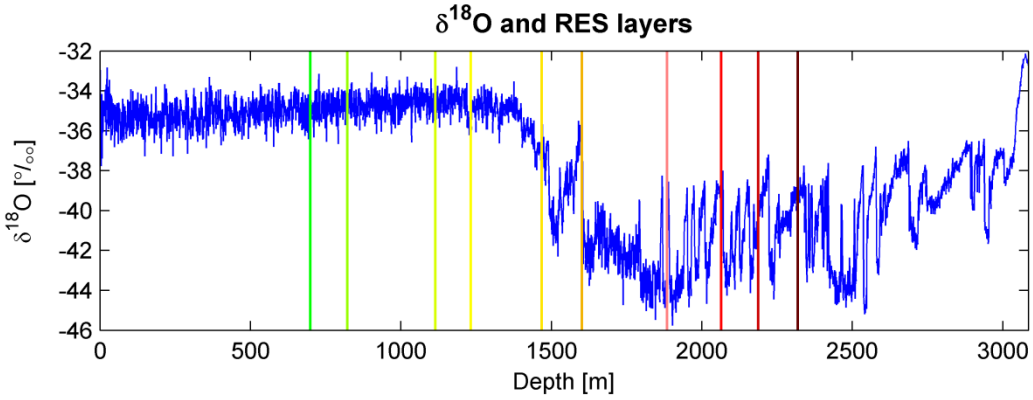

Figure 4.3: A comparison between the NGRIP $\delta^{18}O$-profile, which essentially is a climate index, and the depth of the traced radio-echo layers. Many of these coincide with climatic events.

4.2. Ice thickness and basal topography

Ice thickness and basal topography are two very important glaciological parameters for understanding the flow dynamics of an ice sheet. Where a radio-echo pulse is recorded from the glacier bed, they can both be inferred. The basal topography is deduced from knowledge of the ice thickness and the surface elevation, and a map of the bedrock topography can be constructed. Such a map for the area around the North East Greenland Ice Stream is shown in figure 4.4, along with the investigated flight-line.

All the small-scale variations in bed topography resolved by the radio-echo sounding measurements are not important for the ice flow. In the data analysis, the bed topography and ice thickness profile have therefore been smoothed over a distance of approximately three ice thicknesses. This number was chosen such that as many as possible of the undulations in the internal layering had a bedrock counterpart.

4.2.1. Basal topography in the area around the NEGIS

One of the most significant features of the map showing the basal topography around the NEGIS (figure 4.4), is an extensive area of very low elevations (blue) in the inner part of the ice sheet. The elevations reach more than 200 meters below sea level. The area is rather elongated, and is to a large extent following the location of the ice ridge, which stretches from the south east to the north west. This depression of the bedrock is due to the isostatic adjustment of the lithosphere in response to the overburden pressure of the ice volume. The bed is also below sea level at several locations along the margin, where the isostatic compensation is substantially less. This is e.g. the case along some segments of the trench along the NEGIS (whose existence and continuity is not very obvious from the map).

The drainage basin around the NEGIS is flat and low compared to most of the surrounding areas. Especially the area south east of the flight-line is mountainous with elevations up to 2500 m.a.s.l. Another highland area is situated to the north of the ice stream drainage basin.

In general, the bed topography of the central areas is relatively smooth, and the roughness of the bed increases towards the margin. This is seen from figure 4.5, which shows the detailed bedrock topography profile along the flight-line. The bed is quite smooth along the first 150 km of the flight-line, but from 150 to 500 km the bedrock topography becomes rougher, and hence increasingly important for the ice flow. Some of the large bedrock undulations may be the result of the flight-line repeatedly crossing into and out of subglacial trench beneath the ice stream.

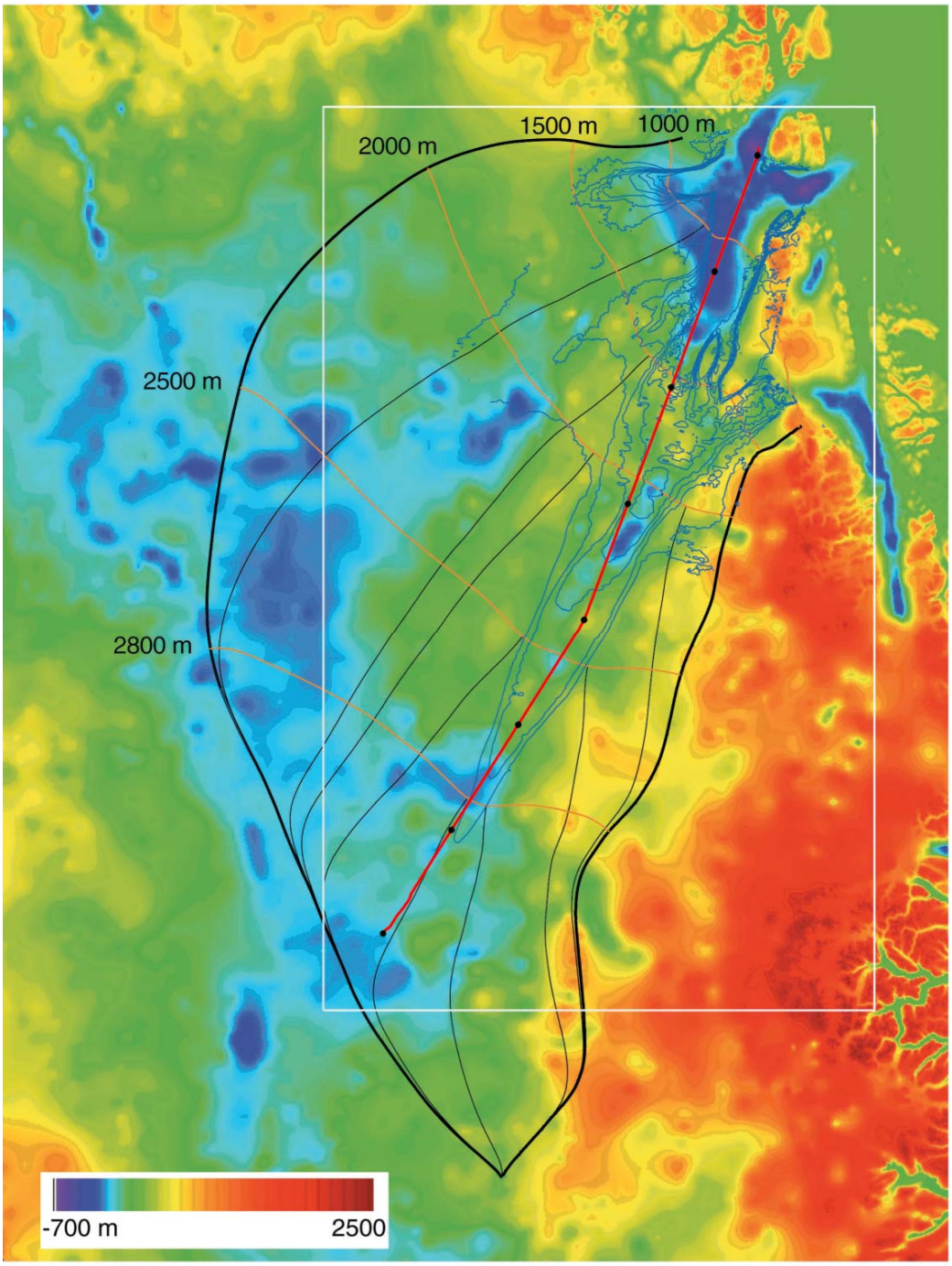

Figure 4.4: A map of the basal topography of the drainage basin around the NEGIS. The delineation of the drainage basin is indicated with the thick black line. The examined flight-line along the ice stream is shown in red. Black dots are plotted with a spacing of 100 km. Also shown are flowlines originating at the edges of the drainage basin (thin black lines), elevation contours in the basin (orange lines) and ice stream speed contours going from 25 to 200 m/yr (blue lines). See section 4.3.3 for more. In the following, we will concentrate on the area in the white box, which contains the same area as plotted in figure 4.7, p. 30. Figure from *Joughin et al., 2001*.

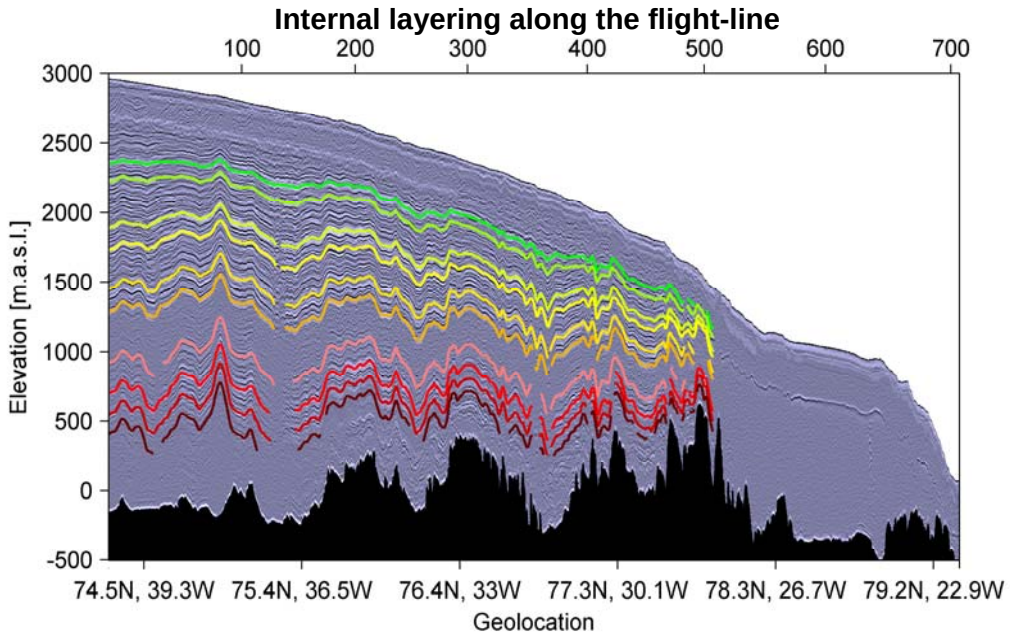

Figure 4.5: Enhanced radio echogram from the flight-line along the NEGIS. Compare with figure 4.2, p. 20 to see the effect of the enhancement. More layers than before are present, including several deeper layers. Furthermore, there is no longer any visual difference in appearance between radar images acquired at different times. The x-axis is given in geographical coordinates as well as distance from the beginning of the flight-line (in km, shown in top of the image).

The impact of the bedrock topography on the ice flow is so large that it influences the shape of the ice sheet surface. This is e.g. the case for the area between 400 and 500 km from the beginning of the flight-line, where the surface elevation undulates with amplitudes close to 100 m. Such large surface undulations are extreme topography for the surface of an ice sheet.

At a distance of approximately 500 km from the beginning of the flight-line, the ice passes a major obstacle at the bed. Hereafter, the bedrock suddenly becomes flat once again, but at much lower elevations (300 m.b.s.l.) than those characteristic for the rest of the profile. In figure 4.4, this is where the flight-line reaches the deep depression of the bed that is situated close to the margin of the ice sheet. The drop in bed elevations coincides with a sudden drop in surface elevations, as well as with a complete disappearance of the layering in the ice. Hereafter, we reach the ice plain, which probably is formed due to a deforming layer of sediments (section 3.2.2), and the surface stays close to level for approximately 100 km. This is a significant departure from the typical parabolic ice sheet profile. At a distance of 650 km, the margin of the ice sheet approaches, and the surface elevations rapidly decrease to zero.

4.3. Present surface velocities

Over the last decades, satellite remote sensing techniques have been developed that have great potential for improving our knowledge on ice flow dynamics. For instance, a wealth of new data has become available from synthetic aperture radar (SAR) imagery. Using the methods of interferometry in combination with SAR data, it has become possible to infer the present-day surface velocities over large areas of an ice sheet. This remote sensing technique is called InSAR (for Interferometric Synthetic Aperture Radar).

4.3.1. Basic principles of SAR interferometry

SAR images are acquired by satellites carrying a microwave emitting radar antenna. At the surface of the Earth, the radar pulses are scattered in all directions, with some reflected back towards the antenna, where the amplitude and phase of the returning radar beam is recorded (see figure 4.6 A).

For most purposes, the measured amplitude of the return signal is used. But for InSAR, it is the recorded phase which is important. The phase of the reflected radiation from a specific place depends on the dielectric properties of the surface, as well as on the distance from the antenna to the point in mind. The returned phase for a small area on the ground can be thought of as being the joint signal from several ground reflectors, which all have different dielectric properties and slightly different distances to the antenna. The combination of different ground reflectors from area to area gives rise to rather abrupt changes in phase, and hence the raw phase return in any SAR image shows no correlation from pixel to pixel (*Pritchard, 2006*).

InSAR relies on repeated radar imaging of a given geographic location. Given the consistency of the phase measurements, two measurements taken at the same place but some time apart will give the same result, provided nothing on the ground has changed in the meantime. If, however, the ground has moved during the time between the two passes of the satellite, the recorded phase from a specific area will have changed due to the increase or decrease in distance from the ground reflectors to the satellite (see figure 4.6 B).

Only the component of ground motion in direction of the line of sight from the radar antenna to the ground will cause a phase difference to be observed. (By line of sight is meant the inclined ray followed by a radar pulse from the satellite to a scattering point on the ground). By comparing the measured phase of the return signal in two subsequent passes of the satellite over the same spot, it is thus possible to infer one component of the surface velocity vector.

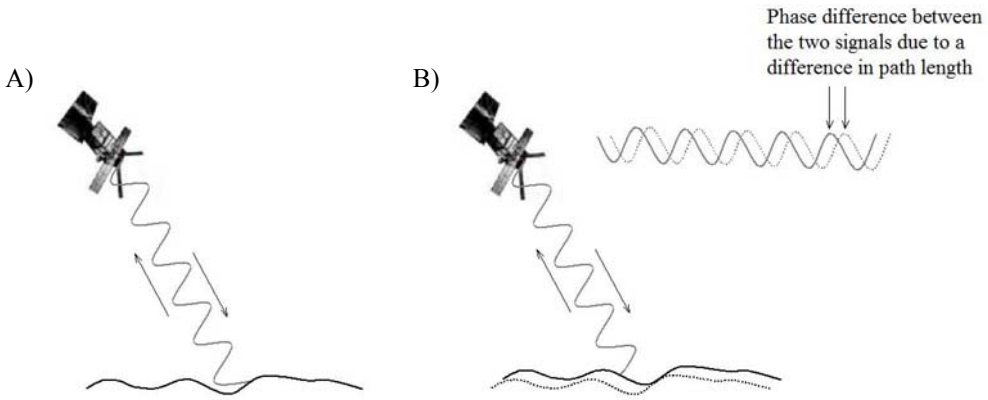

Figure 4.6: A) Satellite carrying a microwave emitting radar antenna. The satellite is moving into the paper, and is emitting microwaves in the plane of the paper. The phase of the returning wave is measured. **B)** When the satellite returns to the same spot at a later time, the ground may have moved compared to the first passing. The old surface is shown with dots. The amount of movement in direction of the beam (line-of-sight direction) can be inferred from the phase difference between the two signals from the same spot. In this case, the ground has both moved upwards and to the right. As the radar only is sensitive to movement in the line-of-sight direction, it is here mainly the upwards component, which is measured.

In reality, a satellite never exactly returns to the same spot. Thus, for InSAR to map surface displacement, it is necessary to account for the phase differences due to the slightly different viewing conditions. With knowledge of the orbital motion of the satellite and the topography in the area, the phase differences due to this effect can be modelled and removed. Other sources of error include degradation of the radar signal during its way in the atmosphere. See Joughin et al. for further discussion of the uncertainties in SAR interferometry (*Joughin et al., 1998*).

4.3.2. Using InSAR to derive ice sheet surface velocities

Two SAR images provide a single component of the velocity vector, which is a mixture between horizontal and vertical velocity components. Ideally, all three components of the velocity vector can be found from three pairs of SAR images from different satellite directions. However, only data from two satellite directions are available for the Greenland Ice Sheet. In order to find the third component of the velocity field, it is customary to use the approximation of surface-parallel flow, i.e. that the ice is flowing parallel to the ice surface and in a direction normal to the topographic contours. This gives the third velocity component expressed by the flow in the two other directions and the slope of the surface. Detailed description of the method can be found in *Joughin et al., 1998*.

For the assumption of surface-parallel flow, an accurate estimate of the surface slope in the area is required, which in turn requires detailed knowledge of the small-scale topography. This is often not known beforehand. Fortunately, such information can also be obtained using interferometry. If two SAR images are acquired within a short time interval, such that the influence of any surface motion can be neglected, the topography of the area can be derived. The detailed topographic map of the area around the North East Greenland Ice Stream shown in figure 2.1 B, p. 4 was partly made by use of this technique.

In reality, the flow in an ice sheet is not surface-parallel. In the accumulation area, there is a velocity component downwards into the ice, and in the ablation area the ice motion is slightly inclined upwards to the surface. But in most places, surface parallel flow is the most important part of velocity vector.

4.3.3. Surface velocities around the NEGIS

Figure 4.7 shows a map of the surface velocities in the area around the North East Greenland Ice Stream, derived by Joughin et al. (*Joughin et al., 2001*) using InSAR and the assumption of surface-parallel flow. Given the low accumulation rate, the flat surface topography and the fast-moving ice in the area, the assumption of surface-parallel flow should not impose too large errors on the resulting velocities. From a comparison of the derived surface velocities with 12 GPS-measurements, Joughin states that an approximate error of the velocities is 5 m/yr (*Joughin et al, 2001*).

It is clear from the map that the area has large spatial variations in the velocity field. It is also seen that the ice stream consists of several branches, which both supply material to the ice stream and conduct material away from it. In its upper reaches, a tributary, often termed the southern tributary, merges with the ice stream. It is a broad feature, which barely is visible on the map as a lighter blue area to the south of the ice stream. At approximately 400 km, the flow divides into two branches, the northernmost branch feeding Nioghalvfjerdsfjorden and Zachariæ outlet glaciers and the eastern branch feeding Storstrømmen outlet glacier. A second tributary merges with the ice stream at a distance of approximately 600 km from the beginning of the flight-line. In the very last part of the flight-line, the flow again divides into two branches, and another flow unit merges with the ice stream.

Another apparent feature of the surface velocities along the ice stream is the occurrence of a slow-moving area in the middle of the ice stream at approximately 500-550 km from the beginning of the flight-line. By comparison to the local bed topography, it can be seen that the lower velocities in this area are developed as the reaction to a bedrock obstruction which is large enough to force the ice flow around the obstacle rather than over it (*Joughin et al., 2001*).

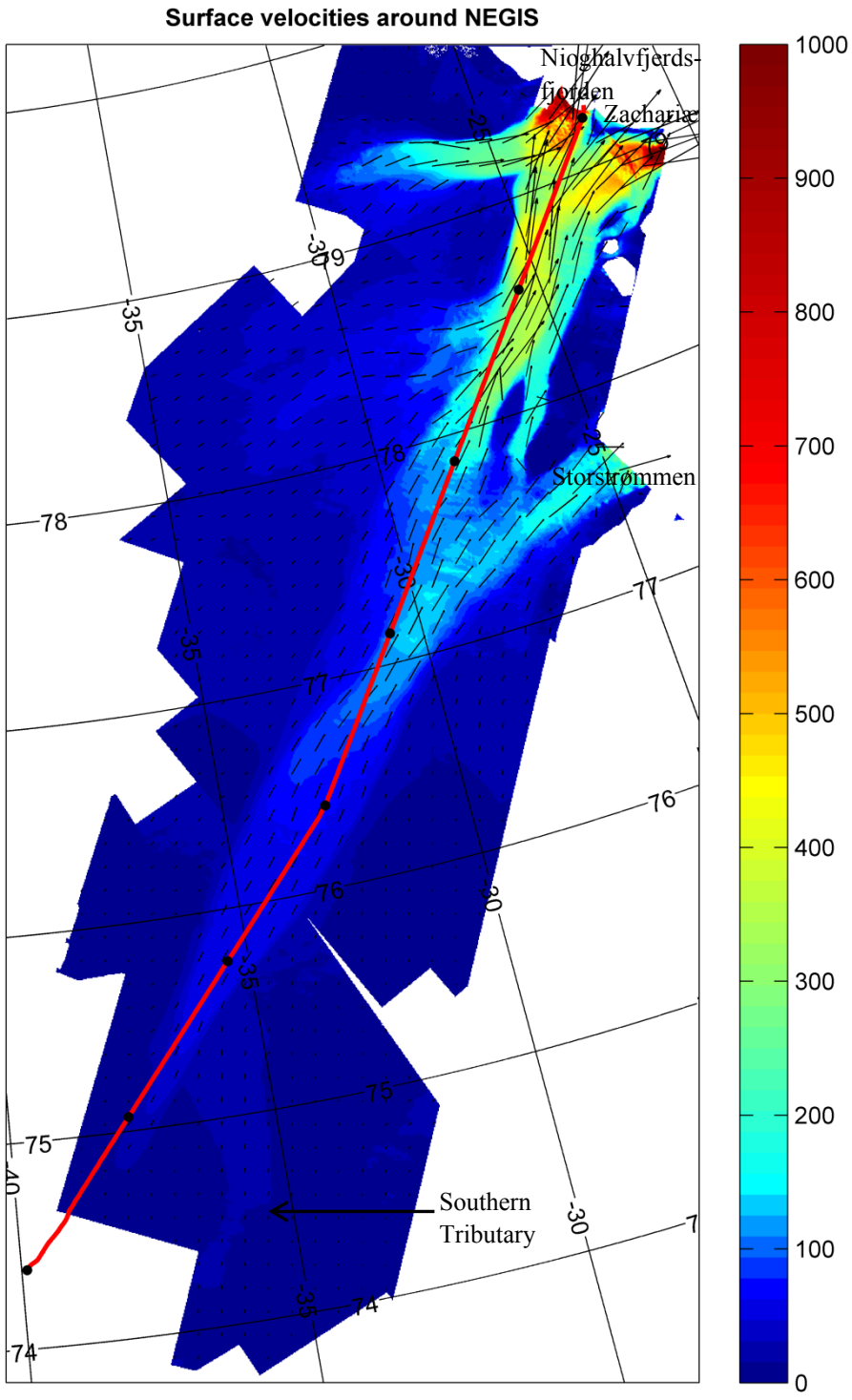

Figure 4.7: Map of the surface velocities in the area around the North East Greenland Ice Stream. The colouring is based on the total surface speed (in m/yr), and the arrows mark the direction and size of the surface velocity. The considered flight-line is shown with red. Black dots are plotted on the flight-line with a mutual spacing of 100 km. Surface velocity data provided by Ian Joughin.

4.3.4. Surface velocity along the flight-line

The changing surface velocity along the flight-line is shown in figure 4.8. No data exist for the first part of the flight-line, but the velocities in this area are presumably low, as the flight-line starts only about 40 km away from the ice divide. Where the measurements start, in a distance of 38 km from the beginning of the flight-line, the surface velocities are around 4 m/yr.

Following the flight-line, the ice flow velocities increase dramatically towards the ice sheet margin, reaching more than 600 m/yr. From the map in figure 4.7, it can be seen that even larger surface velocities (more than 1000 m/yr) are found at other places close to the margin. Two areas with very large velocities stand out, one of which is close to the very last part of the considered flight-line. The fact that the surface velocities reach more than 1000 m/yr in this area, situated just 5 km away from our flight-line where we "only" reach velocities of 600 m/yr, gives an impression of the enormous velocity gradients in the area. Velocity gradients of a similar size also characterize the other area with high surface velocities.

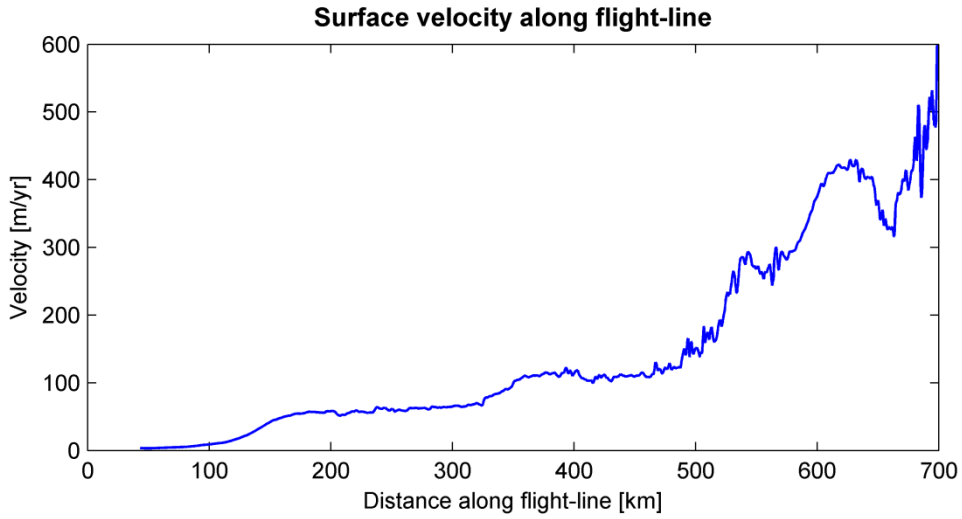

Figure 4.8: Variation of the total surface velocity along the flight-line.

It is clear from figure 4.8 that the surface velocity does not increase uniformly along the flight-line. Along the first 500 km of the flight-line, the increases in velocity mainly occur at specific locations, in between which the velocity is relatively stable. As the internal layering of the ice only is visible along the first 500 km of the flight-line, the most interesting jumps in the surface velocity profile occur around 100-150 km, 350 km and yet again around 500 km from the beginning of the flight-line.

Until about 80 km from the beginning of the flight-line, the surface velocity is only slowly increasing. But in the area from 80 to 160 km, the velocity suddenly increases more than fivefold, from below 10 m/yr to more than 50 m/y, corresponding to a velocity increase of 0.5 m/y per km. Hereafter, it remains relatively stable for a while, until a second enhancement of the flow velocities occurs at 320 to 360 km from the beginning of the flight-line. Here, the velocities speed up roughly by the same amount as at the first jump (from about 65 m/yr to 110 m/yr) over a distance of merely 40 km.

Over the last 200 km of the flight-line, the velocity profile gets more and more rough and complicated. Even larger increases (at least in an absolute sense) occur, but in some areas, the velocity is decreasing as well. This may be due to the flight-line crossing in and out of the channel in which the ice stream flows, and the ice stream flow becoming more and more complicated. The general trend, however, is an extreme increase in surface velocity towards the margin.

Chapter 5

A preliminary data analysis

5.1. A non-perfect flowline in an area with large spatial variations

In the following is used a right-handed curvilinear orthogonal coordinate system, with the x-axis in the direction of the flight-line, and the z-axis pointing upwards. z is measured in meters above sea level (m.a.s.l). The velocity vector according to this coordinate system is denoted $\boldsymbol{v} = (u, v, w)$, subscript s denotes the surface velocities.

In the subsequent analysis, the flight-line along the North East Greenland Ice Stream will often be considered an exact flowline. However, the large spatial variations in surface velocity in the area around the NEGIS may inflict a large uncertainty on our results when assuming the flight-line to be a true flowline. A measure of the deviation from a true flowline is expressed by the angle between the actual velocity vector of the location and the flight-line (figure 5.1 B).

From figure 5.1 A it is seen that all along the flight-line, the total surface velocity is very similar in magnitude to the surface velocity in direction of the flight-line, u_s. Their difference is plotted in black. But in some areas, a non-negligible velocity component perpendicular to the flight-line (cyan) exists, which in general increases towards the margin of the ice sheet. This is, however, mainly a consequence of the larger surface velocities. The actual angle between the flight-line and the surface velocity vector at a specific location fluctuates around zero with about the same magnitude all along the flight-line, reaching from almost -30º to +12º (figure 5.1 B). This is quite a lot, and it implies that caution must be taken when using the approximation of the flight-line being a true flowline.

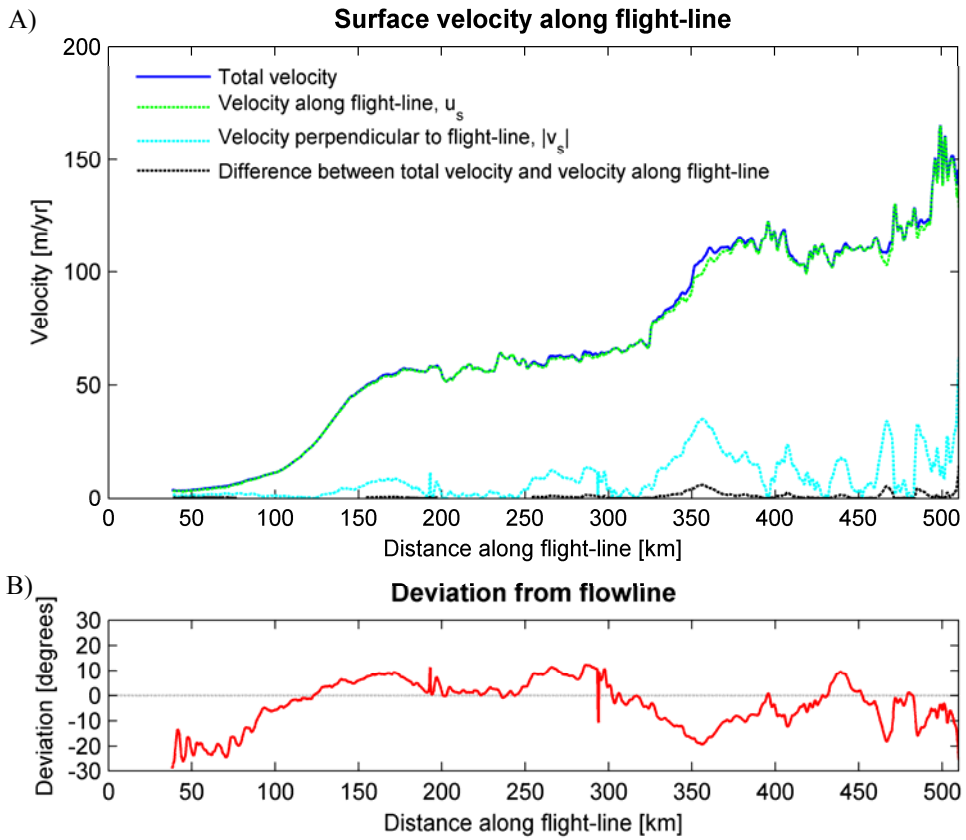

Figure 5.1: A) Surface velocities along the flight-line. The total velocity is portrayed, as well as the velocity components along the flight-line and perpendicular to the flight-line. Although the total velocity and the velocity component along the flight-line are almost equal along most of the flight-line, some deviations do occur, especially over the last 200 km. This difference is represented with a black line. **B)** The angle between the observed velocity vector and the considered flight-line.

As the flight-line is not a perfect flowline, the material forming the internal layers does not necessarily originate further up the flight-line, but some distance away. As we have no information on the internal layering away from our flight-line, we cannot say anything about the conditions under which the ice flow has taken place in these areas. So the most important issue in this aspect is whether the particles have originated sufficiently close to the flight-line for them to have experienced approximately the same conditions as they would, had they originated exactly at the flight-line. Only then it is possible to extract reliable information from the internal layering along the flight-line by use of a flow model.

In order to ensure that this is the case, particles starting on the flight-line have been tracked upstream and downstream to see whether or not they stayed within a reasonable area around the ice stream. The resulting flowlines of the particles are

shown in figure 5.2. It is also illustrated how long it took for the particles to reach the margin of the ice sheet when starting at a specific location on the flight-line. It has been assumed that no change occurs in the surface velocity field with time (neither in magnitude nor direction), and it is not taken into account that the velocity changes as the particles move down into the ice.

Along the first part of the flight-line (until around 500 km), the flowlines are relatively close to the flight-line, while major discrepancies arise in the last part. The sticky spot, i.e. the area with much smaller surface velocities mentioned in section 4.3.3, brings about a division of the flowlines, depending on which way the particles choose to go around it. And just after, the particles seem to originate far west of the flight-line. Furthermore, close to the margin there is no doubt that most of the particles actually choose to flow into Zachariæ Isstrøm to the east instead of Nioghalvfjerdsfjorden to the north, over which the radar carrying aircraft passed. However, when only dealing with the ice flow along the upper 500 km of the flight-line, the minor discrepancies here justify our assumption of the flight-line being close to a flowline.

As expected due to the large increase in surface velocity towards the margin, the time it takes for the particles to reach the margin is almost exponentially decreasing with starting distance from the ice ridge. For a particle starting 50 km away from the commencement of the flight-line (where the surface velocity data starts), it takes little less than 13 ka to reach the margin. However, from a climatic perspective the ice flow in the North East Greenland Ice Stream may react faster to changes in the mass balance than this (*Summerfield, 1991, p. 267*).

Had it been anywhere else, the fairly small discrepancies from a true flowline along the first 500 km of the flight-line would not have been an issue for the data analysis. But even small discrepancies can be of large importance if the conditions for flow are changing rapidly across the flight-line. And in case of an ice stream, this is very likely to be the case. Nevertheless, we will still assume this discrepancy to be insignificant for the forthcoming data analysis.

The fact that we are not dealing with a perfect flowline also presents us with another problem. The transverse velocity component ought to be taken into account when dealing with the equations of flow along the flight-line (see section 5.3.3). Due to its rather large value at some places (though still small compared to the along track surface velocity component), it may be important for the analysis (figure 5.1 A). Nevertheless, the contribution from the transverse velocity component is disregarded in the subsequent analysis, since new parameters concerning e.g. the rate of change of ice thickness across the flight-line then would appear in the equations.

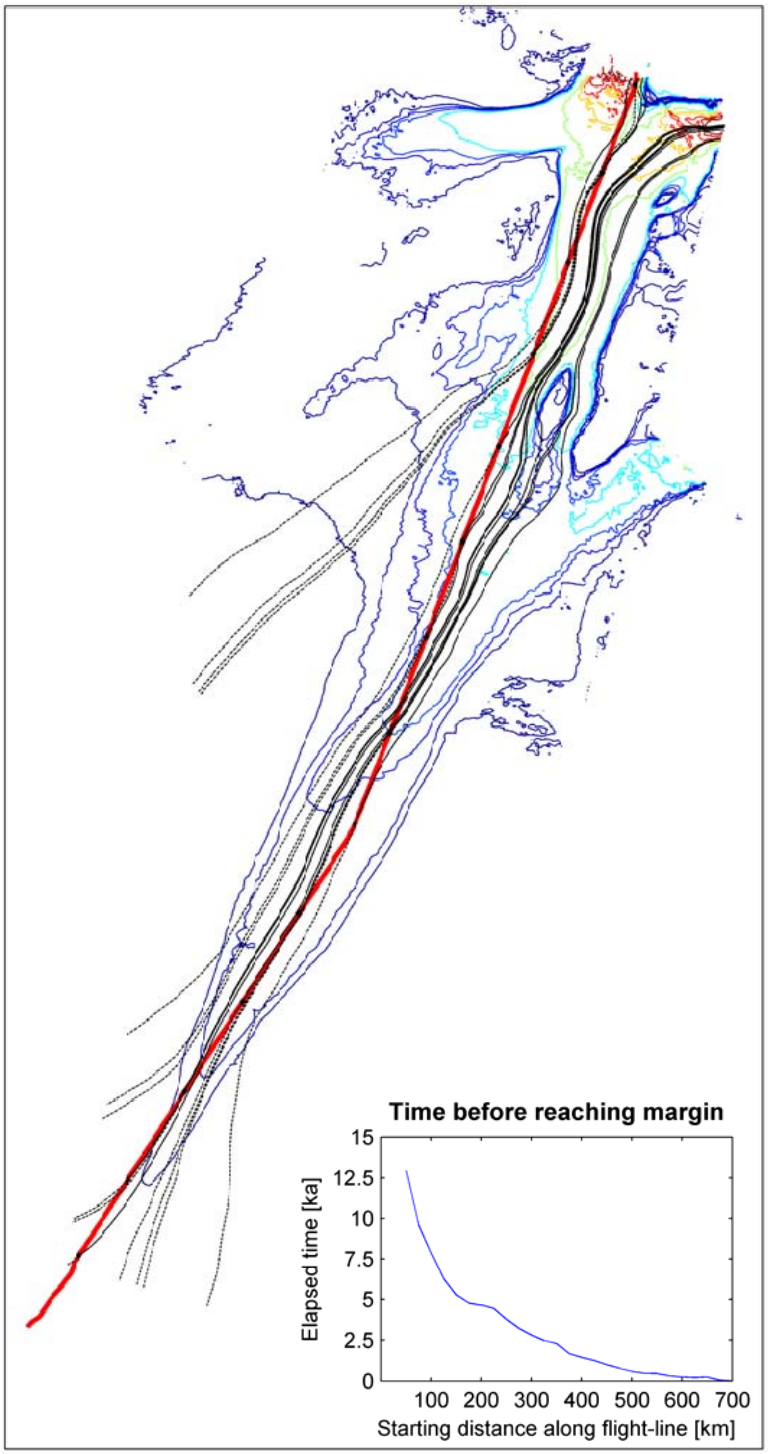

Figure 5.2: The flowlines (in black) performed by particles starting and ending at the flight-line (red) 50 km apart. The flowlines are superimposed a contour map of the total surface velocity, which indicates the location of the ice stream. The inserted figure in the lower right shows the resulting time it takes a particle to reach the margin from a given position along the flight-line when assuming constant velocities with time (but not in space).

5.2. Present accumulation rates

We will now determine the present accumulation rates along the flight-line by use of a very simple one-dimensional model. Not only do the accumulation rates have major implications for the mass balance of the ice stream, and hence the ice flow, they are also a prerequisite for a later analysis (section 5.3).

5.2.1. A simple model for determining the present accumulation and thinning rates along the flight-line

When assuming a constant horizontal velocity with depth, the vertical velocity component in the upper part of an ice sheet, $w_{upperpart}$, can be approximated as decreasing linearly in magnitude with depth, whilst having a magnitude at the surface of the ice sheet equal to the ice equivalent accumulation rate. A derivation of this relationship is found in appendix III. The following relationship therefore holds:

$$w_{upperpart}(x,z,t) = -a(x,t) - \dot{\varepsilon}_z(x,t) \cdot (S(x,t) - z)$$

Here, a denotes the accumulation rate, S is the surface of the ice sheet, and $\dot{\varepsilon}_z$ is the near surface vertical strain rate component. We will in the following refer to $-\dot{\varepsilon}_z$ as the thinning rate, as it conveys information on the thinning of the annual layers due to ice flow.

During the Holocene, the accumulation rate, the thinning rate and the elevation of the ice sheet surface can be assumed constant in time. Furthermore, their changes with distance will be disregarded in the subsequent analysis, i.e. it is not taken into account that the ice have originated further upstream where other conditions may prevail. It is therefore essentially a one-dimensional analysis.

With these assumptions, w only depends on z, and the above equation can be integrated to give a very simple formula for the age-depth relationship down the upper part of the ice sheet:

$$t(z) = \int_S^z \frac{1}{w(z)} dz = \int_S^z \frac{1}{-a_0 - \dot{\varepsilon}_z \cdot (S - z)} dz = \frac{1}{\dot{\varepsilon}_z} ln\left(\frac{a_0 + \dot{\varepsilon}_z(S - z)}{a_0}\right)$$

Here, t denotes the age of the ice. This timescale only depends on two parameters; the present accumulation rate (a_0) and the thinning rate ($-\dot{\varepsilon}_z$). At any place along the radio echogram, this relationship can be fitted to the depth of the age markers in the Holocene ice, and the best fitting values of a_0 and $\dot{\varepsilon}_z$ can be determined. The results are shown in figure 5.3.

Two cases have been considered. In one case (denoted the "sandwich model"), the downwards velocity is assumed to decrease linearly all the way down to the bed, where it equals zero. In this model, the vertical strain rate is given by $\dot{\varepsilon}_z = -a_0/H$, and hence only one parameter is to be determined. The sandwich model implies a constant horizontal velocity with depth all the way down the ice sheet, and thus full basal sliding. No such restrictions have been applied to the so-called "kink model". This is a generalized form of the Dansgaard-Johnsen model, which we will deal with further in chapter 6. Additionally, the two models are fitted to data from a various number of internal layers.

5.2.2. The accumulation rates

For both the sandwich model and the kink model, the calculated accumulation rates along the flight-line do not depend much on the number of layers used in the model (figure 5.3 B). But the two models predict different accumulation rates along the first half of the radio echogram. Generally, the sandwich model overshoots the kink model. For the last part of the radio echogram, the accumulation rates calculated in the two ways coincide. This is an indication that the flow along the second half of the flight-line to a large extent can be described by a sandwich model. Thus, there may be a high degree of basal sliding in this area.

The quality of the fit is generally very good, though deteriorating towards the margin. The deterioration of the fit, as well as the increased disparity between the different models towards the margin, are indications that two and three-dimensional effects become more and more important for the ice flow pattern when approaching the margin.

We believe the best result is to be found when using the kink model and all four layers, as this eliminates the most of the noise, while not putting too many restrictions on the velocity profile. However, it also implies that we are averaging over a longer period of time, in which the accumulation rate (and surface elevation) may have changed, as well as over a larger distance. But due to the minor variation between the results when using a different number of layers, the effect of a varying accumulation rate etc. through time and with distance on the calculated values of the parameters may be quite small.

Yet, it is clear that the present accumulation rates as estimated by these simple one-dimensional models have one serious flaw – they are fluctuating far more than anticipated. A glance at the variation of the ice thickness along the flight-line shows that the ice thickness and the calculated accumulation rates vary together (figure 5.4).

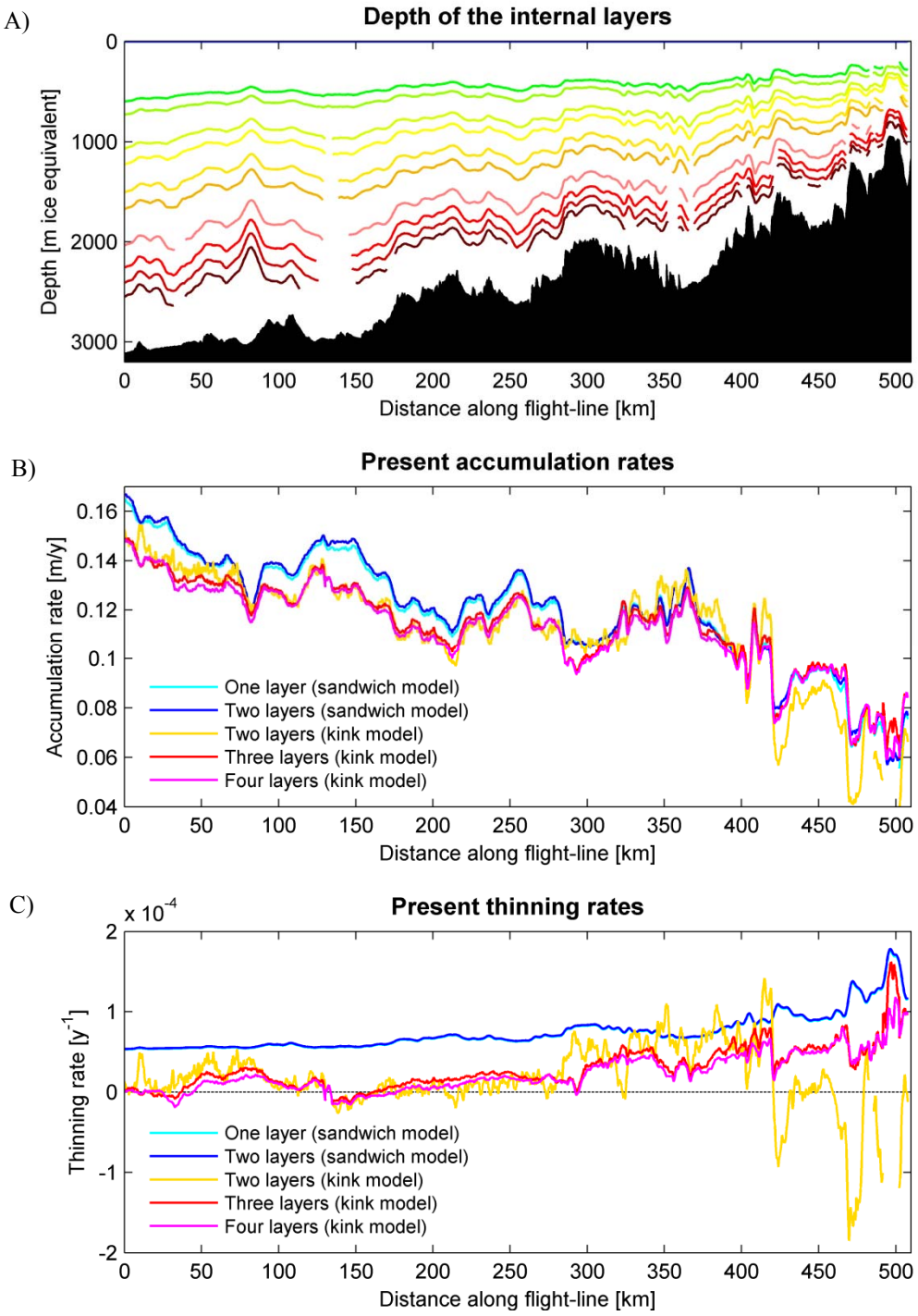

Figure 5.3: A) Depth of the internal layers in ice equivalents. **B)** The accumulation rates and **C)** the thinning rates along the flight-line as found by use of a one-dimensional model. Two variations of the one-dimensional model have been applied: A sandwich model, in which the vertical velocity decreases linearly to zero at the bed, and a so-called kink model, in which such a linear decrease only has been assumed for the upper part of the ice sheet. The cyan line is hiding almost directly behind the blue line.

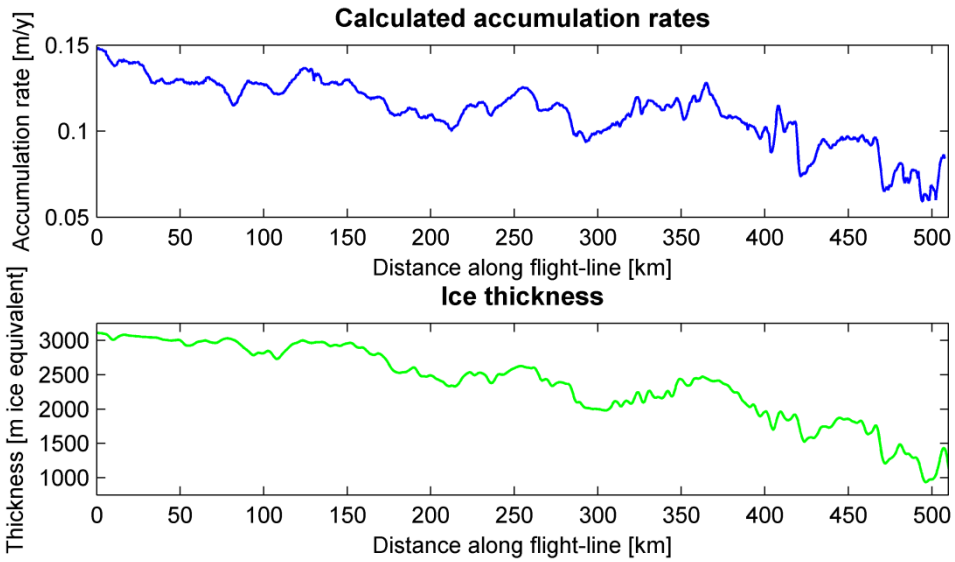

Figure 5.4: A close correlation exists between the ice thickness and the calculated one-dimensional accumulation rates. The accumulation rates shown are those found when applying a kink model and using the depth of the four uppermost layers to determine the best fitting parameters.

It is a possibility that the variations in accumulation rates are genuine. The bedrock relief in the area is large enough to cause the surface of the ice sheet to undulate (see section 4.2.1). It has previously been established that such surface undulations affect the pattern of snow deposition, and are able to create an irregular accumulation rate distribution (*Reeh et al., 1985*). In this way, a connection exists between accumulation rates and bedrock topography, and hence also the ice thickness. However, it seems unlikely that the accumulation rates should follow the bedrock undulations in so high details and over so large distances. Moreover, the accumulation rate pattern matches the bed topography much more closely than the surface topography. It all points to the conclusion that while such a relationship between bed topography and accumulation rates probably exists, it may not be the most influential factor for the derived accumulation rates.

The main reason for the fluctuating accumulation rates is probably that it is not a very good approximation to assume the flow along the ice stream to be one-dimensional. Two-dimensional and three-dimensional effects caused by e.g. the changing ice thickness along the flight-line have been disregarded, which may inflict large uncertainties on the derived accumulation rates. This matter will be taken up more elaborately in section 7.1.4.

Nevertheless, even from this very simple model, some information about the accumulation rates in the area is revealed. In general, the trend is a marked decrease

of the rather low accumulation rates from the inner parts of the ice sheet (0.15 m/yr) towards the ice margin (below 0.10 m/yr). This pattern is consistent with accumulation data from other sources. According to the accumulation map over Greenland shown in figure 5.5, the accumulation rates in the area along the North East Greenland Ice Stream range from 0.15 m/yr to below 0.10 m/yr, with the largest accumulation rates in the inner part of the ice sheet. It should be stressed, however, that only sparse data exist for the accumulation rates in this remote area. The consistency of the one-dimensional accumulation rates with these data makes the overall trend of the acquired data from the one-dimensional model very plausible, despite their correlation with the ice thickness.

These low accumulation rates and the decreasing trend in accumulation towards the eastern margin is explained by a change in weather pattern due to the position of the ice ridge. The northern part of Greenland is predominantly affected by weather systems passing from the north west. The ice ridge acts as a barrier for these storm tracks, hence causing much less precipitation on the lee side of the ridge where the NEGIS is situated. In this way, the ice ridge causes a clear disparity in climate on each side of the ice ridge (*Dethloff et al., 2002*).

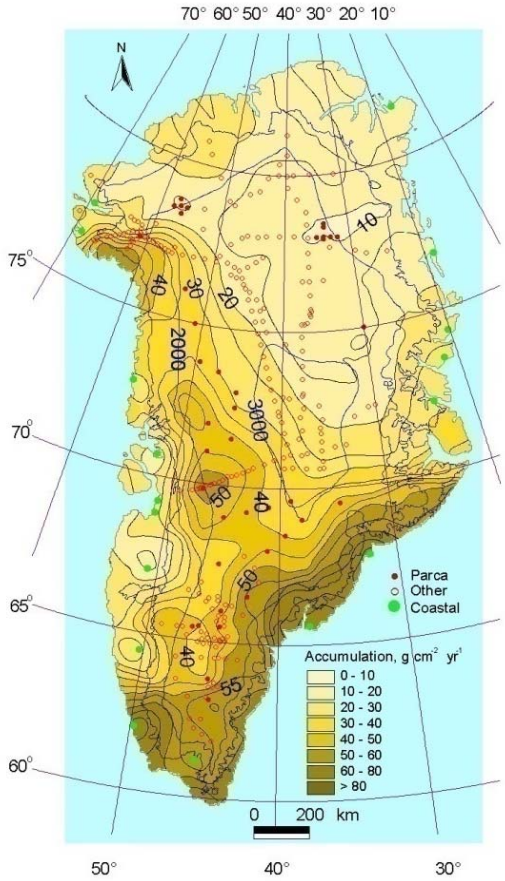

Figure 5.5: Accumulation map based on data from snow pits, shallow cores, deep cores, coastal precipitation data etc. The locations where the accumulation data have been retrieved are marked as red and green dots. The rest of the map is made by interpolation, which imposes a large uncertainty on the result in these areas (up to 20-25%). The accumulation is here defined as precipitation minus evaporation, i.e. surface melting and run off is not included. In this way, it differs slightly from the definition of accumulation rate used in the rest of the thesis, which includes all ways by which material has been added and removed from the surface, and as such probably should have been termed the "surface mass balance" instead. Map from *Bales et al., 2001*.

5.2.3. The thinning rates

When calculating the best fit of the present accumulation rates, the thinning rates along the flight-line were determined as well (figure 5.3 C). While the annual layer thickness in the sandwich model decreases linearly to zero at the bed, the kink model requires less thinning of the uppermost layers. The thinning rates calculated by the sandwich model are therefore generally larger than those found by use of the kink model.

The thinning rates do not show much variation along the flight-line, but do exhibit a slight increase towards the margin. The stability of the thinning rates despite the hilly terrain was against expectations. When the ice thickness is diminished due to an obstacle at the bedrock, the ice is squeezed together, and the thinning rate ought to increase correspondingly. Yet, the calculated thinning rates appear unaffected.

This is probably due to the shortcomings of using a simple one-dimensional model. In its derivation, the thinning rates were assumed to be approximately constant with distance. But due to the high velocities in the area, the particles at a specific location originate much further upstream, and on their way they may have experienced a large variety of thinning rates. In average, however, they have experienced approximately the same thinning rate no matter the ice thickness at their present position. This also explains why the thinning rates increase towards the margin. As the ice thickness generally decreases towards the margin, the particles ending here have experienced a larger average thinning rate during their journey.

Also the fact that the actual ice flow is three-dimensional is contributing to keep the thinning rates constant along the flight-line. When encountering a bedrock obstruction, the ice may to a large extent flow around it, and not over it as assumed in the two-dimensional approach. As less material is passing over the bulge, the need for a larger thinning rate at this location is diminished.

It is interesting that the best fit when using a kink model implies a negative thinning rate in some areas along the first part of the profile. It signifies that the layers are becoming thicker with depth, which is the case only under very rare circumstances.

The negative thinning rates may be due to bedrock obstacles, which create divergent and convergent flow around them and between them. However, the corresponding influx and outflux of mass mainly affect the deeper layers, and it is questionable how much influence this effect has on the layers used in the fitting process, which are situated in the upper half of the ice sheet. Besides, the bed topography in this area seems to be quite flat.

Another possible explanation is large spatial variations in accumulation rate. Given that the accumulation rates decrease towards the margin, the lower layers, which have originated the furthest upstream, have been affected by the largest average accumulation rate. The effect of this may be large enough to counteract the ice thinning due to ice flow, and it may result in a thickening of the layers with depth. In general, this effect ought to increase with increasing surface velocities. It cannot therefore explain the negative thinning rates observed in the very first part of the flight-line.

An explanation, which also holds for the first part of the flight-line, may be that the lower layers have been formed during a period of increased accumulation. In the one-dimensional model, the accumulation was assumed constant with time during the Holocene, which is not entirely true. The climatic optimum, a warm period lasting from 9,000 to 5,000 years ago, resulted in larger accumulation rates, and it may – at least partly – be the effect of this, which is seen here.

Basal melting is yet another influencing factor. High basal melt rates in an area will contribute to reduce the thinning rates at a given spot. Hence, from the shear presence of the very small thinning rates in the beginning of the flight-line, the existence of high rates of basal melting in this area is very likely.

5.3. Mass flux considerations

From the map in figure 5.6, the surface elevation contours are seen be to relatively flat in the area around the North East Greenland Ice Stream. In general, this is indicative of a small degree of convergent or divergent ice flow (see e.g. *Reeh, 1988*). But, as it will be shown in this section, the high velocities in the area cause the tiny curvature of the surface elevation contours to have a large effect. The flow along the flight-line turns out to be highly convergent, and convergent flow is therefore an important factor to incorporate in any ice sheet model of the area.

To see the importance of taking the convergent flow into account, we will first try to reconstruct the observed surface velocities by using a two-dimensional approximation.

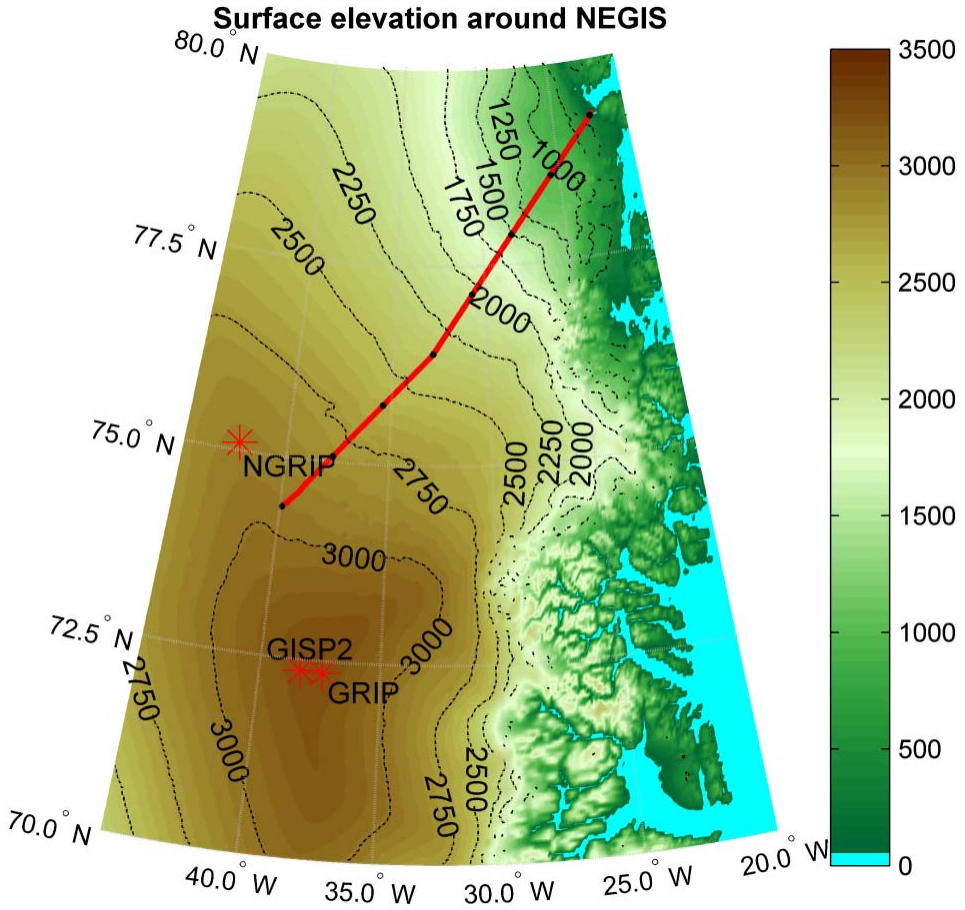

Figure 5.6: Surface elevation in the area around the North East Greenland Ice Stream. The flight-line is marked in red, and also the locations of major drill sites in the area are shown.

5.3.1. A two-dimensional approach

Using a two-dimensional approximation and the principle of mass conservation, the mass flux at a distance x from the beginning of the flowline is given by:

$$Q_{2D}(x,t) = Q_{in}(t) + \int_0^x [a(x,t) - m(x,t)]\, dx$$

Here, a denotes the accumulation rates, and m the basal melt rates. The first term, Q_{in}, has to be taken into account, as the beginning of our flowline does not coincide with the ice divide, where the influx of mass is approximately zero. The present-day value for Q_{in} can be estimated from the distance between the ice ridge and the considered flowline and an educated guess for the average accumulation rate in this area. From section 5.2.2, a proxy is known for the present accumulation rates along the flowline, and for the current purpose we will neglect any occurrence of basal melting, as the amount of this is unknown.

The mass flux can also be given in terms of the depth-averaged horizontal velocity, $\bar{u}(x,t)$:

$$Q_{2D}(x,t) = \bar{u}(x,t) \cdot H(x)$$

By combining the two expressions for Q_{2D} and neglecting m, we have:

$$\bar{u}(x,t) = \frac{Q_{in}(t) + \int_0^x a(x,t)dx}{H(x)}$$

The present-day average horizontal velocity along the flowline can now be calculated using numerical integration, and from knowledge of $\bar{u}$, a proxy for the present surface velocities along the flowline can be obtained. A common convention is to parameterize the depth-averaged horizontal velocity as a fraction of the surface velocity, i.e.:

$$\bar{u} = F \cdot u_s$$

For laminar flow, F equals 0.8 (*Paterson, 2001, p. 252*), but in a real ice sheet, many factors contribute to a larger value. For instance, the increase in temperature down the ice sheet cause relatively more deformation to take place in the basal layers, and hence gives rise to a slightly larger value of F. The most significant factor, however,

is the degree of basal sliding. Total sliding, i.e. $\bar{u}(x,t) = u_s(x,t)$, corresponds to $F = 1$. Paterson estimates a typical value of F to be around 0.95 (*Paterson, 2001*).

In figure 5.7, the present surface velocities calculated under the assumption of two-dimensional flow are plotted together with the observed surface velocities. It is obvious that no matter which value of the conversion factor F is chosen, large differences prevail between the calculated and the observed surface velocities.

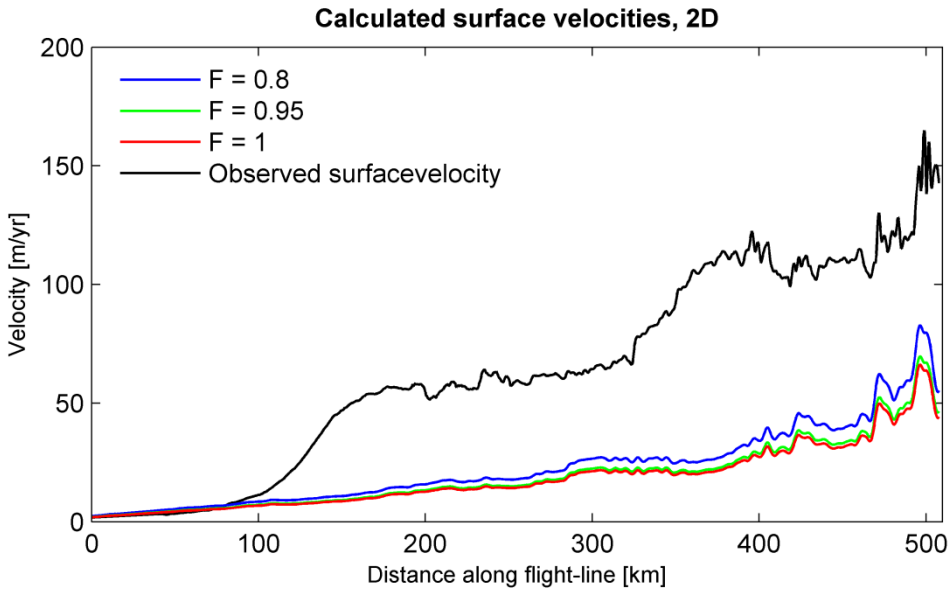

Figure 5.7: A comparison between the observed surface velocities along the flight-line, and the calculated surface velocities assuming 2D flow.

In the beginning of the flowline, the calculated surface velocities correspond rather well to the observed ones. But along with the enormous increases in velocity, discussed in section 4.3.4, the calculated surface velocities cannot keep pace. They remain relatively low towards the margin of the ice sheet, never reaching velocities above 85 m/y. In the last part of the profile (from 370 km and onwards), both the observed and the calculated surface velocity profiles get rougher, and some similarities between the two emerge. For instance, the sudden spikes in the calculated velocity profile around 470 and 500 km from the beginning of the flowline also appear in the observed velocity profile.

In conclusion, some of the small-scale variations of the surface velocity along the flowline can be explained by the mass balance flux due to accumulation pattern and changes in ice thickness. But to explain the vast increase in velocity towards the margin it is necessary to introduce convergent flow along the flowline. Hence, a two-dimensional approximation fails.

5.3.2. A three-dimensional approach

The flight-line along the North East Greenland Ice Stream passes over zones with convergent as well as divergent flow. The amount of convergence/divergence along the flight-line can be estimated by considering $\partial v_s/\partial y$, the change in surface velocity transverse to the flight-line. A negative value can physically be interpreted as the transverse flow slowing down while passing the area (and, if dealing with a flowline, entirely coming to a halt). It consequently corresponds to convergent flow, while a positive value corresponds to divergent flow.

The influx of mass from the sides at a given location is equal to minus the change in flux transverse to the flight-line (this relationship will be derived in section 6.2.3). Using the same equations as in section 5.3.1, but now for the flow component transverse to the flowline, we have $Q_y = H\bar{v} = HFv_s$, with Q_y denoting the total mass flux in the y-direction. The mass influx due to convergent flow is now:

$$M_{influx} = -\frac{\partial Q_y}{\partial y} = -\frac{\partial}{\partial y}(HFv_s) = -HF\frac{\partial v_s}{\partial y}$$

This relationship is only entirely true when dealing with a flowline, such that $v_s = 0$, or in an area with no variations in ice thickness or F-value in the y-direction. Otherwise, terms like $-v_s F\,\partial H/\partial y$ and $-v_s H\,\partial F/\partial y$ ought to have been taken into account as well. However, let us for now assume these terms to be negligible.

One way of estimating the convergence along the flight-line is by using u_s/R, R being the radius of curvature of the surface elevation contours in the area (*Reeh, 1988*). Yet, this method will not be pursued here. Instead, from the detailed map of the surface velocities in the area shown in figure 4.7, p. 30, the derivative of the transverse surface velocity in any point along the flight-line can be calculated by finite differentials. In figure 5.8 is shown how $\partial v_s/\partial y$ varies along the flight-line, together with the corresponding influx of mass. In the further analysis, we use for $\partial v_s/\partial y$ the average value found by this method.

It is seen that $\partial v_s/\partial y$, and therefore also the influx of mass, changes in a very complicated way along the flight-line, attaining both negative and positive values. In the beginning of the flight-line, the influx of mass is small. But around 100 km, there is a large and steady influx of material which continues over more than 50 km. This steady influx gives rise to the first large increase in velocity.

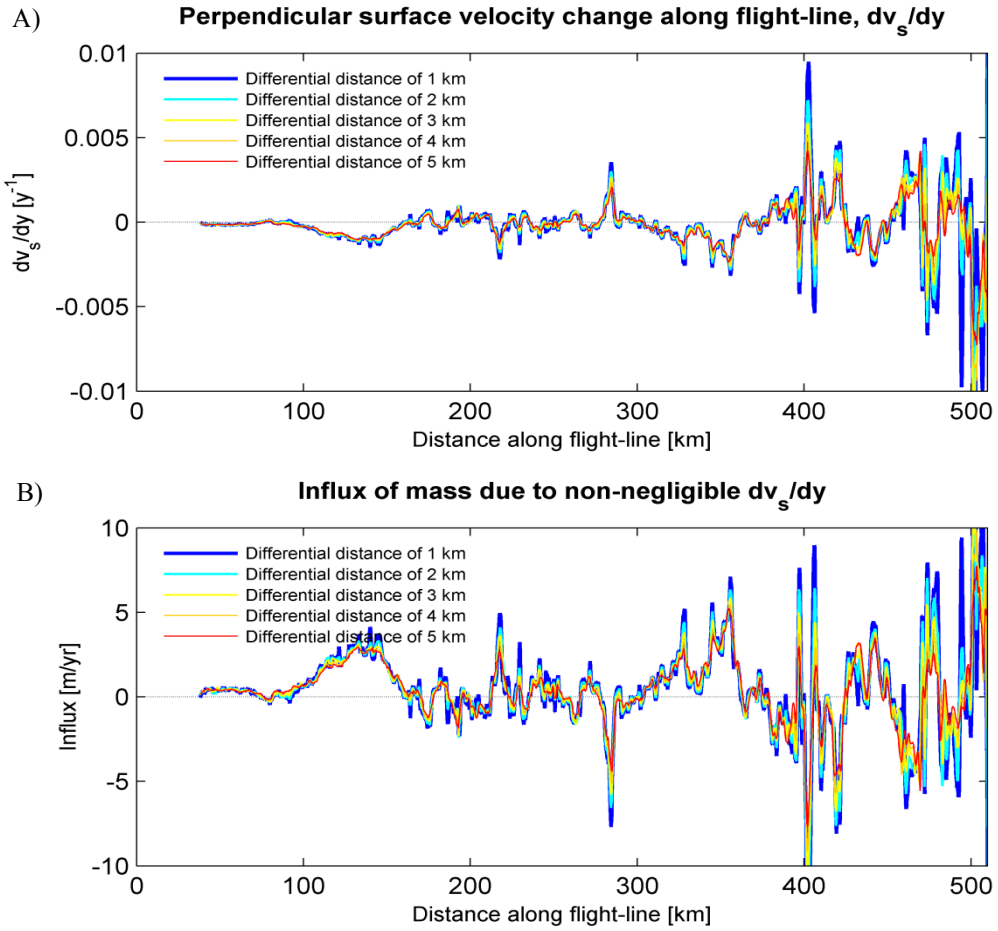

Figure 5.8: A) The transverse velocity change along the flight-line, calculated on basis of the map in figure 4.7. Five different finite differential distances have been applied. Fortunately, it turns out that the resulting outcome is almost unaffected by the choice of differential distance. **B)** The corresponding influx of mass.

Over the next 100 km, $\partial v_s/\partial y$ is heavily fluctuating, but to a large extent the short-lived spikes in both directions cancel each other out. Around 350 km, $\partial v_s/\partial y$ again consistently reaches negative values. This coincides with the second of the major increases in velocity. Along the last 100 km of the flight-line, tremendous fluctuations in $\partial v_s/\partial y$ occurs. However, the lower ice thickness in the area partly counteracts the importance of these oscillations on the resulting in- and outflux of material to the flight-line.

The importance of taking the convergence of the flow into account can be seen from figure 5.8 B. The resulting influx of mass easily reaches several meters per year. These values are to be compared to the magnitude of the accumulation rate (in order of 0.1 m/y) and basal melting terms (in order of 0.01 m/yr), which they greatly exceed.

When also taking the influx of material from the sides into account, the expression for the present mass balance flux along the flowline is given by:

$$Q_{3D}(x) = Q_{in} + \int_0^x \left[a_0 - m - HF\frac{\partial v_s}{\partial y}\right] dx$$

Despite the inclusion of transverse material in this equation, this is still far from a full three-dimensional model. It is based on simple mass balance considerations, and the notion that the ice flow along the flowline contains information on the ice flow transverse to the flowline. It should as such maybe rather have been termed a 2.5D approach.

Using the above expression for the mass balance flux, and disregarding the possible occurrence of basal melting along the flowline, the present surface velocities along the ice stream can be calculated the same way as in the previous section. As seen from figure 5.9, the impact on the calculated surface velocities of the influx of mass due to convergent flow is immense.

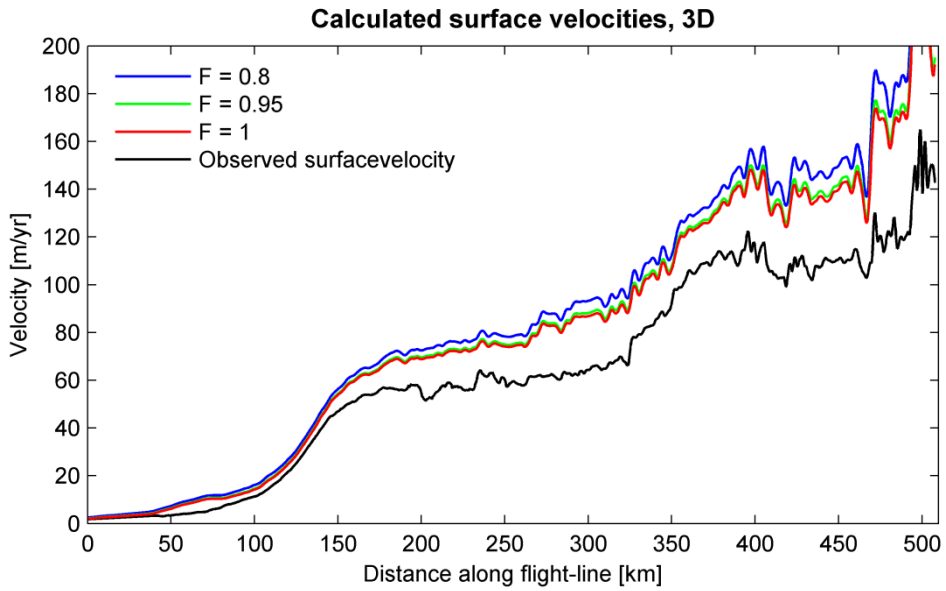

Figure 5.9: Calculated surface velocities along the flowline when assuming three-dimensional flow. Three different values of the *F*-factor have been applied.

Given the large influx of mass due to convergent flow, the enormous increase in surface velocity along the flowline can be explained. In fact, the surface velocities are overestimated. But despite this discrepancy, the calculated and the observed surface velocity profiles are very similar. They have almost the same shape, and even many of the small-scale variations of the observed surface velocity profile are

recovered in the calculated one. This is far better than the results obtained from the two-dimensional approach.

5.3.3. Effects from transverse flow

As it was apparent from figure 5.9, the surface velocities were overestimated by the preceding three-dimensional analysis of the mass flux along the flowline. This disagreement can stem from many factors. For instance, the effect of the transverse surface velocity component was completely disregarded. The effect of transverse flow on the surface velocities depends on to which degree the terms $\partial H/\partial y$ and $\partial F/\partial y$ are negligible.

The North East Greenland Ice Stream is aligned along the axis of a broad trench, and ice is transported to the ice stream from the surroundings. To a first approximation, this implies that the particles usually will flow in direction of greater ice thickness, since this will be towards the ice stream centreline. Hence, away from a true flowline the term $v_s \cdot \partial H/\partial y$ will most often be positive. The correction term to be added to the mass balance equation due to a changing ice thickness transverse to the flight-line is given by $-v_s F\, \partial H/\partial y$. The general effect of this term is therefore to decrease the amount of material which is to be transported downstream, thus decreasing the required surface velocities. A small scale analysis shows that it may indeed be a rather important term. The magnitudes of the involved parameters are:

$$v_s \sim 10 \frac{m}{yr} \quad , \quad \frac{\partial H}{\partial y} \approx \frac{\partial H}{\partial x} \sim 10^{-2} \quad , \quad F \sim 1$$

Hence, the order of magnitude for this correction term amounts to:

$$v_s F \frac{\partial H}{\partial y} \sim 10^{-1}\, m/yr$$

This is of the same order of magnitude as the accumulation rates and at least one order of magnitude larger than the basal melt rates. However, it is still only a small fraction of the influx of mass due to the term $\partial v_s/\partial y$ (figure 5.8 B).

Another factor, which may contribute to the importance of transverse flow for the calculated surface velocities, is non-negligible values of $\partial F/\partial y$. Due to the increased flow along the ice stream, it is very likely that the ice stream is exactly situated where the value of F is largest. Therefore, the term $v_s \cdot \partial F/\partial y$ may be positive along most of the flight-line. The correction term to be added to the mass balance equation

equals $-v_s H\, \partial F/\partial y$, and hence also this factor may contribute to decrease the calculated surface velocities. The magnitudes of the involved parameters are here:

$$v_s \sim 10\,\frac{m}{yr} \quad , \quad H \sim 10^3\, m \quad , \quad \frac{\partial F}{\partial y} \approx \frac{\partial F}{\partial x} \sim 10^{-5}$$

The magnitude estimate for $\partial F/\partial x$ is derived in chapter 10, where also its possible influence on the calculated surface velocities is discussed. An order of magnitude estimate for this correction term is now:

$$v_s H\, \partial F/\partial y \;\sim\; 10^{-1}\, m/yr$$

Thus, both two terms due to the transverse velocity component along the flight-line act to decrease the surface velocities, and they potentially have just as large an effect (but opposite) as the accumulation rates along the flight-line.

In figure 5.10, the surface velocities along the flight-line have been calculated under the assumption that the effects of the above mentioned correction terms arising from the transverse velocity component cancel out the effect of the accumulation along the flight-line. This conjecture rests on the assumption that the two terms are of the same order of magnitude, but opposite in sign. The result is a surprisingly good fit between the calculated surface velocity profile and the observed velocities.

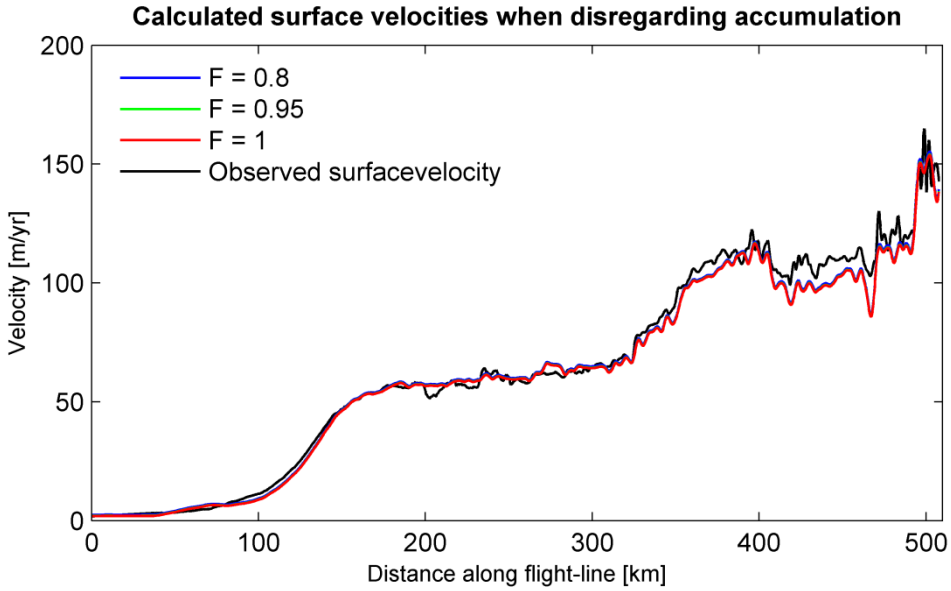

Figure 5.10: Calculated surface velocities when assuming three-dimensional flow, and assuming the effect of the accumulation along the flight-line to be cancelled by the effects of the transverse flow component. The blue and green lines are difficult to see, as they are situated almost directly behind the red line.

Other factors may also contribute to explain the discrepancy between the observed and calculated surface velocity profile. As mentioned, $\partial F/\partial x$ may be influential (see chapter 10). Discrepancies may also arise from smaller accumulation rates than anticipated from the one-dimensional model and/or the existence of large basal melt rates in the area. Besides, as no surface velocity data exists for the first part of the flight-line, two-dimensional flow was assumed to exist here. Any convergent or divergent flow in this small area may also affect the calculated surface velocities.

From these preliminary considerations of which factors are the most influential for the flow pattern along the North East Greenland Ice Stream, we now proceed to a more sophisticated analysis by use of a three-dimensional flowline model in combination with a Monte Carlo analysis.

Chapter 6

A flowline model

6.1. Employing a Dansgaard-Johnsen model

As we wish to reconstruct how ice particles have moved from the time they were deposited on the surface of the ice sheet to their present position down the ice, the velocity field in the ice sheet must be known. In this thesis, a modified Dansgaard-Johnsen model is used.

In the Dansgaard-Johnsen model (also commonly referred to as the kink model), the horizontal velocity field is described by a constant horizontal velocity (u_s) in the upper part of the ice sheet down to the kink height, h. Below the kink height, the horizontal velocity decreases linearly towards the base of the ice sheet (see figure 6.1). In the original Dansgaard-Johnsen model, the horizontal velocity was set to zero at the base of the ice sheet, thus implying no basal sliding (*Dansgaard and Johnsen, 1969*). However, this was later found to be a rather poor assumption, in particular in areas with basal melting, and the currently used Dansgaard-Johnsen model is often extended with a basal melting term and allows for basal sliding at the bed.

Basal sliding can be taken into account by defining a parameter F_B, given as the fraction of basal velocity, u_B, compared to the surface velocity, u_s:

$$F_B \equiv \frac{u_B}{u_s}$$

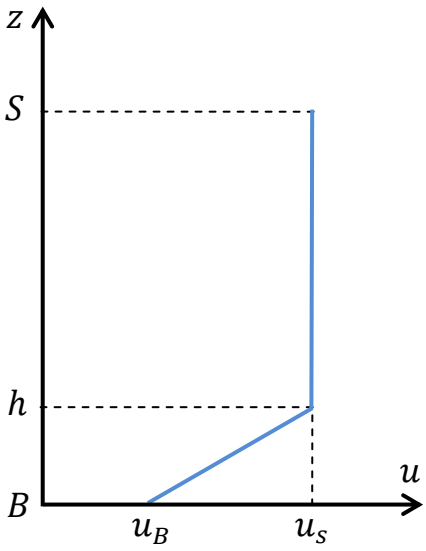

Figure 6.1: The horizontal velocity profile of the modified Dansgaard-Johnsen model.

With this definition, the following expression for the horizontal velocity profile, $u(z)$, is obtained:

$$u(z) = \begin{cases} u_s, & h \leq z < S \\ u_s \cdot \left(F_B + \dfrac{1 - F_B}{h - B} \cdot (z - B) \right), & B < z \leq h \end{cases} \tag{6.1}$$

Here, B is the bed, S is the surface of the ice sheet, and h is the kink height. All of these quantities, as well as u_s and F_B, depend on time and place.

The assumption that the horizontal velocity profile at any given location can be described by a Dansgaard-Johnsen type of model is a central assumption, which we will hold true throughout the rest of the thesis. Despite its simple appearance and its empirical nature, it has in many cases been found to describe the velocity field in an ice sheet rather well (see e.g. *Paterson, 2001, p. 252*). And its simplicity makes it ideal for use in Monte Carlo searches, where the calculation of the velocity field must not be computational heavy.

6.2. Equations for the flow model

6.2.1. The vertical velocity component

Consider the continuity equation, which is simply a statement of conservation of mass:

$$-\frac{\partial \rho}{\partial t} = \nabla \cdot \rho \boldsymbol{v} = \frac{\partial(\rho u)}{\partial x} + \frac{\partial(\rho v)}{\partial y} + \frac{\partial(\rho w)}{\partial z}$$

Here, ρ is the density of the material, and $\boldsymbol{v} = (u, v, w)$ is the velocity vector of the ice, measured in a Cartesian coordinate system. As ice is almost incompressible, its density can be assumed constant in time and space, and ρ can be removed from the equation. Hereby, the following relationship is obtained, which is to hold for all values of x, y, z and t:

$$0 = \nabla \cdot \boldsymbol{v} = \frac{\partial u}{\partial x} + \frac{\partial v}{\partial y} + \frac{\partial w}{\partial z}$$

If it is known how $\partial u/\partial x$ and $\partial v/\partial y$ changes down an ice column, this equation can be integrated upwards from the bed, B, to find $w(z)$:

$$w(z) - w(B) = \int_B^z \frac{\partial w}{\partial z} dz = -\int_B^z \left(\frac{\partial u}{\partial x} + \frac{\partial v}{\partial y}\right) dz$$

The downwards velocity at the base of an ice sheet, $w(B)$, is mainly due to basal melting, m. However, in case of irregular bedrock topography, a non-negligible contribution to the downwards velocity arises from basal sliding over the bedrock. In a general setting, the kinematic boundary condition at the bed reads (*Pattyn, 2003*):

$$w(B) = \frac{\partial B}{\partial t} + \boldsymbol{v_B} \cdot \nabla B - m$$

The term $\boldsymbol{v_B} = (u_B, v_B)$ denotes the basal sliding velocity in respectively the x- and the y-direction. The contribution from a possible change in bedrock topography over time is considered negligible, and when dealing with a flowline v_B equals zero. The above equation is then reduced to:

$$w(B) = u_B \cdot \frac{\partial B}{\partial x} - m$$

The vertical velocity can thus be obtained from the following equation:

$$w(z) = u_B \cdot \frac{\partial B}{\partial x} - m - \int_B^z \left(\frac{\partial u}{\partial x} + \frac{\partial v}{\partial y}\right) dz \tag{6.2}$$

6.2.2. Coordinate transformation

The application of a Dansgaard-Johnsen model is only really appropriate for areas in which the basal topography does not change too much. In mountainous areas, the ice flow is heavily influenced by the bedrock, and a complicated flow pattern may exist. It may e.g. no longer be a good approximation to assume the direction of the velocity field to be unchanged downwards an ice column (as assumed in a flowline model). Nevertheless, we intend to use this simple model all along the flowline.

For numerical convenience, a non-dimensional vertical coordinate, ζ, is introduced in order to account for the ice thickness variations along the flowline in the best possible way:

$$\zeta \equiv \frac{z - B}{H} \tag{6.3}$$

Applying the coordinate transformation which maps $(x, y, z) \curvearrowright (x', y', \zeta)$, a normalized coordinate system is generated, in which the base of the ice sheet is situated at $\zeta = 0$ and the surface of the ice sheet is positioned at $\zeta = 1$, see figure 6.2. The new x' and y' axes are perpendicular to ζ.

In our new coordinate system, the partial derivatives of a function f are given by:

$$\frac{\partial f}{\partial x} = \frac{\partial f}{\partial x'}\frac{\partial x'}{\partial x} + \frac{\partial f}{\partial y'}\frac{\partial y'}{\partial x} + \frac{\partial f}{\partial \zeta}\frac{\partial \zeta}{\partial x}$$

Similar expressions are obtained for $\partial f/\partial y$ and $\partial f/\partial z$.

As long as the surface and bedrock gradients are not too large, we can set $\partial x'/\partial x \cong 1$ and $\partial y'/\partial x \cong 0$. In this case, the above equation reduces to:

$$\frac{\partial f}{\partial x} = \frac{\partial f}{\partial x'} + \frac{\partial f}{\partial \zeta}\frac{\partial \zeta}{\partial x} \tag{6.4}$$

Again, a similar expression applies for $\partial f/\partial y$ (but not for $\partial f/\partial z$).

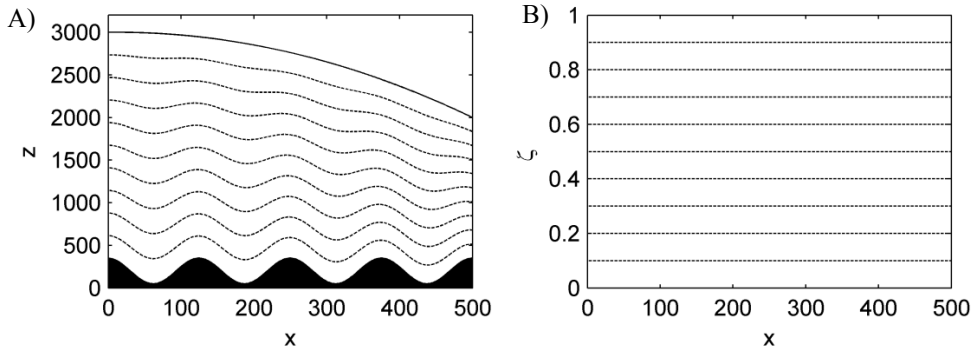

Figure 6.2: Introduction of a normalized coordinate system. **A)** Before transformation. The dashed lines indicate surfaces with constant ζ. **B)** The same surfaces after the transformation.

When taking the partial derivative of ζ with respect to x, the variation of bed topography and ice thickness along the flowline must be taken into account:

$$\frac{\partial \zeta}{\partial x} = \frac{-\frac{\partial B}{\partial x} \cdot H - \frac{\partial H}{\partial x} \cdot (z - B)}{H^2} = -\frac{\frac{\partial B}{\partial x} + \frac{\partial H}{\partial x} \cdot \zeta}{H} = -\frac{\frac{\partial B}{\partial x'} + \frac{\partial H}{\partial x'} \cdot \zeta}{H} \tag{6.5}$$

The last equality holds, as neither B nor H are dependent on ζ. Now consider the function $u(x, z, t)$. By combining equation (6.4) and (6.5), the following expression for $\partial u / \partial x$ is obtained:

$$\frac{\partial u}{\partial x} = \frac{\partial u}{\partial x'} - \frac{\partial u}{\partial \zeta} \cdot \frac{\frac{\partial B}{\partial x'} + \frac{\partial H}{\partial x'} \cdot \zeta}{H} \tag{6.6}$$

To simplify matters, let us define a parameter k, the fractional kink height, as the kink height in this normalized coordinate system:

$$k \equiv \frac{h - B}{H}$$

In our new coordinate system, the horizontal velocity according to the modified Dansgaard-Johnsen model, equation (6.1), is now given by:

$$u(\zeta) = u_s \cdot \Phi(\zeta) = u_s \cdot \begin{cases} 1 & , \quad k \leq \zeta < 1 \\ F_B + \frac{1 - F_B}{k} \cdot \zeta, & 0 < \zeta \leq k \end{cases} \tag{6.7}$$

Here, the function $\Phi(\zeta)$ has been introduced. It is termed the shape function, as it conveys information about the shape of the velocity profile. The shape function will be assumed to be slowly varying with distance in this normalized coordinate system, such that $\partial\Phi/\partial x' \cong 0$. (Note that this is not the same as assuming $\partial\Phi/\partial x \cong 0$). This is an assumption commonly made, and it is presumed to hold quite well under most circumstances (*Reeh, 1988*). It implies that neither k nor F_B are allowed to change rapidly with distance. It is probably a reasonable assumption that $\partial k/\partial x'$ is negligible, but the question is whether $\partial F_B/\partial x'$ is negligible as well. This issue is discussed in chapter 10.

An expression for $\partial u/\partial x$ can now be derived using the new coordinates. When setting $\partial\Phi/\partial x' \cong 0$, we obtain for $\partial u/\partial x'$ (see equation (6.7)):

$$\frac{\partial u}{\partial x'} = \frac{\partial u_s}{\partial x'} \cdot \Phi + u_s \cdot \frac{\partial \Phi}{\partial x'} \cong \frac{\partial u_s}{\partial x'} \cdot \Phi$$

And as u_s does not depend on ζ, $\partial u/\partial\zeta$ becomes:

$$\frac{\partial u}{\partial \zeta} = u_s \frac{\partial \Phi}{\partial \zeta} = u_s \cdot \begin{cases} 0 \quad , & k \le \zeta < 1 \\ \dfrac{1 - F_B}{k}, & 0 < \zeta \le k \end{cases}$$

Inserting these two equations into equation (6.6) leads to the following expression for $\partial u/\partial x$:

$$\frac{\partial u}{\partial x} = \begin{cases} \dfrac{\partial u_s}{\partial x'} \quad , & k \le \zeta < 1 \\ \dfrac{\partial u_s}{\partial x'} \cdot \left(F_B + \dfrac{1 - F_B}{k} \cdot \zeta \right) - u_s \cdot \dfrac{1 - F_B}{k} \cdot \dfrac{\dfrac{\partial B}{\partial x'} + \dfrac{\partial H}{\partial x'} \cdot \zeta}{H}, & 0 < \zeta \le k \end{cases}$$

Assuming the velocity in the y-direction to be described by the same Dansgaard-Johnsen model, a similar equation holds for $\partial v/\partial y$. When considering a flowline, v_s equals zero, and $\partial v/\partial y$ becomes:

$$\frac{\partial v}{\partial y} = \begin{cases} \dfrac{\partial v_s}{\partial y'} \quad , & k \le \zeta < 1 \\ \dfrac{\partial v_s}{\partial y'} \cdot \left(F_B + \dfrac{1 - F_B}{k} \cdot \zeta \right), & 0 < \zeta \le k \end{cases}$$

Inserting $u_B = F_B u_s$ and using the new normalized coordinates, the vertical velocity at a specific location (equation (6.2)) is given by:

$$w(\zeta) = F_B u_s \frac{\partial B}{\partial x'} - m - H \int_0^{\zeta} \left(\frac{\partial u}{\partial x} + \frac{\partial v}{\partial y} \right) d\zeta \tag{6.8}$$

By inserting the derived expressions for $\partial u/\partial x$ and $\partial v/\partial y$ into (6.8) and integrating, an expression for the vertical velocity can now be derived in terms of the new coordinates. But we also wish to know the normalized velocities. The normalized vertical velocity (ω) is the total derivative of ζ with time, and it can be found from u and w by use of the chain rule:

$$\omega = \frac{d\zeta}{dt} = \frac{\partial \zeta}{\partial t} + \frac{\partial \zeta}{\partial x}\frac{dx}{dt} + \frac{\partial \zeta}{\partial y}\frac{dy}{dt} + \frac{\partial \zeta}{\partial z}\frac{dz}{dt} = \frac{\partial \zeta}{\partial t} + \frac{\partial \zeta}{\partial x}u + \frac{\partial \zeta}{\partial z}w \tag{6.9}$$

Assuming pseudo-steady state, such that there are no changes with time in B and S (and therefore also in H), we have $\partial \zeta/\partial t = 0$. And from differentiation of equation (6.3) with respect to z, we get $\partial \zeta/\partial z = 1/H$. When inserting these and the expression for $\partial \zeta/\partial x$ (equation (6.5)) into equation (6.9), ω is given as:

$$\omega = -\frac{\frac{\partial B}{\partial x'} + \frac{\partial H}{\partial x'} \cdot \zeta}{H} u + \frac{1}{H} w$$

The resulting equations for ω are:

$$\begin{aligned} \omega(\zeta \le k) &= -\frac{m}{H} - \left(\frac{\partial u_s}{\partial x} + \frac{\partial v_s}{\partial y} + \frac{u_s}{H}\frac{\partial H}{\partial x} \right) \cdot \left(F_B \zeta + \frac{1}{2}(1 - F_B)\frac{\zeta^2}{k} \right) \\ \omega(\zeta \ge k) &= -\frac{m}{H} - \left(\frac{\partial u_s}{\partial x} + \frac{\partial v_s}{\partial y} + \frac{u_s}{H}\frac{\partial H}{\partial x} \right) \cdot \left(\zeta - \frac{1}{2}k(1 - F_B) \right) \end{aligned} \tag{6.10}$$

The horizontal velocity is unaffected by this change in coordinate system. This can be seen by substituting x' for ζ in equation (6.9), and using the relationships $\partial x'/\partial x \cong 1$, $\partial x'/\partial y \cong 0$, $\partial x'/\partial z \cong 0$ and $\partial x'/\partial t \cong 0$. The velocity in the x'-direction is now given by:

$$u' = \frac{dx'}{dt} = \frac{\partial x'}{\partial t} + \frac{\partial x'}{\partial x}\frac{dx}{dt} + \frac{\partial x'}{\partial y}\frac{dy}{dt} + \frac{\partial x'}{\partial z}\frac{dz}{dt} = \frac{dx}{dt} = u$$

6.2.3. Equations for the surface velocity

In the preceding section, equations for the velocity components in a normalized coordinate system were derived under the assumptions of pseudo-steady state and a slowly varying shape function with distance. But to calculate the velocity field in an ice sheet using these equations, we need to know how u_s and $\partial u_s/\partial x$ change with time and location along the flowline.

Despite our knowledge of the present surface velocities along the flowline, we may – due to data uncertainties – only have limited knowledge of $\partial u_s/\partial x$. In order to get a better estimate of $\partial u_s/\partial x$, an expression for this quantity will now be derived based on the equations governing the local mass balance in an ice sheet.

Consider a column of ice, having the thicknesses δx and δy and reaching from bedrock to the surface (see figure 6.3). During a small time interval, δt, the amount of material added to this ice column by precipitation is $a \cdot \delta x \delta y \delta t$, and the amount of ice lost due to basal melting is $m \cdot \delta x \delta y \delta t$. Material is also added and disappearing through the faces of the column. The amount of material added to the face perpendicular to the x-axis is equal to $Q_x(x, y, t) \cdot \delta y \delta t$, where Q_x denotes the total flux of material in the x-direction, while the amount of material leaving is $Q_x(x + \delta x, y, t) \cdot \delta y \delta t$. Hence, the total amount of material accumulated in the column during the time interval δt due to the flux of material in the x-direction is given by:

$$Q_x(x, y, t) \cdot \delta y \delta t - Q_x(x + \delta x, y, t) \cdot \delta y \delta t$$
$$= \left[Q_x(x, y, t) - \left(Q_x(x, y, t) + \frac{\partial Q_x}{\partial x}\delta x\right)\right] \cdot \delta y \delta t = -\frac{\partial Q_x}{\partial x}\delta x \delta y \delta t$$

A similar equation holds for the material accumulated in the column due to Q_y, the flux in the y-direction.

As the density of ice is assumed constant, any accretion of mass at a specific location over time must correspond to an increase in ice thickness; $\partial H/\partial t \cdot \delta x \delta y \delta t$. Using the principle of conservation of mass, the following equation is then obtained when dividing by the common factors $\delta x \delta y \delta t$:

$$a(x, y, t) - m(x, y, t) - \frac{\partial Q_x}{\partial x}(x, y, t) - \frac{\partial Q_y}{\partial y}(x, y, t) = \frac{\partial H}{\partial t}(x, y, t) \quad (6.11)$$

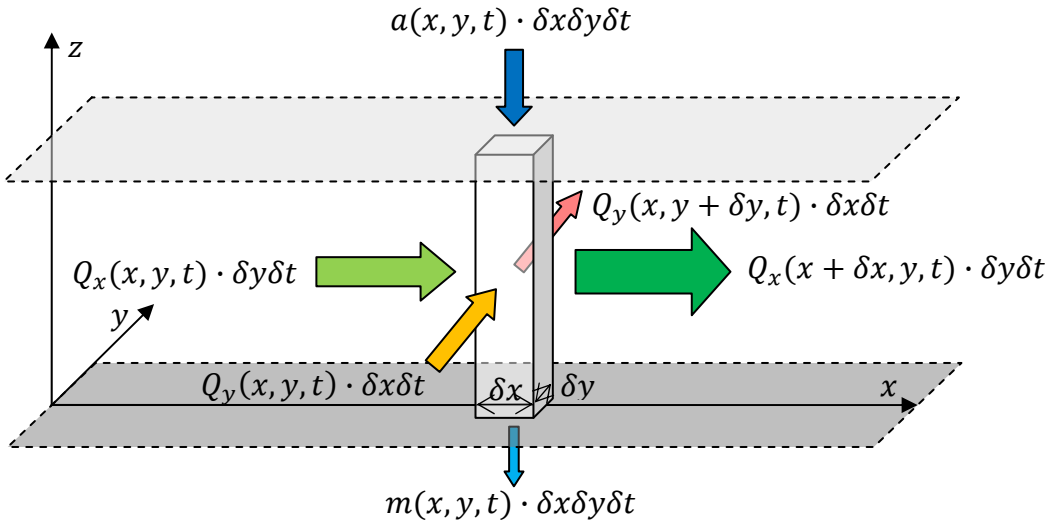

Figure 6.3: Conservation of mass of an ice column with no changes in thickness over time.

When dealing with a Dansgaard-Johnsen flow model, an analytical expression for the flux in the x-direction can be calculated to:

$$Q_x = H\cdot\bar{u} = H\cdot Fu_s = u_sH\left(1-\frac{1}{2}k(1-F_B)\right) \tag{6.12}$$

Here, $\bar{u}$ denotes the mean horizontal velocity in the x-direction, and F is as given in section 5.3. Under the assumption of a slowly varying shape function with distance (i.e. assuming $\partial k/\partial x$ and $\partial F_B/\partial x$ to be negligible), $\partial Q_x/\partial x$ is given by:

$$\frac{\partial Q_x}{\partial x} = \left(1-\frac{1}{2}k(1-F_B)\right)\left(\frac{\partial u_s}{\partial x}H + u_s\frac{\partial H}{\partial x}\right)$$

A similar expression holds for $\partial Q_y/\partial y$, but once again we can set $v_s = 0$, and reduce the expression for $\partial Q_y/\partial y$ to:

$$\frac{\partial Q_y}{\partial y} = \left(1-\frac{1}{2}k(1-F_B)\right)\frac{\partial v_s}{\partial y}H$$

Inserting these expressions for $\partial Q_y/\partial y$ and $\partial Q_x/\partial x$ into equation (6.11), and solving for $\partial u_s/\partial x$, we get:

$$\frac{\partial u_s}{\partial x} = \frac{a - m - \frac{\partial H}{\partial t}}{\left(1 - \frac{1}{2}k(1 - F_B)\right)H} - \frac{1}{H}\frac{\partial H}{\partial x}u_s - \frac{\partial v_s}{\partial y} \tag{6.13}$$

However, just as in the previous section, the ice sheet will be assumed to be in pseudo-steady state, such that its thickness does not change over time (i.e. $\partial H/\partial t$ is negligible). By inserting this expression for the rate of change of the surface velocity into equations (6.10), the dependency of the vertical velocity component on the term $\partial u_s/\partial x$ is eliminated.

The expression for $\partial u_s/\partial x$ can also be used to determine u_s along the flowline. Equation (6.13) is a first-order linear differential equation in u_s with the solution:

$$u_s(x) = e^{-\theta}\left[\int e^{\theta}\left(\frac{a - m}{H - \frac{1}{2}kH(1 - F_B)}\right)dx + c\right],$$

$$\theta = \int \left(\frac{1}{H}\frac{\partial H}{\partial x} - \frac{\partial v_s}{\partial y}\right)dx$$

Given knowledge of the mass balance along the flowline and the surface velocity in the beginning of the flowline, this expression can be solved by numerical integration to give the surface velocities along the flowline.

For the flow model, we have chosen to use these calculated velocities rather than the observed ones, despite the fact that this calculation slightly overestimates the surface velocities (see section 5.3.2). Subsequent comparison to the observed velocities then gives an indication of how well the model is working. In the future, it may be possible to use the discrepancy between modelled and calculated values of the surface velocity directly in the Monte Carlo search, in order to optimize the model also with respect to these data.

6.3. Time variations of the velocity field

It is probably a rather good approximation to consider the basal melt rates, relative basal sliding and the kink height to be constant in time. However, this is not a good approximation for the accumulation rates. It is known from ice core data that accumulation rates are very dependent on climate, with high accumulation rates during periods of warm climate, and low accumulation rates during cold climate regimes. The accumulation rates during the last glacial are estimated to have been less than half their present-day value (see e.g. figure 9.5, p. 97). As furthermore the accumulation rate is one of the most important flow parameters, its temporal change must be taken into account the best way as possible.

6.3.1. Reconstructing past accumulation rates

We employ the same type of accumulation model as used by Johnsen et al. to date the GRIP ice core (*Johnsen et al., 1995*). This accumulation model is based on an empirical relationship between $\delta^{18}O$ values (a climate proxy) and past accumulation rates, and it postulates an exponential second-degree relationship between the two:

$$a(t) = a_0 \cdot \exp\left(k_2\left(\delta^{18}O(t) - \delta^{18}O_w\right) + \frac{1}{2}k_1\left(\delta^{18}O(t)^2 - \delta^{18}O_w^2\right)\right)$$
$$k_1 = \frac{c_1 - c_2}{\delta^{18}O_w - \delta^{18}O_c} \qquad k_2 = c_1 - \delta^{18}O_w \cdot k_1 \tag{6.14}$$

Here, a_0 denotes the present accumulation rate, $\delta^{18}O_w = -35.2‰$ is the present-day $\delta^{18}O$ value (which is taken to be a typical value during the Holocene) and $\delta^{18}O_c = -40‰$ is a typical value during cold periods. The physical meaning of the two parameters c_1 and c_2 can be seen by differentiation of equation (6.14):

$$c_1 = \frac{1}{a}\frac{\partial a}{\partial \delta^{18}O}\bigg|_{\delta^{18}O_w} \qquad c_2 = \frac{1}{a}\frac{\partial a}{\partial \delta^{18}O}\bigg|_{\delta^{18}O_c}$$

I.e., the two constants represent the relative change in accumulation with $\delta^{18}O$ in warm and cold climate respectively.

The onset of the North East Greenland Ice Stream is situated close to the location of the NorthGRIP ice core. The $\delta^{18}O$ signal in the ice core provides a proxy for how the climate in the area has changed back in time. Assuming the past climate to have changed in a similar way along the ice stream, the $\delta^{18}O$ values from NGRIP can be

used to reconstruct how past accumulation rates have changed here as well. A corrected $\delta^{18}O$ curve for NGRIP, which takes into account past changes in seawater $\delta^{18}O$ due to changes in global ice volume, has been employed (*Waelbroeck et al., 2002*).

At NGRIP, the slope of the accumulation rates during the Holocene is $c_1 = 8.4 \pm 0.4‰^{-1}$. This value is similar to what is calculated thermodynamically for the present-day climate ($8‰^{-1}$). The slope for the accumulation rates in cold climate at this location is calculated to be $c_2 = 14.1 \pm 0.1‰^{-1}$ (*S. J. Johnsen, pers. comm.*). The difference is caused by the disparity of the prevailing climate systems during the two periods.

When this relationship was used to date the NGRIP ice core (the ss09sea timescale), the value for c_2 was taken to be $18‰^{-1}$. This was the value found for GRIP, and the corresponding timescale turned out to fit well with the GICC05 timescale. The difference between these two values for c_2 is probably due to a deficiency of the model to explain the changes in accumulation rates during the transition to the Holocene (*S. J. Johnsen, pers. comm.*).

The value of the constants c_1 and c_2 depends on the location. As the North East Greenland Ice Stream is situated in a different climatic zone from Central Greenland (and hence NGRIP), it is likely that the weather pattern, and hence the amount of precipitation, has changed differently with climate at the two locations. In this way, the value of the two constants, c_1 and c_2 may to a good approximation be treated as constants along the ice stream, while having different values than in Central Greenland. The (average) values of these two constants along the NEGIS are unknown, and are to be determined in the Monte Carlo analysis.

When treating c_1 and c_2 as constant along the flowline, we have:

$$a(x,t) = a_0(x) \cdot f(t),$$

$$f(t) = \exp\left(k_2\left(\delta^{18}O(t) - \delta^{18}O_w\right) + \frac{1}{2}k_1\left(\delta^{18}O(t)^2 - \delta^{18}O_w^2\right)\right)$$

6.3.2. Effects of changing accumulation rates

As the ice thickness is assumed to remain constant in time, the ice sheet must react instantaneously to changes in climate. Consequently, an increase in accumulation rate will immediately give rise to increased mass flux and surface velocities

downstream. Assuming a constant kink height with time, the surface velocity must increase equally much as the accumulation rates:

$$u_s(x,t) = u_s(x,t_0) \cdot f(t)$$

In turn, the changing surface velocities over time affects $\partial u_s/\partial x$ and $\partial v_s/\partial y$:

$$\frac{\partial u_s}{\partial x}(x,t) = \frac{\partial u_s}{\partial x}(x,t_0) \cdot f(t) \qquad \frac{\partial v_s}{\partial y}(x,t) = \frac{\partial v_s}{\partial y}(x,t_0) \cdot f(t)$$

These calculations disregard the influence of basal melting, which anyway is small compared to the uncertainties involved when determining the past accumulation rates.

With the combined equations of this and the previous sections, the velocity field at any time and place can be calculated from knowledge of the accumulation rates, basal melt rates, kink height and the relative amount of basal sliding. For any given set of these parameters, we are now able to track a particle originating at the surface down the ice sheet to its present position.

6.4. Parameterization and prior knowledge of the flow parameters

6.4.1. Present accumulation rates

In the Monte Carlo analysis, the present accumulation rates will be derived at six locations along the North East Greenland Ice Stream with a mutual distance of 100 km. Between the data points, linear interpolation will be used. From the accumulation rates calculated by use of the one-dimensional model in section 5.2, we have a preconception value of the accumulation rates at these six locations (figure 6.4).

The one-dimensional accumulations rates are only rough estimates, and hence their corresponding uncertainties may be large. As a very conservative estimate, the average accumulation rates at the six locations are assumed to be known with an accuracy corresponding to three times the standard deviation of the data from the average value in a given interval. In this way, they do not constrain the Monte Carlo analysis very much.

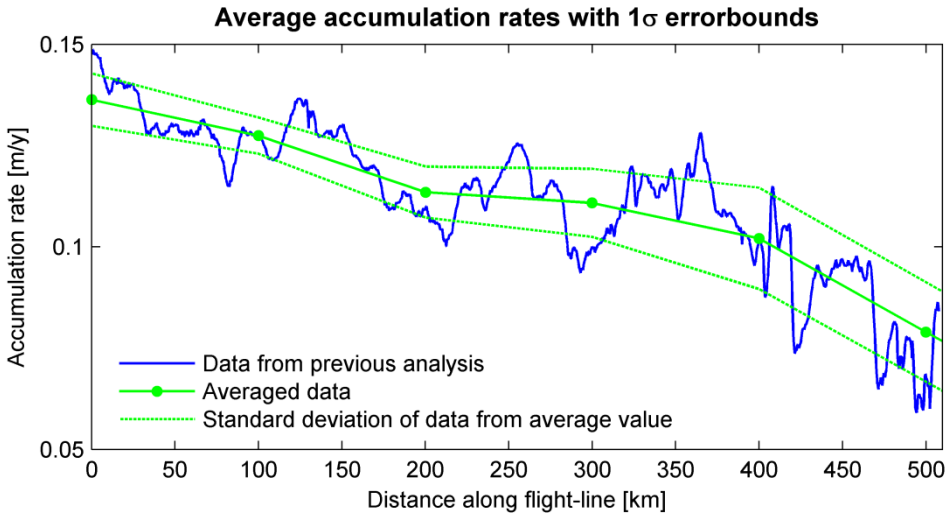

Figure 6.4: Average accumulation rates along the NEGIS as found by the one-dimensional model, and the corresponding 1σ-uncertainties.

6.4.2. Basal melt rates

The basal melt rates are also assumed to display a linear trend in between the actual data points, which are located with a mutual distance of 25 km. This is much smaller than the distance between the accumulation data points, as the basal melt rates are expected to change much more rapidly with distance. Also, the main focus of the

Monte Carlo simulation is to determine the basal melt rates along the North East Greenland Ice Stream. It is therefore only natural that we allow this parameter to be determined very carefully along the ice stream.

One could argue that the basal melt rates ought to be determined at even smaller length-scales. In his study, Steen-Larsen (*Steen-Larsen, 2007*) assumes a distance of only 10 km, which he finds is necessary to resolve the features of the internal layering. However, due to the extensive computer time needed when using such a high resolution, it was necessary to use the above mentioned distance of 25 km between the acquired data for the basal melt rates.

6.4.3. Basal sliding

Basal sliding may to a large extent be explained by the occurrence of basal melt water lubricating the bedrock. We will therefore assume it possible to estimate the amount of basal sliding from the basal melt rates along the flowline.

However, recent research has found basal sliding to be a much more widespread phenomenon than previously thought. When fitting a Dansgaard-Johnsen model to the data from the Greenland ice cores, the best fit is usually obtained when using a basal sliding factor of about 15-20% percent. Astonishingly, this is regardless of the conditions at the base of the ice sheet, and applies both at locations such as Dye 3, with very cold conditions at the bed, and at NGRIP, where basal melting occurs (*S. J. Johnsen, pers. comm.*).

Thus, it seems reasonable to believe that even in areas with no basal melt water the ice is sliding. The "sliding" does not necessarily take place at the ice-bedrock interface, but may also take place in the lowest 10s of meters of the ice sheet itself, where lots of impurities make the ice soft. Fast deformation in this soft layer may be what is recognised as sliding. Indeed, the existence of silty ice in itself is a sign of the sliding of ice over the bedrock, while blending rocks from the bedrock into the ice.

We hence wish to parameterize the basal sliding factor, F_B, along the flowline from the basal melt rates in such a way that an increase in melt water production results in a higher amount of sliding. At locations where no melting occurs (in the limit $m \to 0$), the potential non-zero amount of basal sliding is denoted F_{B0}:

$$F_B(m = 0) = F_{B0}$$

In the other limit, where lots of water is present beneath the ice sheet (i.e. for $m \to \infty$), the ice may start to slide as an ice cube over the bedrock, having the same

velocity at the bed as at the surface. This corresponds to a value of $F_B = 1$. A possible functional dependence of F_B with m, which satisfies these limits, is:

$$F_B(m) = 1 - \exp(\kappa - \lambda \cdot m), \qquad \kappa \equiv \ln(1 - F_{B0}) \tag{6.15}$$

The parameter F_{B0} must fulfil the conditions $0 \leq F_{B0} < 1$, and in order to have an increasing function with m, we must have $\lambda > 0$. (For $\lambda = 0$, basal melt water has no impact on the basal velocity). In figure 6.5 is shown the relationship between basal melt rates and basal sliding when using this parameterization for different values of F_{B0} and λ.

The parameter λ signifies to which degree a certain amount of water is able to increase the basal flow. The above relationship takes into account that a small amount of basal melting, as opposed to none, may affect the ice flow a lot, while even a large increase in basal melt water at locations where water already is present in large quantities may not be very important.

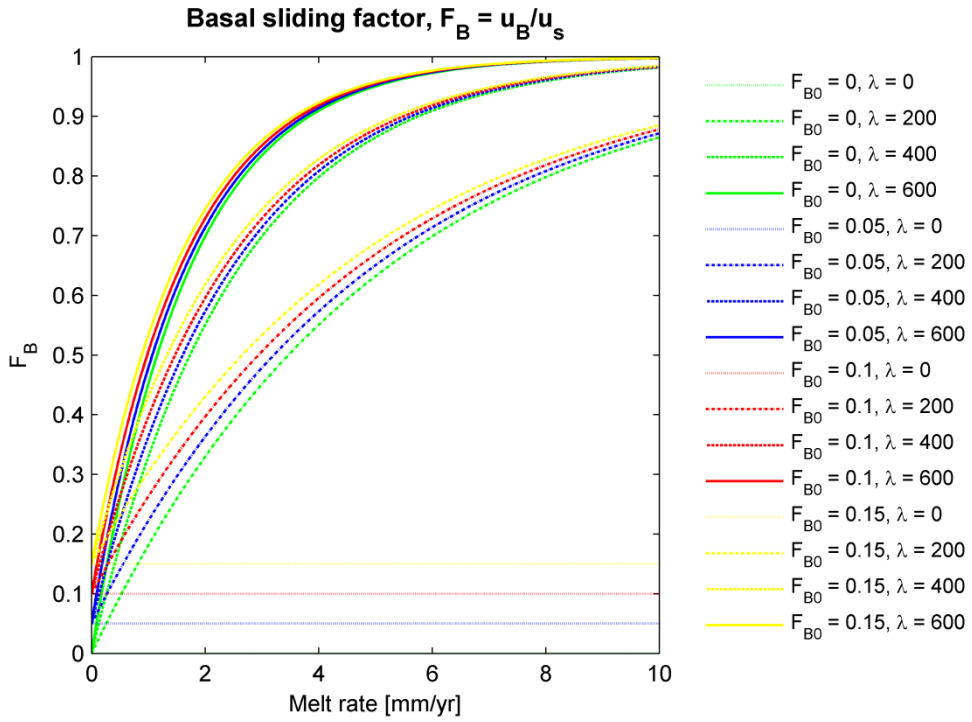

Figure 6.5: The effect of basal melt water on basal sliding as expressed by the parameterization in equation (6.15), when using different values for F_{B0} and λ.

The relationship in equation (6.15) assumes that melt water only affects the ice flow where it is formed. But if the water it not able to drain away into the ground, a thin layer of melt water or indeed melt water channels may evolve at the bedrock, possibly leading the water to locations, where no melting occurs. On the other hand, at locations with loose sediments, the melt water may drain away immediately after its formation, and hence at some places no basal melt water will be present despite of even heavy basal melting. Thus, to determine the amount of basal sliding, one ought to take into account the properties of the underground as well as the hydraulic system at the base of the ice sheet. These are issues that are very hard to deal with in a proper way.

Other factors than basal melt water also affect the amount of basal sliding. This applies e.g. for the roughness of the bed. The rougher the bed, the more difficult it is for the ice to slide. However, it is not yet known at which length-scales the roughness is important for the ice flow. We have therefore chosen to disregard such a relationship.

6.4.4. Kink height

In the Monte Carlo analysis, the kink height will be assumed to stay a constant percentage of the ice thickness along the flowline. This is a rough estimate. Many factors influence the kink height (basal melting, bedrock topography etc.), and may cause it to be very different from constant along the flowline. Yet, these relationships are difficult to quantify, and will therefore not be taken into account here.

6.4.5. Upstream variations

To track particles down the ice sheet which are to end up in the first part of the radio echogram, we need to start the particles upstream the considered flowline. In fact, due to the large surface velocities in the area, all the particles forming the lowest layer originate further inland than the beginning of the flowline.

Despite no information exists on the internal layering upstream the start of the radio echogram, the particles can still be tracked down the ice sheet here provided knowledge of how the flow parameters change in this area. Thus, the following assumptions are made: Upstream the image, the present accumulation rates and basal melt rates are equal to their value in the very first part of the image. The same goes for the ice thickness. And just as in the first part of the radio echogram where no surface velocity data are available, the amount of influx from the sides is assumed negligible.

Chapter 7

Internal layering in an ideal ice sheet

7.1. Effects of the flow parameters

We now wish to investigate the effect of the different flow parameters on the internal layering in an idealized ice sheet under the assumption of the flow pattern being completely described by the equations given in chapter 6. Furthermore, the resulting layering will be compared to the layering found by using a one-dimensional approximation. Steady state is assumed throughout the chapter.

7.1.1. Variations in accumulation rate

To see the effect on the internal layering of a changing accumulation rate along the flowline, the accumulation rate has been assumed to display a decreasing trend towards the margin, overlain by rather large sinusoidal oscillations. The resulting layering, when using respectively a one-dimensional and a two-dimensional approximation, is illustrated in figure 7.1.

In both cases, the variations in accumulation rate give rise to wobbling isochrones. The layers are nice and smooth with large oscillations in the one-dimensional model, and more chaotic with smaller variations in the two-dimensional model. The uppermost layers have a similar shape in the two approximations, but in the two-dimensional approximation the peaks and dips of the layering are situated further towards the margin due to the horizontal movement of the ice. The displacement increases with depth.

The deeper layers exhibit substantial differences when using the two approximations. In the one-dimensional model, the amplitude of the undulating layering increases downwards the upper half of the ice sheet. In the two-dimensional model, the particles forming the deeper layers have originated much further upstream. On the way to their present locations, they have experienced both large and small

accumulation rates, and they have all experienced approximately the same average accumulation rate. The further the particles get to travel, the more similar the average accumulation rate experienced by the different particles is. Hence, the layers gradually become more straight downwards the ice sheet.

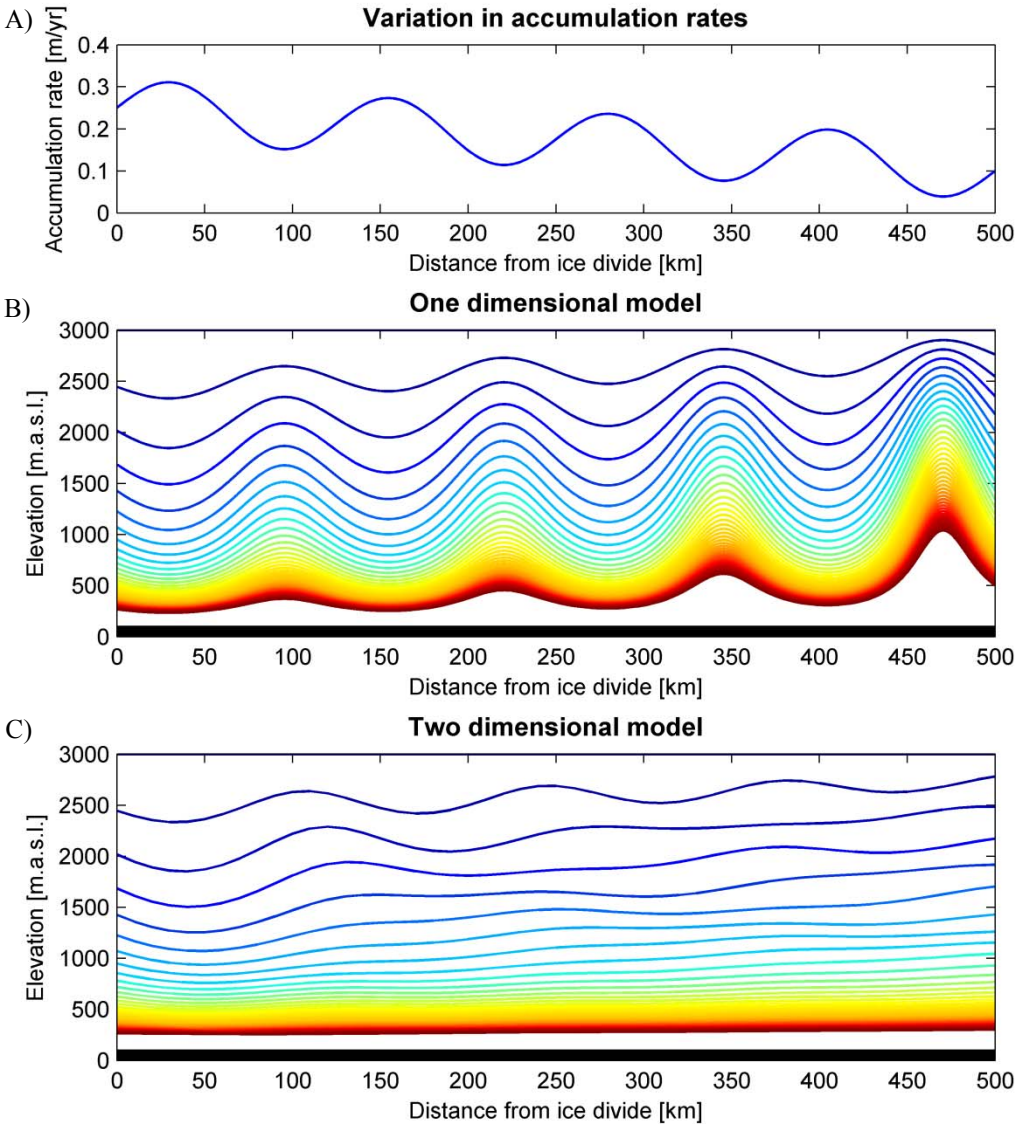

Figure 7.1: The resulting internal layering under the assumption of a varying accumulation rate along the flowline as shown in **A)**. **B)** A one-dimensional approximation and **C)** a two-dimensional approximation. Isochrones are drawn with a spacing of 2500 years back to 100 ka BP. No basal melting or sliding is allowed, and the fractional kink height is set equal to 0.3. The bed (shown in black) is horizontal, and the surface is constant at 3000 m.a.s.l.

In conclusion, the small-scale variations in accumulation rates mainly affect the position of the upper layers and the layering close to an ice divide, where the horizontal velocities are small. On the other hand, there is a slight upwards inclination of the deeper layers in the two-dimensional model due to the overall decrease in accumulation rates towards the margin. Accordingly, large-scale variations in accumulation rates persist to have an influence all the way down the ice sheet.

7.1.2. Basal melting and sliding

In figure 7.2 is shown the resulting layering when non-zero basal melt rates exist along some part of the flowline. The situation can be perceived as an encounter with a hotspot, where the geothermal heat flux is large, and a significant amount of basal melt water is produced. As the basal melt rates and basal sliding are intimately connected, two cases with different amounts of basal sliding due to the presence of the melt water will be considered. Firstly, we assume no basal sliding to occur (a rather unlikely scenario, but very instructive), and secondly basal melt water is assumed to have a large influence on the amount of basal sliding. The basal sliding factor, F_B, has been determined according to the "sliding law" in section 6.4.3, when using $\lambda = 100$ and assuming the amount of basal sliding when no water is present to be negligible ($F_{B0} = 0$). Note that due to the large basal melt rates at the hotspot, even a λ-value of 100, which is not exceptionally large, causes the basal sliding factor to approach unity. In this second case, we are thus dealing with almost full basal sliding in the area of the hotspot.

In general, basal melting drags down the internal layers, and the effect is most pronounced for the lower layers. From the layering obtained when using a one-dimensional model, it is also obvious that (in contrast to the other parameters) basal melting results in relatively thick annual layers at the base of the ice sheet.

In the one-dimensional case, the effect of basal melting on the internal layering is (of course) only visible in the area where melting actually occurs. The two-dimensional approximation allows basal melting to also be important for the layering downstream the hotspot, where no melting occurs. Compared to the one-dimensional approximation, the influence of basal melting in the two-dimensional approximation is less at any specific point, but in return it affects the layering over a much larger area. From figure 7.2 C it is seen that even in the very last part of the image, the lowest layers are still situated deeper than they were in the beginning of the image. This is a direct result of the existence of the hotspot 200 km further upstream.

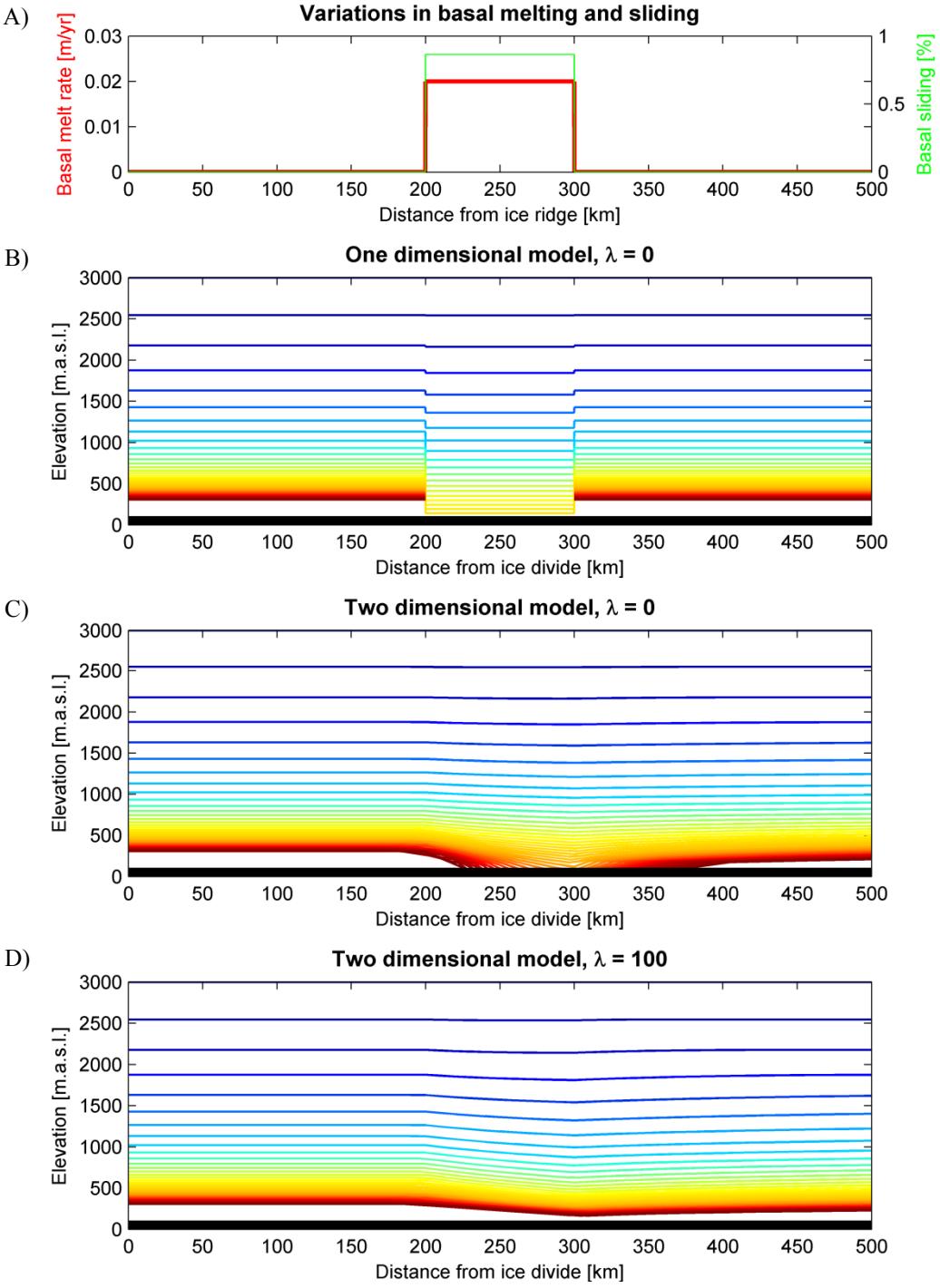

Figure 7.2: The resulting internal layering under the assumption of a varying basal melt rate along the flowline as shown in **A)**. The basal sliding factor has been determined according to the sliding law in section 6.4.3 by use of F_{B0}= 0 and a λ-value of 0 and 100 respectively. **B)** Both a 1D approximation and **C)**, **D)** a 2D approximation have been applied. Isochrones are drawn with a spacing of 2500 years back to 100 ka BP. The accumulation rate is a constant 0.2 m/yr along the flowline, and the fractional kink height is set equal to 0.3. Again, bed and surface are assumed horizontal.

When also taking basal sliding into account, the appearance of the layering changes significantly. At any spot, the lowest layers are now affected less by the basal melting while the upper layers are affected a bit more. This can be explained by the changes in the horizontal velocity profile due to the increased basal sliding. Below the kink height, the horizontal velocities become larger, which cause any particle traversing the location of the hotspot to experience the high downwards velocity during a shorter period of time. As the mass flux at any location must remain the same in both scenarios, the increased horizontal velocities below the kink height must in return cause the horizontal velocity above the kink height to decrease. As a result, the particles are here exposed during a longer period of time to a higher downwards velocity due to the hotspot, and they will reach a position deeper down in the ice sheet.

7.1.3. The kink height

We will now look into the influence of the kink height on the internal layering.

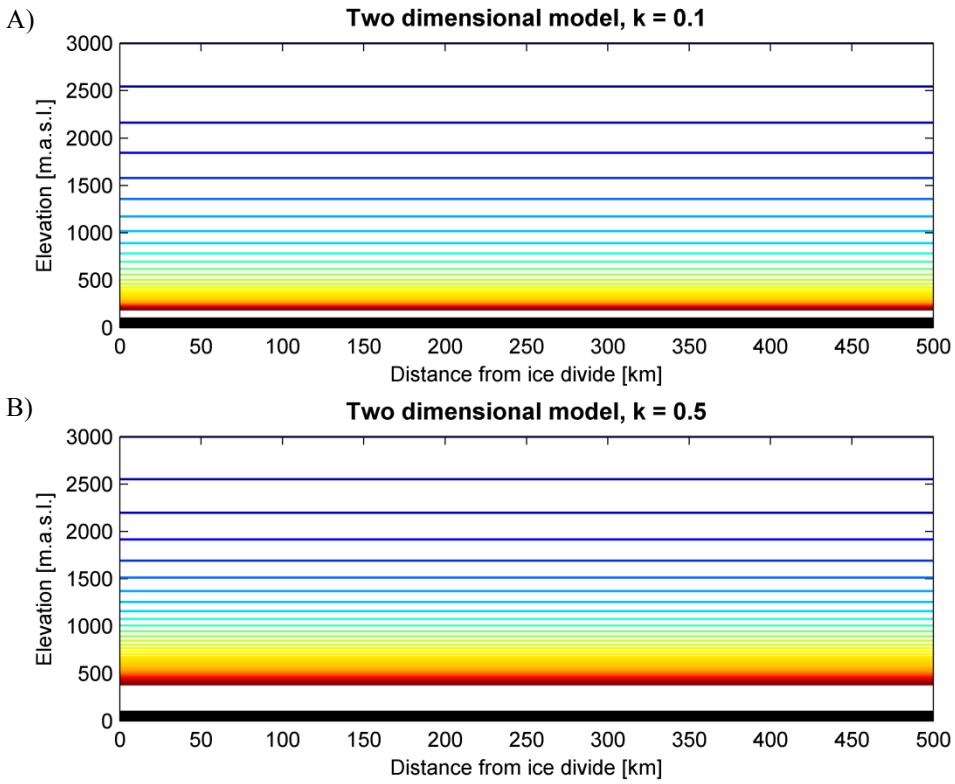

Figure 7.3: A) and **B)** The resulting layering when using two different fractional kink heights, namely $k = 0.1$ and $k = 0.5$, and otherwise assuming the rest of the parameters to be constant along the flowline. Bed and surface are horizontal. The accumulation rate is equal to 0.2 m/yr and no basal melting or sliding is allowed. Isochrones are drawn with a spacing of 2500 years back to 100 ka BP.

In figure 7.3 is shown the resulting layering when using a fractional kink height of respectively 10% (very low) and 50% (very high). From a comparison of the two plots, it is clear that changes in kink height mainly affect the position of the lower layers. As the mass flux at any spot once again must remain the same in the two scenarios, a high kink height results in larger horizontal velocities in the upper part of the ice sheet, and correspondingly lower vertical velocities. This leads to an increased compression of the layers downwards the ice sheet, with old layers being situated relatively high up in the ice sheet.

7.1.4. Importance of bedrock topography

Bedrock topography exerts a large influence on the internal layering in an ice sheet. It can e.g. from figure 4.5, p. 26 be seen how the shapes of the deep internal reflectors along the NEGIS conform to the bedrock topography. To gain a better understanding of its effect, we will now allow the bedrock to change along the flowline, and observe the resulting layering.

In reality, it is changes in ice thickness that are relevant for this kinematic model, not changes in bedrock topography. However, as the surface elevation changes far less abruptly than the bedrock topography, most of the resulting changes in ice thickness are indeed due to the bedrock topography. For these simple configurations, the surface elevation is assumed to be constant along the flowline, in which case the magnitude of the change in bedrock topography and ice thickness is precisely equal.

The effect of the bed topography on the internal layering is most obvious when considering the instructive example of a step in the bedrock profile. In figure 7.4 is plotted the resulting layering. In the one-dimensional approximation, the upper layers are almost unaffected by the step in the bedrock, while in the two-dimensional approximation even the uppermost layer is somewhat influenced by the bed. Deeper in the ice, the difference between the layering in the 1D and the 2D model increases, for yet again to decrease close to the bedrock.

To explain this feature of the two-dimensional model, let us consider the path of a particle, which has reached a certain depth before encountering the bedrock step (see figure 7.5 for an illustration). Until the particle reaches the step in the bedrock, its path can be calculated by means of a one-dimensional model, as everything else is held constant. In a pretended absence of the downwards velocity component due to accumulation, the particle would maintain a constant normalized vertical coordinate ζ when moving across the step in the bedrock profile where the ice is squeezed together. However, accumulation causes the particle to experience a downwards velocity component relative to the ζ-isolines. In other words, in the two-dimensional

approximation a particle experiences both an upwards velocity component due to the rising of the bed and – as always – a downwards component due to accumulation.

The one-dimensional model (being one-dimensional!) does not recognize that the bedrock at a given point is not plain flat. As the accumulation rates along the flowline are constant, the only factor causing a difference in the position of the layers is the larger thinning rates in areas where the ice thickness is small. As it can be seen from figure 7.4 A, the upper layers in the 1D approximation are at an almost constant depth all along the flowline despite the changes in bedrock topography. Hence, the effect of the different thinning rates along the flowline on the position of the upper layers is miniscule. This is also true in the two-dimensional approximation.

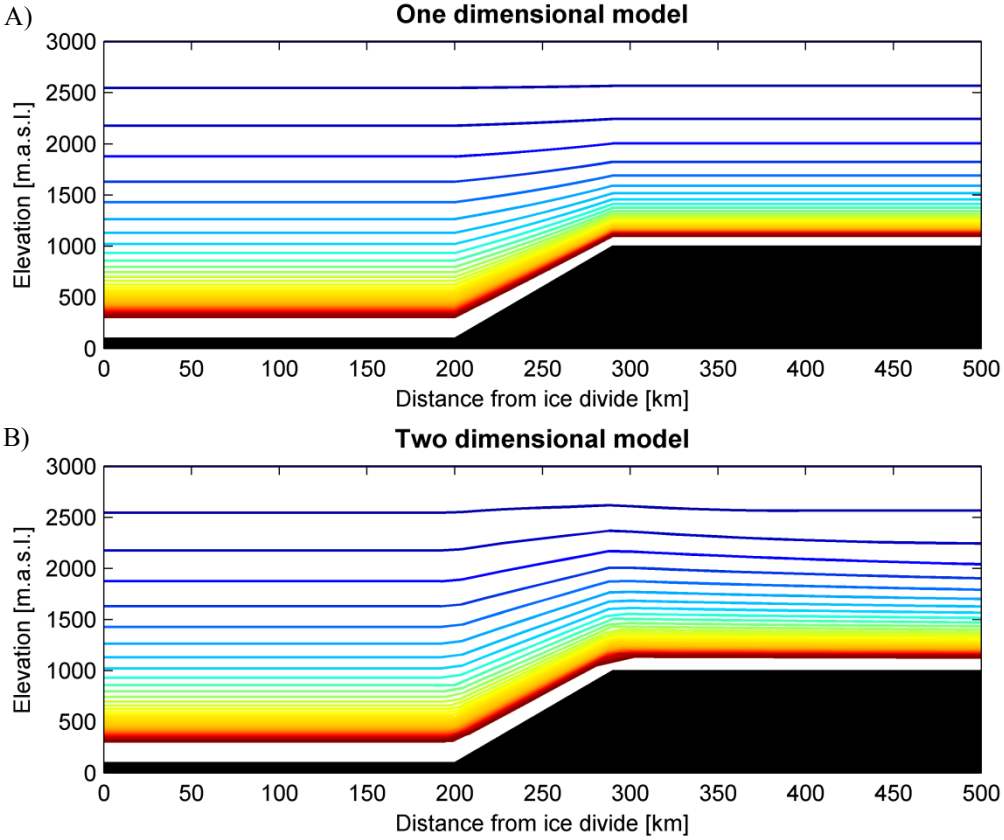

Figure 7.4: Internal layering in case of a step in the bedrock topography when **A)** using a one-dimensional model and **B)** using a two-dimensional model. The accumulation rate is constant along the flowline (0.2 m/yr) and no basal melting or sliding occurs. The kink height is equal to 0.3. Isochrones are drawn with a spacing of 2500 years back to 100 ka BP.

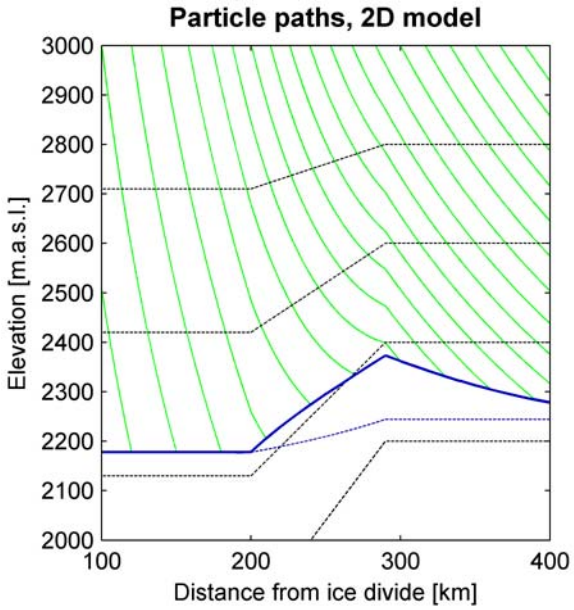

Figure 7.5: Particle paths leading to the 5000 year old isochrone in case of a step in the bedrock topography. Parameters as given in figure 7.4. For comparison, the resulting isochrone when using a 1D model is shown with a dashed blue line. Dashed black lines indicate isolines of constant ζ-values.

The effect of the bed topography on the shape of the isolines is also relatively small in the uppermost part of the ice sheet. Yet, it contributes much more significantly to the resulting position of the layers than does the different thinning rates along the flowline. As the shape of the isolines only is relevant for the two-dimensional model, the isochrones corresponding to this model are located higher up in the ice sheet than those in the one-dimensional case. Conversely, if the bed displays a descending step, only the particles in the two-dimensional approximation will feel this change in topography, and the resulting isochrones will be situated lower than the corresponding one-dimensional isochrones.

In the lower part of the ice sheet, the different thinning rates along the flowline due to bedrock topography start to play an important role. As the ice thickness generally is decreasing with distance from the ice divide, the thinning rates increase with distance from the ice divide. Thus, the average thinning rate encountered by a particle is smallest in the two-dimensional approximation. In other words, the particles forming the isochronous layers in the two-dimensional case have not been compressed as much as those forming the layers in the one-dimensional case. Consequently, the effect of the different thinning rates along the image is opposite of that of the shape of the isolines, and the two are competing with each other. Their combined effect is to make the resulting layering in the two approximations more and more alike with depth.

In conclusion, the isochrones found by use of a two-dimensional model are much more influenced by the bedrock topography than those found by use of a one-dimensional model. Even the uppermost layers are affected by the bedrock. This is

also the case in reality, where bedrock topography seems to inflict meter-sized undulations of layers in a depth of only 200 m (*T. Overly, pers. comm.*). It is therefore not surprising that we in section 5.2 had difficulties calculating the true accumulation rates along the NEGIS by use of a one-dimensional model. Indeed, the calculated accumulation rates were to a high degree reminiscent of the bed topography. But so it should also be. The undulations of the uppermost layers are not due to variations in the accumulation rate (as they are inherently taken to be when using a one-dimensional model), but are instead the result of a changing bedrock topography, which is a factor not taken into account in a one-dimensional model.

Let us now proceed to a slightly more realistic scenario. In figure 7.6 is shown the resulting layering due to sinusoidal undulations of the bedrock topography, while assuming the basal melt rates to increase linearly along the flowline.

Similarly to the previous case, the layering found by a two-dimensional approach is the one most heavily influenced by the basal topography. Moving along the flowline, the basal melt rates are increased, and the layering gradually transforms: In areas with large melt rates, the layering follows the bedrock topography less closely. The effect is most obvious when using a one-dimensional approximation, but it is also the case for the two-dimensional approximation. Using radar images, it is thus possible to make a qualified guess for the location of areas with high basal melt rates by comparing the shape of the radio-echo layers with the bedrock topography.

The undulations of the upper layers due to the bedrock topography increase with distance from the ice ridge. This behaviour has nothing to do with the increasing melt rates (which have almost no effect this high up in the ice sheet), but is due to the increased horizontal velocities along the flowline. Close to the ice divide, the horizontal velocity is small. Here, one-dimensional flow is a good approximation, and the upper layers are just as straight as found when using the one-dimensional model. On the other hand, the large horizontal velocities in the last part of the image cause the particles to have travelled a long way before reaching their present positions, and they are affected by the changing bed topography on their way.

Another difference between the layering in the one- and two-dimensional cases is the presence of slightly older layers in the two-dimensional approximation. This is due to the fact that the basal melt rates are assumed to increase with distance. Compared to the one-dimensional approximation, this relationship causes the particles in the two-dimensional case to have experienced a smaller average basal melt rate on the way to their present locations.

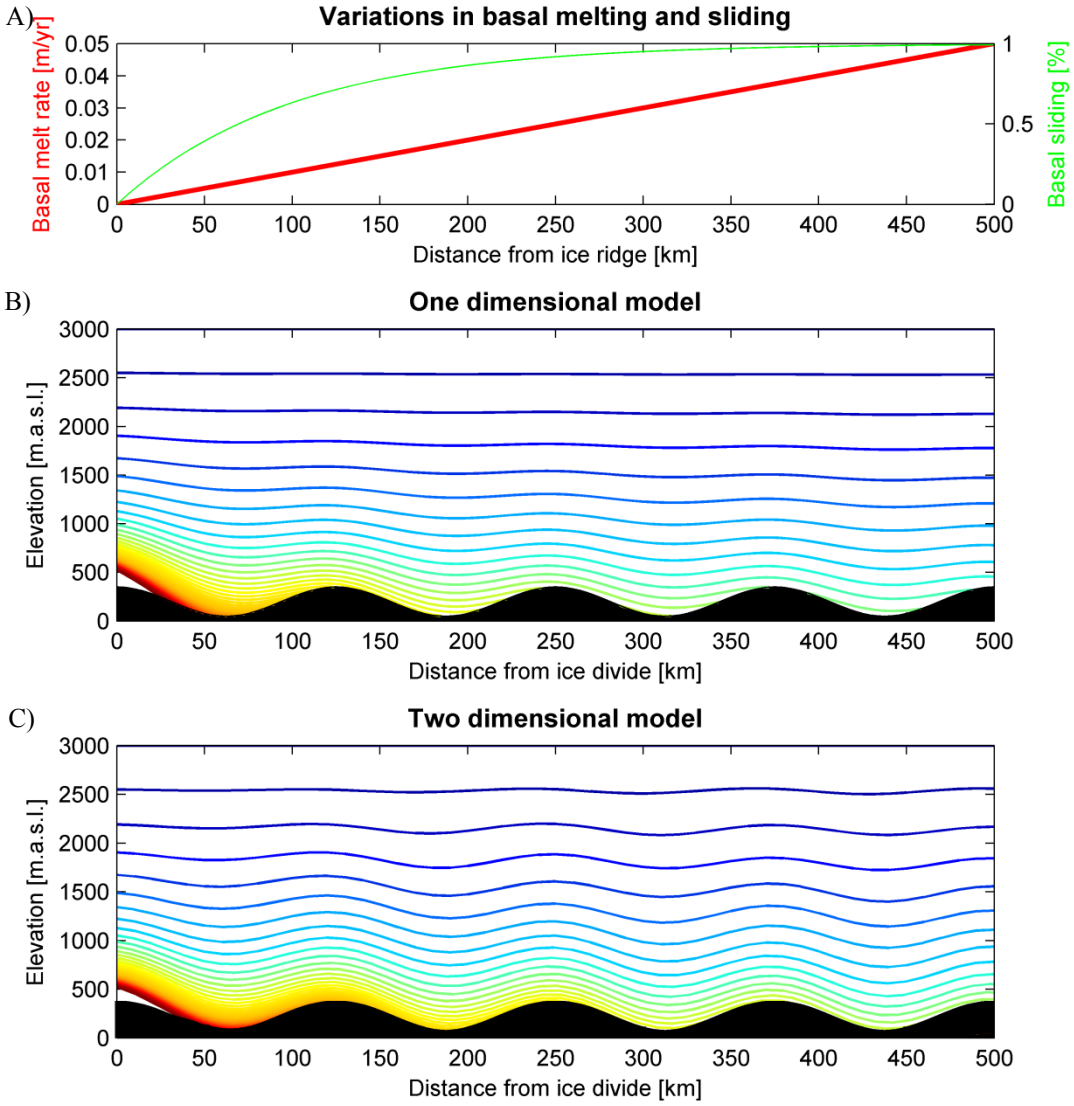

Figure 7.6: The resulting layering when dealing with an undulating bed and linearly increasing basal melt rates when using **B)** a 1D approximation and **C)** a 2D approximation. The basal melt rates and the resulting basal sliding are portrayed in **A)**. For the sliding is employed $F_{B0} = 0$ and $\lambda = 100$. The accumulation rate is a constant 0.2 m/yr and the fractional kink height is equal to 0.3.

7.1.5. Impact of 3D-effects

Finally, we will consider the effect of convergent flow on the layering. In figure 7.7D a constant influx of material along a confined part of the flowline is assumed. The amount of influx here (corresponding to $\partial v_s/\partial y = 10^{-3}$ yr^{-1}) is significantly less than at some places along the flowline along the NEGIS, but due to its stability over a large area, it has an important impact on the resulting layering.

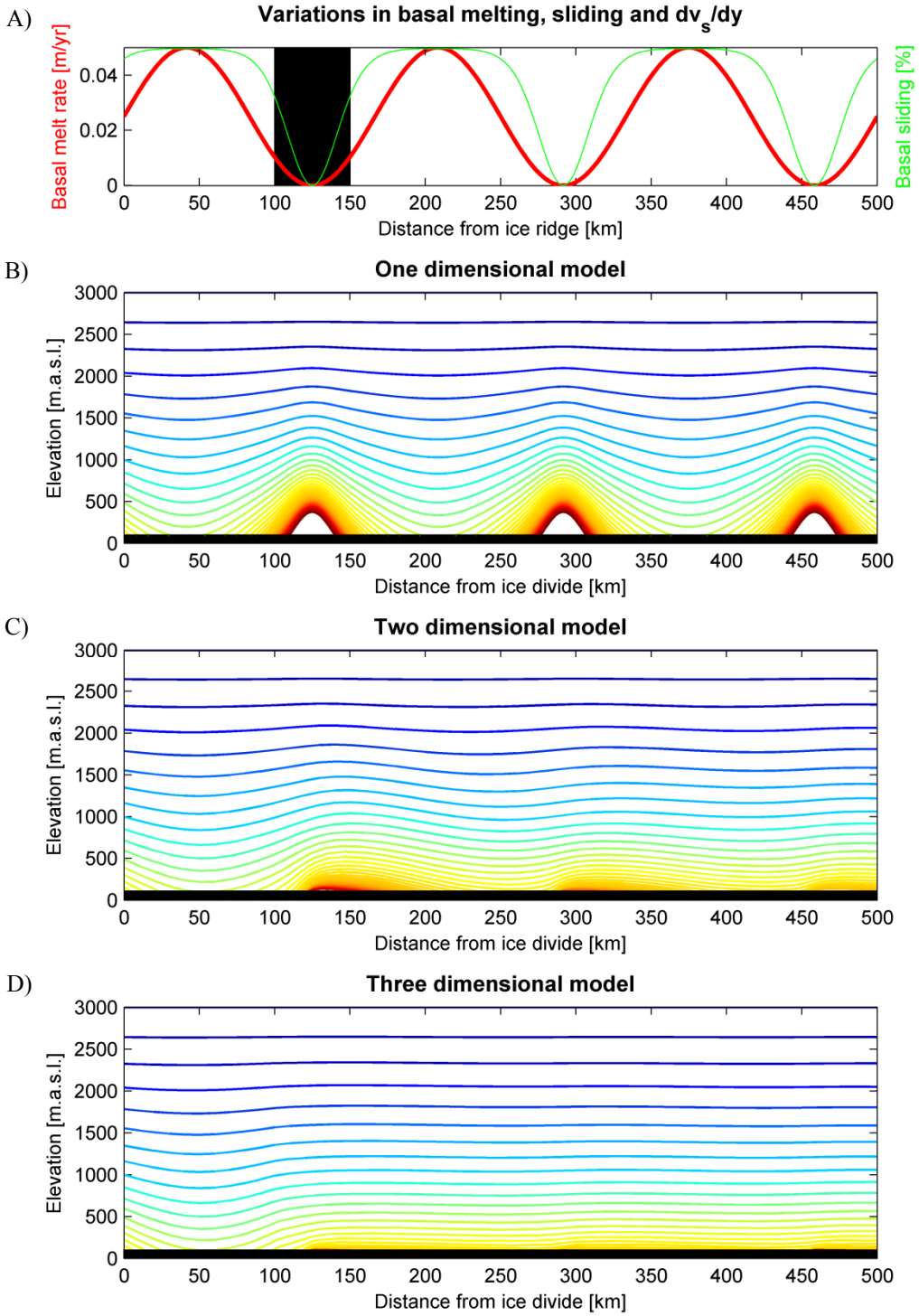

Figure 7.7: The resulting layering when using **B)** a 1D approximation, **C)** a 2D approximation, and **D)** a 3D approximation. The variation of basal melt rates and basal sliding along the flowline is shown in **A)**. For the sliding is employed $F_{B0} = 0$ and $\lambda = 100$. The area in black signifies an area with an influx of material corresponding to a value of $\partial v_s / \partial y$ equal to 10^{-3}. The accumulation rate is equal to 0.15 m/yr and the fractional kink height is 0.3. Bed and surface of the ice sheet are horizontal.

If all other parameters were constant along the flowline, even an enormous supply of material would have no influence on the internal layering. The main result of such a supply is to increase the horizontal velocities, which in case of no lateral variations whatsoever has no effect on the resulting layering. We thus chose to let the basal melt rates vary sinusoidally along the flowline.

From the one-dimensional approximation in figure 7.7 A, the influence of basal melting on the position of the internal layers is observed once again. In areas with high rates of basal melting and sliding, the layers are situated deeper, and the effect increases with depth. To some extent, the same applies for the two-dimensional model. However, the effect of the increasing surface velocities along the flowline is obvious. In the beginning of the flowline where the surface velocities are small, the resemblance between the 1D and the 2D model is significant. But due to the larger horizontal velocities downstream, the particles are subjected to the large basal melt rates during a shorter period of time. Hence, basal melting causes the layers to be dragged less down than in the one-dimensional approximation. Instead, it affects the layering over a much larger area. The effect gets more and more pronounced downstream, as the surface velocities are increasing along the flowline.

When also taking into consideration the extra influx of material in the small area in the beginning of the flowline, the resulting layering is yet again significantly altered (figure 7.7 D). Before the influx of material, the layering is of course exactly the same as derived by use of the two-dimensional model. But hereafter, the extra supply of material gives rise to increased horizontal velocities. The particles have almost no time to feel the changing melt rates along the flowline, but feel a basal meltrate corresponding to the average one, and the layers become almost straight lines.

Chapter 8

Using an inverse approach

8.1. An inverse problem

A typical physical problem consists of a physical theory and some recorded input values, from which it is possible to predict the values of some unobserved quantities that are the solution to the problem. This corresponds to solving a forward problem. In this context, the forward problem would be to calculate the position of the internal layers in the ice, when given the proper accumulation rates, basal melt rates etc. for the area. However, in many cases – like this one – we do not know the precise value of the parameters used in the physical model, but instead we know the outcome of the model (i.e. the internal layering). We want to use this knowledge to ameliorate our information on the value of the parameters. In this case, we are dealing with an inverse problem.

As opposed to a forward problem, an inverse problem generally does not have a unique solution. Instead, its solution is a probability distribution describing which values of the parameters are best at predicting the observed data.

8.1.1. Model space and data space

To solve an inverse problem, a physical theory must be known, which allows us to solve the forward problem. Also a parameterization that provides a "complete" description of the system must be chosen. Such a complete description of the system will in the following be termed a model.

Given such a parameterized system, we can introduce the notion of a multi-dimensional space called the model space, M, which is formed by the span of the different model parameters. Each point in the model space, in the following denoted $\boldsymbol{m}$, corresponds to a specific choice of parameters and is thus a conceivable model of the system.

In our flow model, the parameters are accumulation rates and basal melt rates in discrete points along the flowline, parameterized time dependence of the accumulation rates, parameterized basal sliding, surface velocity in the beginning of the flowline and kink height. Also the ages of the isochrones that are only known to a certain accuracy, are parameters. In total, we have 43 parameters, and hence our model space is 43 dimensional.

Another multi-dimensional space, *D*, the data space, can equivalently be defined as being the space of all possible data responses. Each observable quantity represents a dimension of the data space, and an observed data set is represented by a point $\boldsymbol{d}$ in the data space. In our case, $\boldsymbol{d}$ represents discrete data points (90 along each of the ten layers, i.e. 900 in total) describing the position of the internal layers in the ice sheet.

For all practical purposes, both *M* and *D* can here be considered linear spaces, which simplifies the following analysis. In reality, they are not true linear spaces, but they are approximately so in the small region of the data and model space we are dealing with. (See e.g. *Steen-Larsen, 2007* or *Mosegaard and Tarantola, 2002*, for a thorough treatment of metrics in non-linear spaces, and the consequences for the different probability densities hereof).

With these notations, the forward problem (i.e. to predict the corresponding theoretical outcome when given the model parameters) can be expressed as performing a mapping from *M* to *D*:

$$\boldsymbol{d} = \boldsymbol{g}(\boldsymbol{m})$$

Here, $\boldsymbol{g}$ is our mathematic model of the physical system under study, which relates the model parameters with the corresponding observed dataset. But in general, the theoretical outcome computed by the forward model does not reproduce the observed data set perfectly. This is partly due to imperfections in the mathematical model, and partly due to observational uncertainties.

Conversely, the inverse problem can be expressed as:

$$\boldsymbol{m} = \boldsymbol{g}^{-1}(\boldsymbol{d})$$

However, in most cases $\boldsymbol{g}$ is not invertible, and its inverse $\boldsymbol{g}^{-1}$ cannot be constructed. This is certainly the case here, where the operator $\boldsymbol{g}$ is given by a numerical algorithm.

8.1.2. Probability distribution of the observed data

Our measured data set may be perceived as constituting a single point in the data space, $\boldsymbol{d_{obs}}$. But the uncertainties connected with the measurement of every physical entity may cause the true value to be slightly different. Hence, the result of the measurement is better described by a probability density $\rho_D(\boldsymbol{d})$ defined over the data space *D*.

As *D* is linear, the uncertainties corresponding to the individual data points along the different layers in the ice sheet can be ascribed a normal distribution (*Tarantola, 2005, p. 57*). The resulting Gaussian probability density centred at $\boldsymbol{d_{obs}}$ is given by (*Tarantola, 2005, p. 25*):

$$\rho_D(\boldsymbol{d}) = k \cdot \exp\left(-\frac{1}{2}(\boldsymbol{d} - \boldsymbol{d_{obs}})^t C_D^{-1}(\boldsymbol{d} - \boldsymbol{d_{obs}})\right) \tag{8.1}$$

Here, k is a normalization constant (such that the probability density over the whole data space integrates to 1), and C_D is the covariance matrix of the data points. The off-diagonal entries in the covariance matrix describe how different data points tend to vary together, while the entries on the diagonal describe the variances, σ^2, of the data points. As the different data points along any particular layer will be chosen far enough away from each other for their uncertainties to be assumed independent, the off-diagonal elements in C_D are all equal to zero.

8.1.3. A priori information on the model parameters

Independent of the observed data, some knowledge of the values of the different model parameters usually exists prior to starting to solve the inverse problem. Such knowledge is called a priori information. The probability distribution in the model space corresponding to this information is denoted $\rho_M(\boldsymbol{m})$.

Some of our model parameters will be assumed bounded by two values $m_{min,i}$ and $m_{max,i}$. When dealing with a linear model space, the a priori probability distribution for these parameters is constant within a certain interval and zero otherwise:

$$\rho_i(m_i) = \begin{cases} k_i, & m_{min,i} \leq m_i \leq m_{max,i} \\ 0\,, & otherwise \end{cases}$$

This is the case for the basal melt rates, the fractional kink height, the surface velocity in the beginning of the flowline, and the parameters corresponding to basal sliding and past accumulation rates.

For the present accumulation rates and the ages of the different layers, a preconception of their values exists beforehand. The uncertainty of these is assumed to be described by a normal distribution with a corresponding variance, σ_i^2, as given in section 4.1.7 and 6.4.1. For these parameters, the a priori probability density is given by:

$$\rho_i(m_i) = k_i \exp\left(-\frac{1}{2}\frac{\left(m_i - m_{prior,i}\right)^2}{\sigma_i^2}\right)$$

Due to the linearity of the model space, the complete a priori probability density in the model space is then given as the product of the individual prior probability distributions for the different model parameters:

$$\rho_M(\boldsymbol{m}) = \prod_i \rho_i(m_i)$$

8.1.4. The general solution to an inverse problem

The solution to an inverse problem is a so-called a posteriori probability distribution over the model space, which can be perceived as a collection of models that all fit the observed data sufficiently well. Although such a posterior probability distribution may be very complex, it is uniquely defined, and it contains information on mean values, maximum likelihood values etc. of the different model parameters.

The general solution to an inverse problem can be obtained from the a priori knowledge on the model parameters and the probability distribution of the observed data (*Tarantola, 2005, p. 34*):

$$\sigma_M(\boldsymbol{m}) = k\rho_M(\boldsymbol{m})L(\boldsymbol{m}) \tag{8.2}$$

Again, k is a normalisation constant, and $L(\boldsymbol{m})$ is called the likelihood function, which is a measure of how well a model is able to explain the observed data, when given their inherent uncertainties. This solution is illustrated in figure 8.1. Under the assumption of a linear data space and a perfect theory (i.e. negligible modelling uncertainties), the likelihood function for a specified model $\boldsymbol{m}$ is given by:

$$L(\boldsymbol{m}) = \rho_D\big(\boldsymbol{g}(\boldsymbol{m})\big)$$

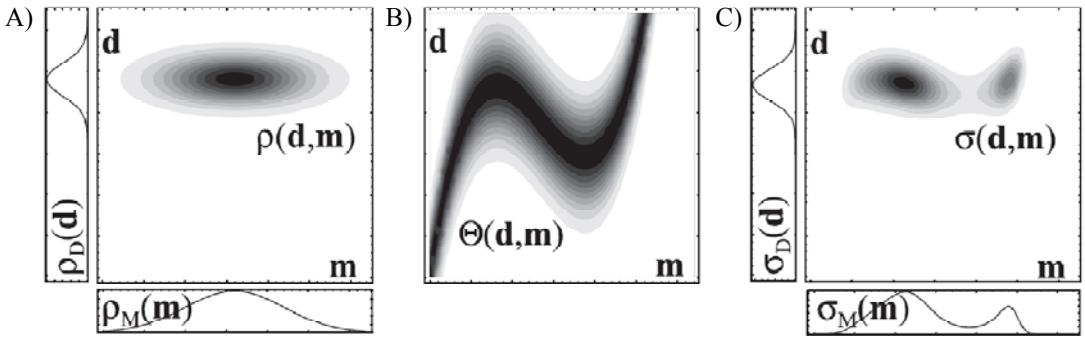

Figure 8.1: A) The probability densities ρ_D and ρ_M represent our information on the observable parameters and our a priori information on the model parameters, i.e. information that is available before the start of the inverse analysis. As the a priori information on the data and model parameters per definition is independent, we may consider the joint probability density $\rho(\boldsymbol{d},\boldsymbol{m}) = \rho_D(\boldsymbol{d})\rho_M(\boldsymbol{m})$. It is shown in grey. **B)** The physical operator $\boldsymbol{g}$ performs a mapping from the model space to the data space in a possibly non-linear way. Here, the perfect physical theory represented by $\boldsymbol{g}$ has been replaced by a non-exact theory $\Theta(\boldsymbol{d},\boldsymbol{m})$. **C)** The resulting joint posterior probability, $\sigma(\boldsymbol{d},\boldsymbol{m})$, found by combining the information in A and B. Also shown are the marginal a posteriori probability distributions for the data and model parameters, σ_D and σ_M. By comparison to the prior probability densities, we see the information gained on the model parameters. Figure from *Tarantola, 2005*.

Given our expression for ρ_D for the present inverse problem (equation (8.1)), and using our knowledge of C_D being a diagonal matrix, the likelihood function can be written as:

$$L(\boldsymbol{m}) = k\exp\big(-S(\boldsymbol{m})\big) \tag{8.3}$$

Here, the misfit function, $S(\boldsymbol{m})$, is given by the squared sum of the discrepancy between the calculated value and the observed value of each of the N data points, compared to the standard deviation of that specific data point:

$$S(\boldsymbol{m}) = \frac{1}{2}\sum_{i=1}^{N}\frac{\left(d_{calc,i} - d_{obs,i}\right)^2}{\sigma_i^2} \tag{8.4}$$

From the above equations (8.2), (8.3) and (8.4), the posterior probability for any given set of parameters can be calculated.

8.2. Using a Monte Carlo approach

Given equation (8.2), the posterior probability density for the problem at hand can in principle be found simply by calculating the value of $\sigma_M(\boldsymbol{m})$ for every possible model. However, this is a monstrous task when dealing with high-dimensional spaces. Thus, it often pays off to use a random rather than systematic exploration of the model space.

Named after the famous casino in Monaco, Monte Carlo simulations are based on stochastic processes by the use of random numbers. In Monte Carlo simulations only a small number of possible combinations of the different model parameters are investigated. But as these combinations are chosen randomly or pseudo-randomly, they can be used to describe the system as a whole, and we are thus able to infer the solution to the inverse problem. In this way, it becomes possible to investigate physical systems with high complexity. It also allows us to find a solution, which not only provides the best fitting parameters, but also gives an estimate of the uncertainties with which these have been found.

Monte Carlo methods are highly demanding on computer power, and although the ideas behind the Monte Carlo method are old, only recently the advances in computer technology have made the method really efficient. Today, Monte Carlo based investigations are widely applied in many areas.

8.2.1. The Metropolis sampler

In order to explore the high-dimensional model space for the best solutions to the inverse problem, a pseudo-random walk in the model space is used. A random walk is a kind of Brownian motion – a trajectory formed by taking successive steps in random directions. If unmodified, the random walk would sample a representation of the initial probability distribution of the model parameters. However, to put it with the words of Albert Tarantola: *"There is one problem with large-dimensional spaces that is easy to underestimate: They tend to be terribly empty"*. If unmodified, such a random walk would spend an enormous amount of time sampling the extensive low-probability areas. Fortunately, several ways to modify such a random walk exist. Here, we will apply the Metropolis algorithm.

The Metropolis algorithm is an importance-sampling algorithm. It means that when using this algorithm, the sampled density of models is proportional to the a posteriori probability distribution of the model parameters (*Mosegaard and Tarantola, 2002*). In other words, the algorithm makes sure that we sample most carefully in areas where the a posteriori probability is high, and hence it drastically decreases the

necessary computational power. At the same time, the Metropolis algorithm directly provides us with large collection of models representative of the posterior probability density.

Using the Metropolis algorithm, the steps taken can be either accepted or rejected, depending on how well the corresponding models fit to the data. In this way, the random walk ends up sampling models corresponding to their resemblance to the observed data. Given a current model $\boldsymbol{m}$, the model is perturbed by taking a step in the model space. This is done in such a way that if all steps were accepted, we would sample the a priori distribution of the parameters. We must now decide whether the random walker should stay at $\boldsymbol{m}$ or move to the new test model, $\boldsymbol{m_{test}}$. The probabilistic rule to judge whether any such step should be accepted or rejected is given by (*Mosegaard and Sambridge, 2002*):

$$P_{accept} = \begin{cases} \dfrac{\sigma_M(\boldsymbol{m_{test}})}{\sigma_M(\boldsymbol{m})}, & \sigma_M(\boldsymbol{m_{test}}) < \sigma_M(\boldsymbol{m}) \\ 1 \quad , & \sigma_M(\boldsymbol{m_{test}}) \geq \sigma_M(\boldsymbol{m}) \end{cases}$$

An outline of the resulting random walk is shown in figure 8.2. It can be shown that such a modified random walk samples the a posteriori probability density in the model space (*Mosegaard and Tarantola, 1995*). Note that the above acceptance criterion makes sure that there is no need for us to know the value of the normalization constant in equation (8.2).

If the proposed new model explains the observed data better or equally good as the current model, i.e. if it has a higher posterior probability, the step is always accepted. However, even if $\boldsymbol{m_{test}}$ has a lower posterior probability than the present model, the sampler may still choose to take the step. But the chance of taking it depends on how much lower the probability is. Only if the test model is just slightly worse at describing the observed data than is the current model, there is a good chance of accepting it. Due to the possible acceptance of such a step in the "wrong direction", the random walker is able to perform a global search in the model space, which is very important when dealing with non-linear problems that may have highly complicated posterior probability densities.

8.2.2. Convergence issues

Despite the apparent simplicity of the Metropolis sampler, the practical application of the rule involves the assessment of some non-trivial matters.

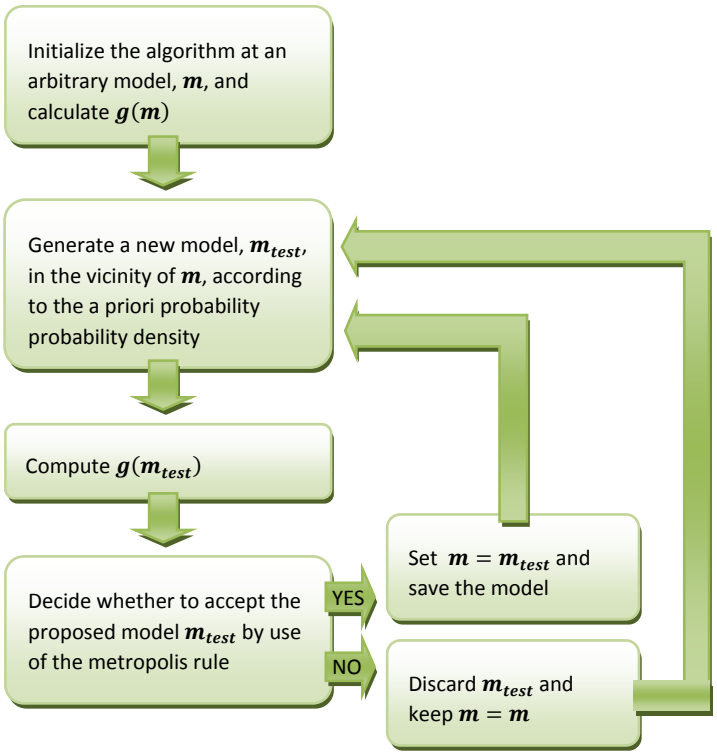

Figure 8.2: A schematic outline of the Metropolis algorithm.

Firstly, how do we decide what kind of "steps" the random walker is allowed to take in the model space? For it to be an efficient algorithm, the steps must be such that when jumping from one sample to the next, the perturbation of the predicted data is small. Otherwise, the random walker might in such a step leave the interesting area with the high posterior probabilities, and none of the steps would be accepted. On the other hand, we want the random walker to move as fast as possible around the interesting areas of the model space in order to get to explore them all.

In the present analysis, we let the random walker select a random direction, and then a step of random length (up to a certain maximum) in that direction. The maximum step length for the different parameters must be chosen carefully. In general, the best size of the perturbations is when the acceptance rate of the proposed steps is 30-50% (*Tarantola, 2005, p. 53*). We have then reached a balance between the necessity of moving rapidly in the model space and need of the Metropolis criterion to find some of the proposed steps acceptable.

Another critical issue is to decide when the random walker has visited enough different models in the model space for the posterior probability density to be sufficiently sampled. An approach, which to some extent can rule out the possibility of some overlooked regions of high posterior probability, is to restart the Metropolis

algorithm at different randomly selected points in the model space. But only a full exploration of model space would prove whether or not such a region exists.

8.2.3. Dependency issues

By nature of a random walk, two successive samples are highly dependent. But independent samples are needed to obtain reliable information on the posterior probability density in the model space. These are achieved by discarding most of the models produced by the Metropolis algorithm. By waiting a sufficient number of steps in between the acquirement of a new sample of the posterior probability distribution, the random walker has no memory of the previous sample, and two subsequent samples are independent.

The number of steps to wait between taking the samples to ensure their mutual independence depends on the problem. Among other things, it depends on the number of parameters, the degree of non-linearity of the forward algorithm, and the applied step sizes. In our flow model, we have 43 parameters. From a statistical analysis on the resulting pseudo-random walk, it was estimated that approximately every 500th step was independent. Hence, this is the value used for the waiting time in the present thesis.

We also need the samples to be independent of the starting model. When initialising the model at a random point in the model space, we most likely do not happen to choose a model with a very high posterior probability. The time before the random walker reaches a stable misfit and hence a high posterior probability is called the burn-in period. The low probabilities of the models during the burn-in period cause them to be uninteresting for the solution to the inverse problem, and they should not be sampled. For the Monte Carlo inversion of the flow pattern along the NEGIS, the burn-in period was identified to be around 25,000 steps, and the samples taken within this period were omitted from the analysis.

8.3. Implementation of the Monte Carlo search

As previously mentioned, we have chosen to use 90 data points along each layer. The remaining part of the data set, which makes up the rest of the internal layering, is discarded. This amount of data points is a balance between the data points to describe the overall structure of the layering, while not being too close, such that their mutual covariance can be disregarded in equation (8.1).

To compare these data points with those resulting from forward modelling, the particles must end their journey through the ice at the same x-values as the data points. The difference between the two can then be determined as the difference in the vertical direction. How to make the particles end here is not trivial, as it implies that the initial positions of the different particles on the ice sheet surface must be known before our forward algorithm can track them down the ice. Above the kink height, the matter is relatively easy, as the horizontal movement of the particles in this part of the ice sheet is independent of depth. For the particles ending below the kink height, this is not the case. Here, the result from the last accepted model is used to find an approximate starting point for the particles in the new model.

Due to uncertainties in the tracking routine, as well as the use of only approximate starting points, the particles do not end up precisely at the same x-values as the data points. We therefore interpolate between the different particles to give the best measure of the vertical position of the layer at this place. Interpolation is allowed as the modelled layers are relatively smooth, and as it only is a question of very little interpolation, given that successive models are very similar.

To proceed in this manner turned out to be of uttermost importance due to the wobbling of the observed layers and the high surface velocities in the area. If the same data points were not used every time, the horizontal displacement of the particles from model to model was so large that the resulting misfit between the modelled and observed layering mainly was a question of where explicitly the particle ended up in the x-direction. Only if it ended up close to where a wiggle of the observed layer accidentally crossed the modelled layer, was the model observed to provide a good fit. The importance of using fixed data points must therefore not be overlooked.

Using fixed data points gives us certain advantages. We inherently have that no layer is overemphasized in the fitting process relative to the rest, as well as no part of any layer is overemphasized. Another advantage of the method is that in areas, where the internal layers are not identifiable, we simply choose not to place any data points. In this way, the problem of assigning a misfit to these areas is irrelevant.

Chapter 9

Results of the Monte Carlo simulation

9.1. Values of the flow parameters

Using the Monte Carlo search, a collection of models that all fit the observed layering to a certain level has been generated. This ensemble of models represents the a posteriori probability distribution in the model space, and some characteristics of this distribution will now be presented.

The focus will be on the posterior marginal probability distributions of each of the different parameters in the flow model. The marginal probability distribution of a parameter is the integral of the probability distribution over the remaining dimensions of model space. In other words, while ignoring any information about the rest of the parameters, the marginal probability distributions reveal which value(s) are the most likely for a given parameter. The marginal probability distributions are constructed as histograms based on the collection of samples found by the Monte Carlo search. From the histograms, the mean value and standard deviation of the parameters can be calculated. It should be mentioned that the uncertainty estimate given by the calculated standard deviation only reflect the precision with which the Monte Carlo inversion is able to determine the value of the parameter. It does not include uncertainties arising from deficiencies of the applied model.

The Monte Carlo simulation was allowed to take 100,000 steps. In order to ensure the independence of two subsequent samples, we had to discard most of them, only taking a sample each 500th step after reaching the burn-in period (section 8.2.3). We hence ended up with a collection of merely 200 samples. A more extensive sampling might possibly give a significant improvement of the results, but we had to stop the Monte Carlo search at this point due to lack of time. Nevertheless, the result provides information on the values and variation of the flow parameters along the ice stream.

9.1.1. Accumulation rates along the flowline

In figure 9.1 is shown the posterior density distribution of the accumulation rates along the flowline. The colouring represents the density of sampled models, red corresponding to areas with a high density and blue corresponding to areas with a lower density of models.

The accumulation rates determined by the Monte Carlo simulation are rather bouncy, varying between 10 and 20 cm/yr. The jagged profile suggests that a too high accumulation at one of the six locations where the accumulation rate is determined, is being counteracted by a too small accumulation at the following spot, and vice versa.

This connection is also obvious when considering the correlation matrix between the different accumulation rates (figure 9.2). Red colours denote a strong positive correlation, while blue colours denote a strong negative correlation. Yellow, green and cyan hues denote weak correlations. As anticipated, two adjacent accumulation rates are strongly negatively correlated. This, being the case for all the accumulation rates, gives rise to the streaked appearance of the correlation matrix: All even accumulation rates are positively correlated, while being negatively correlated to the rest.

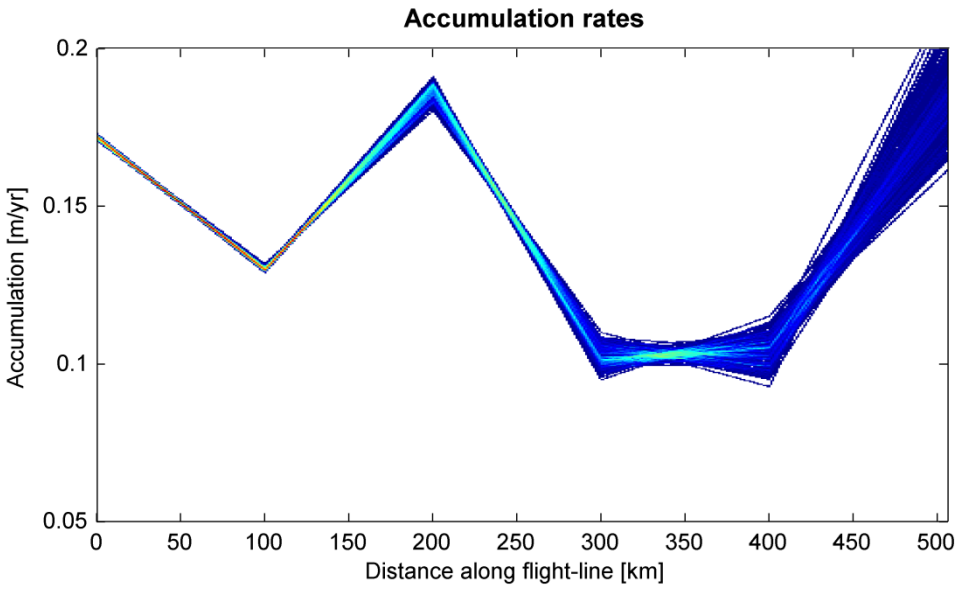

Figure 9.1: Density distribution of the accumulation rates along the flowline as found by the Monte Carlo search. Red denotes areas with a high concentration of sampled models, while blue areas have a lower concentration of models.

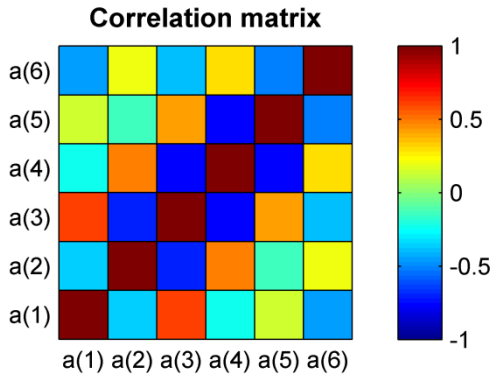

Figure 9.2: Correlation matrix for the six accumulation rates along the flowline.

Such a relationship could maybe have been avoided, had it been incorporated in our a priori information on the accumulation rates that they were to change smoothly along the profile (see e.g. *Steen-Larsen, 2007*). Another possibility is to force the Monte Carlo simulation with a priori information on the accumulation rates with smaller uncertainties. For instance, data from the accumulation map shown in figure 5.5, p. 41 could be included. It could also simply be by assuming smaller uncertainties of the accumulation rates obtained by the one-dimensional model.

The Monte Carlo simulation is best at determining the accumulation rates in the beginning of the flowline, see figure 9.1. This is expected due to the large increase in velocity towards the margin of the ice sheet, which causes the particles to be located in the beginning of the flowline during a much longer time period than in the last part of the flowline. The particles are therefore most affected by the accumulation rates in the first part of the flowline, and their resulting positions down the ice sheet are most dependent on these.

In figure 9.3 is shown a comparison between the mean accumulation rates along the North East Greenland Ice Stream as found by the Monte Carlo search, and by use of the one-dimensional model described in section 5.2. For two out of the six data points (namely at 200 and 500 km from the beginning of the flowline), the difference is substantial. The rest of the derived accumulation rates are not that far from their values found when using a one-dimensional approximation.

Unfortunately, the saw-toothed shape of the derived accumulation rates is of major concern for the reliability of all the results from the Monte Carlo analysis, as the particles are heavily influenced by the different accumulation rates they have met on their way. However, the large velocities in the area may cause this to be less of a problem, as most of the particles are allowed to quickly pass through areas of shifting too high and too low accumulation rates, being affected approximately equally much by both.

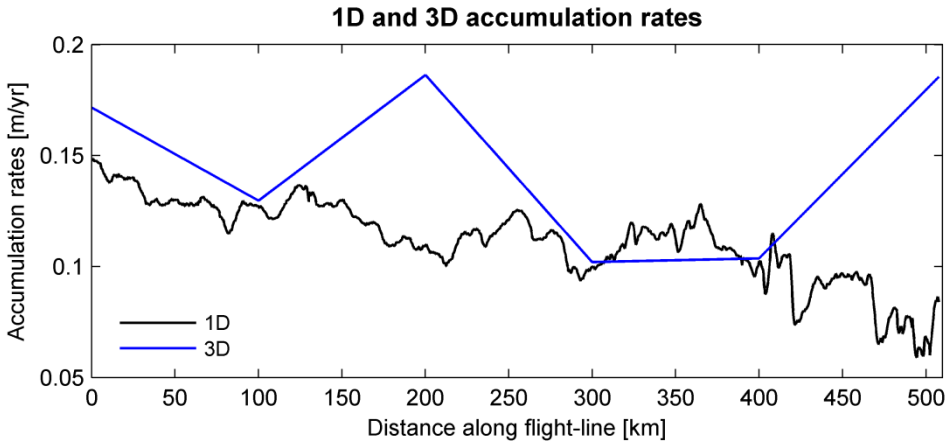

Figure 9.3: A comparison between the accumulation rates along the NEGIS as found by the Monte Carlo simulation (blue) and a one-dimensional model (black).

9.1.2. Past accumulation rates

The two constants c_1 and c_2 in the accumulation model contain information on how the accumulation rates along the North East Greenland Ice Stream have changed back in time. In figure 9.4 is shown the histograms of their marginal probability densities as determined by the Monte Carlo analysis. While the histogram for c_2 displays a nice Gaussian probability distribution with a mean value of $0.125‰^{-1}$, c_1 has a bimodal distribution, which is composite of two normal distributions centred at around $0.067‰^{-1}$ and $0.077‰^{-1}$.

The values used for c_1 and c_2 at GRIP and NorthGRIP are $0.08‰^{-1}$ and $0.18‰^{-1}$. This is somewhat higher than the values found in this study, in particular for c_2. The lower values of c_1 and c_2 along the NEGIS implies that a change in climate inflicts a proportionally smaller change in accumulation rates here than in the central part of the ice sheet.

But as mentioned in section 6.3.1, the "true" value for c_2 at NGRIP is in fact $0.14‰^{-1}$. Due to the influence of the ice ridge on the weather pattern, this relationship may be explained in terms of migration of the ice divide, on which the NGRIP ice core presently is located. It has been speculated that the reason why c_2 has a much smaller value here as opposed to at GRIP is that NGRIP during the glacial may have been situated eastwards of the ice divide (*S.J. Johnsen, pers. comm.*). This conjecture fits very nicely with the even smaller value of c_2 found along the NEGIS, situated further to the east of the ice divide.

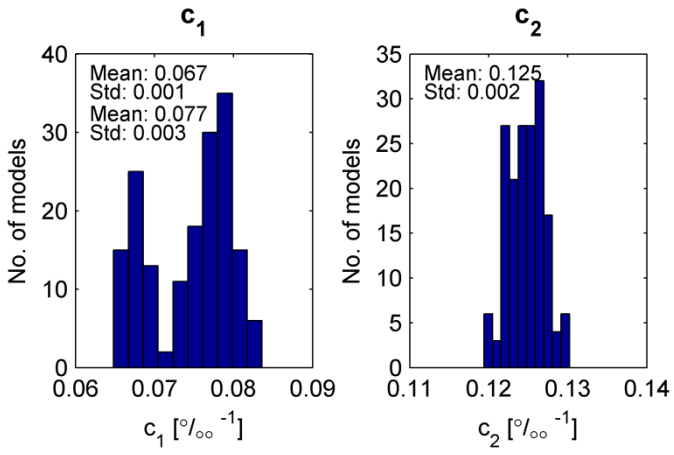

Figure 9.4: Histograms showing the posterior probability densities of c_1 and c_2. Mean and standard deviations of the distributions are given.

The derived accumulation history along the North East Greenland Ice Stream is shown in figure 9.5. For comparison is also shown the accumulation history at the NorthGRIP drill site. It is seen that with this choice of parameters, the accumulation rates along the ice stream during the last glacial were only 30% of their present-day values. At the NGRIP drill site, the accumulation rates were less than 20% of their present values.

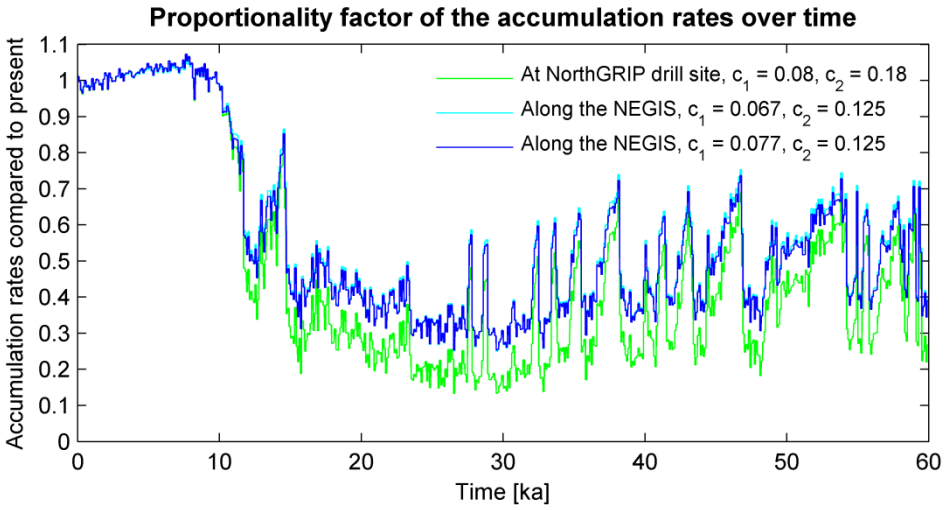

Figure 9.5: The change in accumulation rate over time, given relative to its present-day value. The time-dependence of the accumulation rates is both shown for NGRIP and for the two possible scenarios for along the NEGIS. The cyan line is behind the blue line, and is therefore difficult to see.

9.1.3. Basal melt rates along the flowline

As the main priority for the Monte Carlo simulation was to obtain an idea of how much basal melting takes place along the NEGIS, a large number of basal melt rates

were determined along the flowline. The resulting probability distribution of the basal melt rates is shown in figure 9.6. Once again, the colouring represents the distribution of sampled models, red being the most common.

Our result indicates that very large basal melt rates (close to 20 cm/yr) occur in some areas along the flowline. Both the approximate location of these and their substantial size was a very robust result, which kept showing up, even in our preliminary Monte Carlo searches. This result can be compared to that of Fahnestock et al. (*Fahnestock et al., 2001a*), previously discussed in section 3.2.3.2. They also found very large basal melt rates along the NEGIS. But in contrary to their analysis, we do not find large basal melt rates everywhere along the flowline. Rather, areas with large basal melting are intermittent with areas where no basal melting occurs at all. Along a large portion of the profile, the basal melt rates are consistently equal to zero.

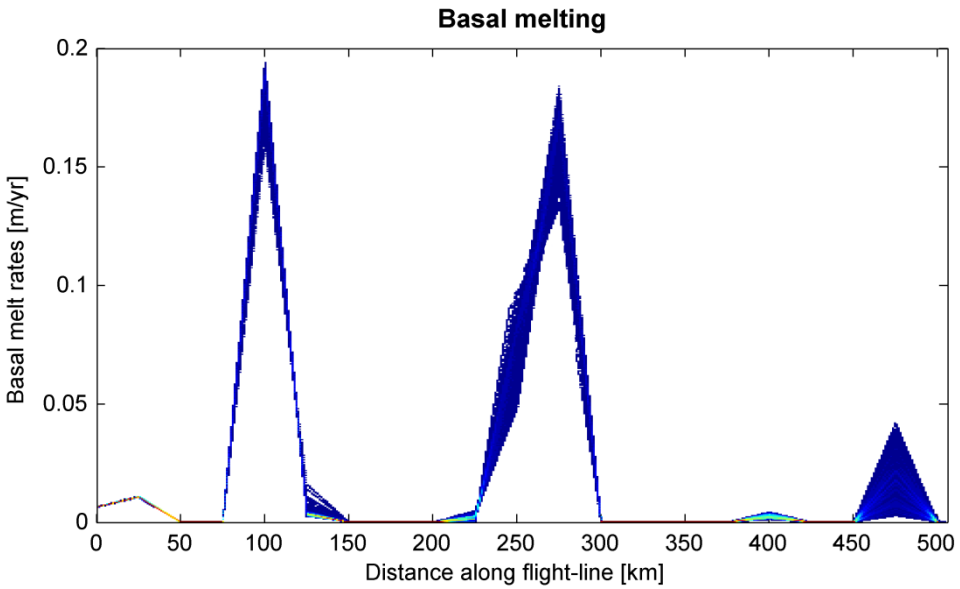

Figure 9.6: Density distribution of the basal melt rates along the NEGIS as found by the Monte Carlo search. Red denotes areas with a high concentration of sampled models, while blue areas have a lower concentration of models.

We could have allowed for a positive basal mass balance to exist along some parts of the flowline (i.e. "negative basal melt rates"). This would correspond to freezing of material to the base of the ice sheet. Refreezing of material may occasionally happen at some places, in particular where large amounts of melt water are produced closely inland (see section 3.1.3.2).

To see the effect on the derived values of the parameters when basal freezing was taken into account, we made a small test run, where the basal mass balance along the

flowline was allowed to take positive values. The Monte Carlo search never came to equilibrium, and we will not show the preliminary results here. However, we saw the development of large basal melt rates in the same areas as above, followed by areas with refreezing. The majority of the rest of the parameters remained approximately the same as for the Monte Carlo search without basal freezing (an exception is the kink height, which will be discussed in section 9.1.5).

Generally, the basal melt rates are most well-defined in areas where they approach zero, which merely is due to the fact that they would prefer to be negative in these areas. Another well resolved feature is the melt rates in the beginning of the flowline. Here, they are determined to be 6.4 ± 0.1 mm/yr, increasing slightly to 10.6 ± 0.2 mm/yr, and then dropping to zero at 50 km from the beginning of the flowline. This is of the same order of magnitude as suggested by a previous study of the basal melt rates along the flowline between GRIP and NGRIP (*Buchardt and Dahl-Jensen, 2007*), and as determined from the NGRIP ice core (*Dahl-Jensen et al., 2003*).

The highest melt rates along the ice stream, situated a distance of 100 and 275 km from the beginning of the flowline, are determined to be respectively 18.6 ± 0.7 cm/yr and 16.3 ± 1.3 cm/yr. The required energy to produce such large melt rates can be calculated from the following expression:

$$Q_{melt} = \rho L m$$

Here, $\rho = 917$ kg/m^3 and $L = 333$ kJ/kg are respectively the density and latent heat of ice, and m is the basal melt rate. Inserting these numbers, the required energy can be determined to be respectively 1.8 W/m^2 and 1.6 W/m^2.

This amount of energy can either be gained from geothermal heat (Q_{geo}), frictional heat from basal sliding ($Q_{friction}$), or from strain heating (Q_{strain}) due to deformation of the ice, most of which happens close to the bed. However, not all the energy from these sources is used for basal melting, some of it is conducted through the ice as well (Q_{ice}). Energy conservation gives:

$$Q_{geo} + Q_{friction} + Q_{strain} = Q_{melt} + Q_{ice}$$

Compared to Q_{melt}, most of these terms are small, and may therefore be disregarded. From the temperature profile at the base of the NGRIP ice core, the energy conducted through the ice at this location has been determined to $Q_{ice} = 70$mW/m^2 (*North Greenland Ice Core Project members, 2004*). A number of the same magnitude may apply for along the NEGIS. Using the relationship $Q_{friction} = u_B \tau_B$

(*Paterson, 2001, p. 226*), the frictional heat from the ice scouring over the bedrock can be calculated to be in order of 10 mW/m^2 at the first location and 100 mW/m^2 at the second location of a large basal melt rate. Therefore only the geothermal heat flux in the two areas and heat produced by ice deformation may act to produce the very large basal melt rates.

9.1.4. Basal sliding

The amount of basal sliding along the flowline is determined by the two parameters F_{B0} and λ, in combination with the derived basal melt rates. In figure 9.7 A and B is shown the histograms of the a posteriori probability density of these two variables. By using their mean values, the amount of basal sliding can be found from the basal melt rates by the relationship shown in figure 9.7 C.

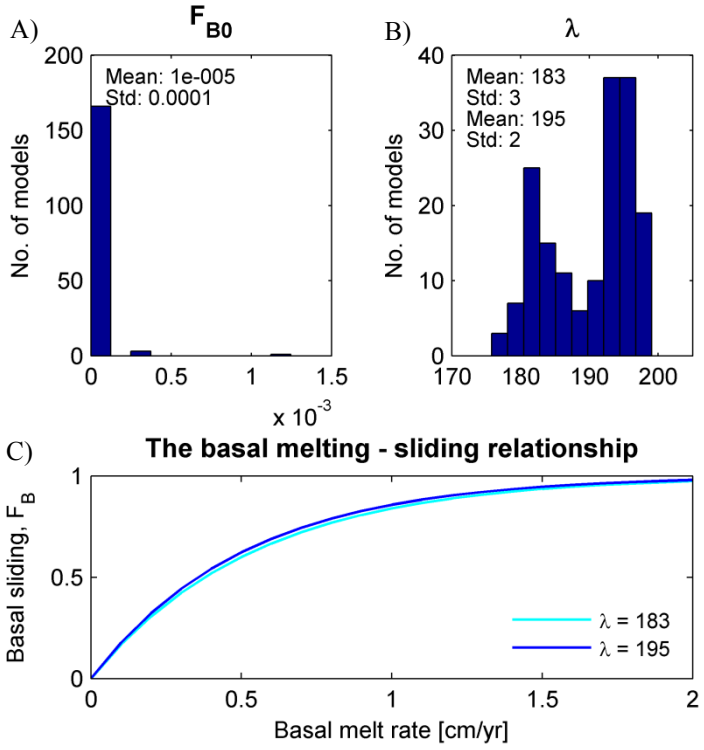

Figure 9.7: A) and **B)** Histograms showing the posterior probability densities of the two sliding parameters, F_{B0} and λ. Further sampling would probably have improved the appearance of the distributions. **C)** The resulting relationship between basal melting and basal sliding when using the mean values of the two sliding parameters.

The value of F_{B0} is very strongly determined to equal zero, hence allowing no basal sliding in areas where basal melting is not present. Such a relationship is very sensible, and is actually a common assumption (see e.g. *Buchardt, 2005*). Here, the variable was merely introduced in order to ensure that such a relationship did not

have to hold. In all ice cores, the basal sliding factor is determined to be around 0.10-0.15, independently of the occurrence of any basal melting. On the other hand, by considering the roughness of the terrain along most of the flowline profile, it is not odd if basal sliding do not occur over large areas. To take into account the influence of basal topography on the occurrence of basal sliding, we suggest a parameterization of F_{B0} with bed topography in future studies.

The histogram for λ exhibits a bimodal distribution with mean values of 183 ± 3 and 195 ± 2 respectively. The large value of λ asserts that in locations where basal melting occurs, the melt water results in large amounts of basal sliding. Almost full basal sliding is developed where the melt rates exceed 2 cm/yr (figure 9.7 C).

9.1.5. Kink height

In figure 9.8 is shown the obtained histogram for the value of the fractional kink height along the flowline. The best fitting value turned out to be quite large, namely 69 ± 1%. Generally, the kink height is low in areas with extensive basal melting and sliding. The large kink height found to apply for along the NEGIS may to some extent be explained by the pattern along the flowline of areas with enormously large basal melt rates intermittent with areas where no melting occurs. Where the melt rates are large, the ice is subjected to almost full basal sliding ($F_B \approx 1$), and the value of the kink height has little or no influence on the velocity field. The value of the kink height only really affects the velocity field where the basal melt rates are negligible. The still rather large kink height in these areas may be caused by the pronounced topography along the flowline. Basal mountains influence the velocity field by the stress and strain fields they inflict on the ice flow. One can imagine the pronounced topography to impede the ice flow by making the ice "feel" the bed higher up in the ice sheet than usual, hence giving rise to an increased value of the kink height.

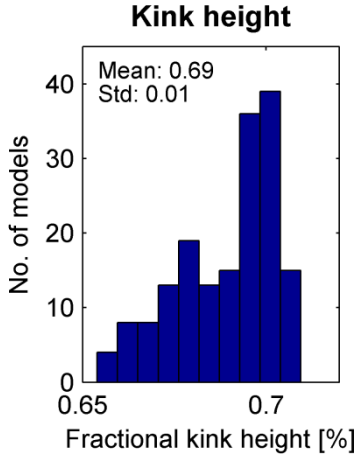

Figure 9.8: The fractional kink height as determined by the Monte Carlo analysis. A more extensive sampling of the model space would probably lead to a more Gaussian shape of the distribution.

However, it may also be an artefact. The derived kink height when also taking basal refreezing into account was substantially smaller. Both refreezing of material and a larger kink height act to compress the layering in the lower part of the ice sheet, and the high value of the kink height when not taking basal refreezing into account may be explained by this relationship.

An obvious extension of the flow model would be to allow the fractional kink height to change along the flowline. In this way, it would be possible to determine if there is a specific area along the flowline in which the kink height is abnormally high. The occurrence of such an area may have a large influence on the determination of the average kink height along the flowline.

9.1.6. Influx of material

In figure 9.9 A is shown a histogram over the value of the surface velocity in the very first part of the flowline. When using the mean values of F_{B0}, λ, k etc., this surface velocity probability distribution can be translated into a probability distribution of the influx of material entering the beginning of the flowline. A histogram of this is shown in figure 9.9 B.

By linear interpolation between the ice ridge (where the surface velocity is equal to zero) and the very first surface velocity data point, the surface velocity in the first part of the image is found to be approximately equal to 2 m/yr. The Monte Carlo simulation finds a value of 2.06 ± 0.01 m/yr, corresponding to an influx of 5747 ± 36 m^3/yr. The agreement gives confidence that this value has been correctly determined.

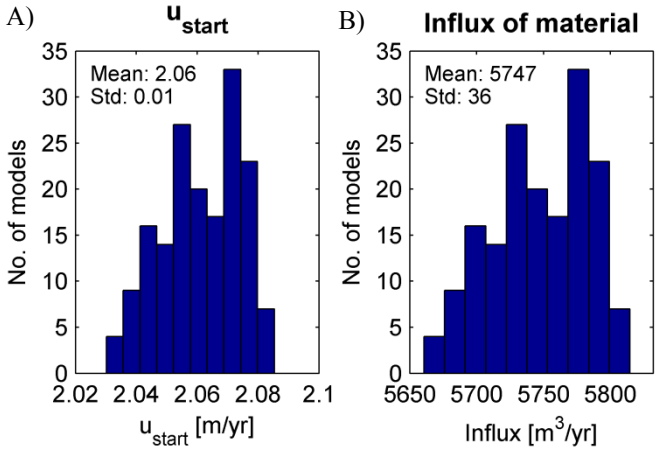

Figure 9.9: A) Surface velocity in the beginning of the flowline and **B)** the corresponding influx of material.

9.1.7. Ages of the selected layers

Due to uncertainties on the dating of the traced layers, their ages were used as flow model parameters to be determined by the Monte Carlo analysis. The resulting histograms of their posterior probability densities are shown in figure 9.10. Most of the ages are well determined by the inversion and exhibit nice Gaussian probability densities.

In table 2 is made a comparison between the ages of the layers as obtained by the Monte Carlo inversion and as determined directly from the NGRIP stratigraphy, i.e. the a priori information on which the Monte Carlo simulation is based. It is seen that despite the apparently fine determination of the layer ages by the Monte Carlo inversion, they end up quite far – too far – from our a priori knowledge of their values. Apparently, the application of a Gaussian error estimate for these ages (see section 4.1.7) was not strict enough to control the Monte Carlo search.

When comparing the obtained ages with their "true" ages, it is seen that the inversion has distorted them in a particular way. The upper layers are being assigned an age too small, while the lower layers are being assigned an age too large, such that the derived depth-age-relationship has a slightly different slope than the original one. Such a distortion must create a much better fit as otherwise the random walker would not be allowed such a movement away from our a priori knowledge. It suggests that the random walker is struggling to find a way to increase the thinning of the layers. In this way, the effect of the distortion is very similar to that of a high kink height and basal refreezing of material. The fact that basal refreezing was not taken into account may explain this distortion of the layer ages.

Given that the Monte Carlo inversion with regard to these age estimates most likely does not find their true values, this may influence the acquired values for the rest of the flow model parameters. Fortunately, it seems that the age estimates are not very strongly correlated to any of the other parameters, which may be due to their relatively minor influence on the layering compared to the influence of many of the other parameters.

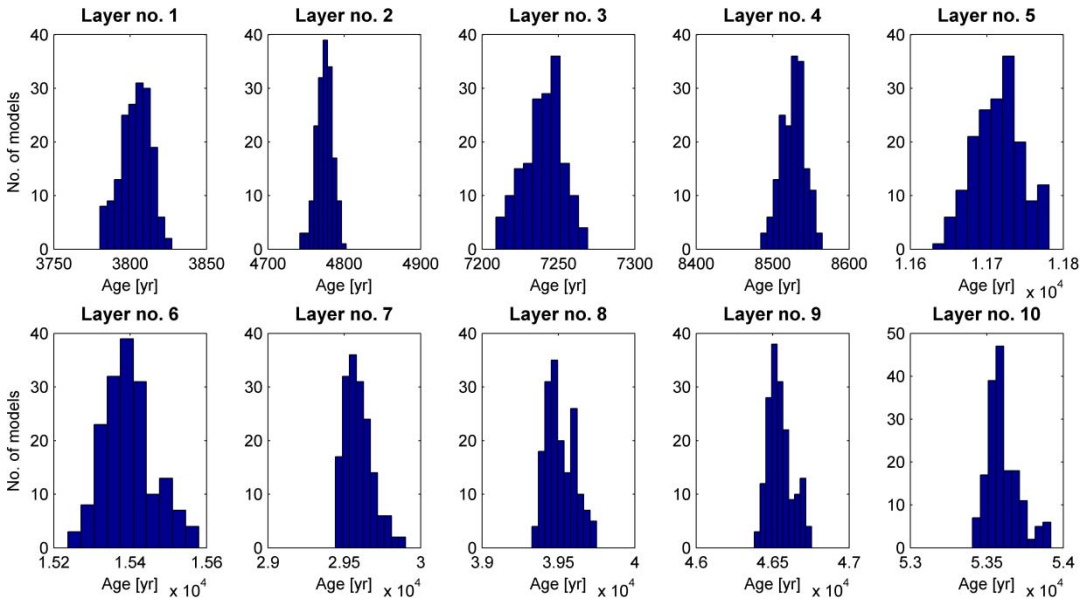

Figure 9.10: Posterior probability distributions of the age of the different layers as found by the Monte Carlo search.

Layer no.	**Age, as determined from the Monte Carlo analysis** [yr]	**Age, as determined from NGRIP** [yr]
1	3804 ± 10	4031 ± 44
2	4774 ± 11	4917 ± 52
3	7240 ± 13	7215 ± 60
4	8527 ± 16	8276 ± 73
5	11715 ± 31	11260 ± 123
6	15395 ± 66	14612 ± 184
7	29593 ± 91	28651 ± 531
8	39512 ± 94	38053 ± 759
9	46549 ± 80	45310 ± 986
10	53606 ± 105	52895 ± 1162

Table 2: A comparison between the ages of the different layers and their corresponding uncertainties as found from our a priori knowledge and the Monte Carlo search respectively.

9.2. The reconstructed layering

In figure 9.11 is shown the resulting surface velocities and internal layering when using the mean values of the different flow parameters. Where the probability distribution of a parameter was determined to be multimodal, the mean value of the most frequent of the distributions was utilized.

As was apparent from the simple analysis of the mass flux along the flowline in section 5.3, we are not able to produce an entirely correct surface velocity along the flowline due to the shortcomings of the employed mass balance equation. The calculated surface velocities are a little too high. But despite the small difference in their magnitude, the calculated and observed surface velocities match each other closely. Even many small scale variations in the observed surface velocity profile are reproduced (figure 9.11 A). Remember, that the observed surface velocity has not been used in the inversion. The two are therefore independent data sets.

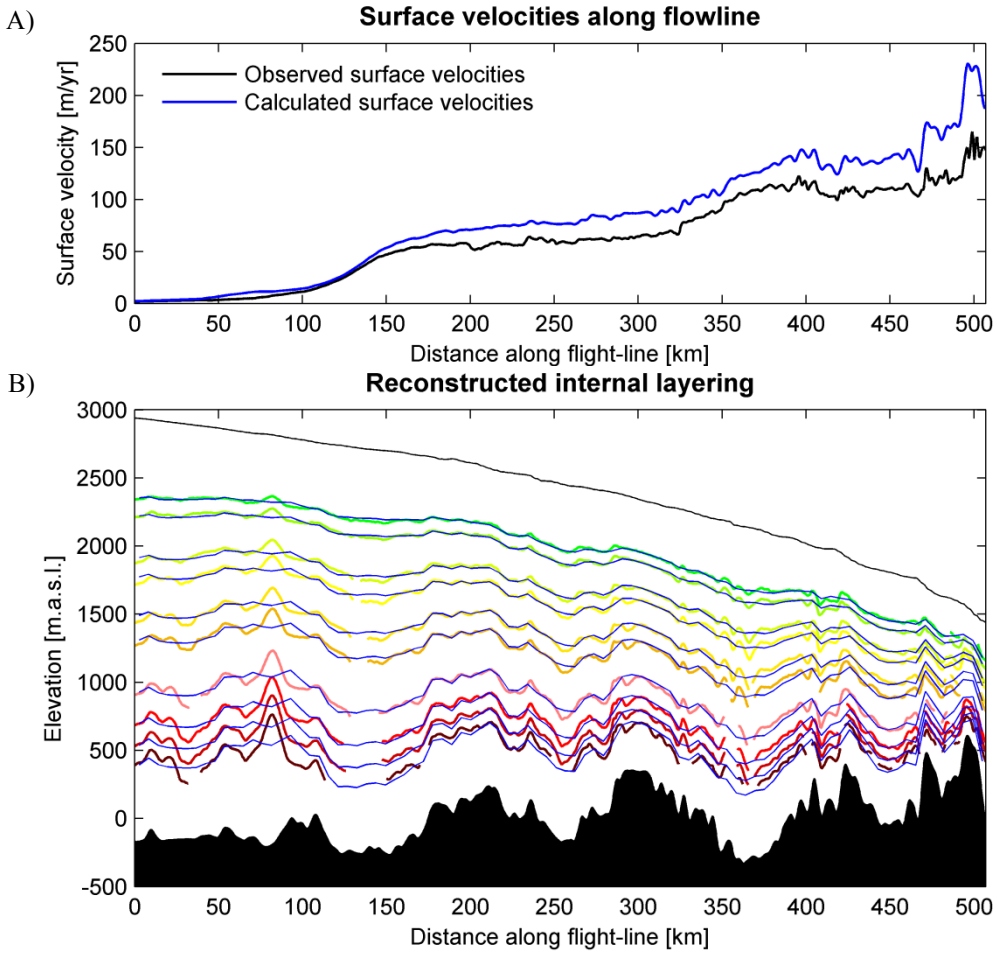

Figure 9.11: A) The calculated surface velocities and **B)** the reconstructed internal layering when using the mean values of the flow parameters derived in the Monte Carlo analysis.

Also the reconstructed internal layering is seen to match the observed layering (see figure 9.11 B). However, the modelled layers cannot achieve the same small-scale variations as the observed layers due to the fact that the basal melt rates are only determined with a mutual distance of 25 km. Undulations of the internal layering at smaller length-scales than 25 km cannot be recreated by the inversion.

In some areas, the fit between the modelled and the observed layering is better than in others. One particular area stands out where our flow model is not able to recreate the internal layering very well. This takes place in a distance of 75-100 km from the beginning of the flowline. The flow model is unable to predict the occurrence of a peculiar bulge in the observed internal layering, which has no bedrock counterpart. The fit worsen with depth as the bulge increases. The occurrence of this sudden bulge and the subsequent depression causes the model to have troubles following the observed layers in both areas. That the model is doing its best can be seen from figure 9.12, which shows a close-up of the observed and modelled layering of the area in a normalized coordinate system, i.e. when taking the bed topography into account.

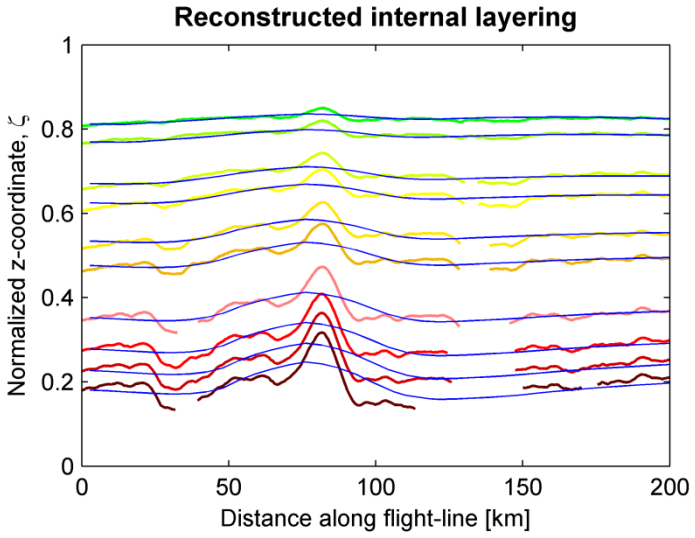

Figure 9.12: The reconstructed layering in a normalized coordinate system for the tricky area in the beginning of the flowline.

Nevertheless, along most of the profile a very nice fit between the observed and modelled layers is produced. But as it is always the case for an inverse problem, observations cannot produce true models, they can only falsify models. Hence, despite the resemblance, we will never be able to conclude that the values of the flow model parameters have been correctly determined.

Chapter 10

Improvements to the flow model

The applied flow model rests upon a number of assumptions, which more or less agree with reality. Some of the shortcomings of the flow model will be described here, along with some ideas of how these may be taken into account in future studies.

Throughout the thesis, the surface elevation of the ice sheet has been assumed constant in time. This is a convenient assumption, which simplifies the governing equations and saves us from guesswork of how the surface elevation has changed over time. But glaciers never reach a steady state. They are constantly adjusting to the changing climate. Over the last 10,000 years, however, the surface elevation of the Greenland Ice Sheet has probably been relatively stable. But the assumption of an ice cap in steady-state breaks down when going into the last glacial, in particular so as we are considering a flight-line that stretches towards the margin of the ice sheet. While the elevations in the inner part of the Greenland Ice Sheet are expected to change less than 250 m during a full glacial cycle (*Paterson, 2001, p. 346*), the margins were probably much more affected by the changing temperatures.

One possible way to avoid this problem of changing surface elevations over time is to only take layers corresponding to the last 10,000 years into account. However, we would then lack the information contained in the oldest and deepest layers. These layers are those most heavily influenced by the basal melt rates, whose determination was our primary goal. In order to improve the determination of these, we will have either to model the changing surface elevations over time during the inversion, or to use a prescribed surface elevation as a function of time from another model, despite the uncertainties attached to these procedures.

The calculation of the present-day surface velocities could also be improved. In so far as we were not able to produce surface velocities entirely similar to those observed, we might have been better off using the observed ones. But if surface

velocities that more accurately mimic the observed velocities could be calculated, this would be a significant improvement of the model, as it also would lead to a better description of the vertical velocity field in the ice sheet.

As mentioned in section 5.3.3, two factors whose influence on the surface velocities is not taken into account in the flow model are a change in ice thickness and horizontal velocity profile transverse to the flight-line ($\partial H/\partial y$ and $\partial F/\partial y$). Also the effect of a changing horizontal velocity profile along the flight-line ($\partial F/\partial x$) is neglected. Due to the large surface velocities in the area and the apparent abruptness of the basal sliding factor F_B, this factor may potentially have a very large influence on the calculated present surface velocities. From equation (6.12), p. 61, the following expression can be derived:

$$\frac{\partial F}{\partial x} \approx \frac{1}{2} k \frac{\partial F_B}{\partial x}$$

By the Monte Carlo simulation, F_B was found to change from 0 to 1 over a distance of less than 25 km, which corresponds to a value of $\partial F_B/\partial x$ in the order of 10^{-5} m^{-1}. As k is in order of unity, the magnitude of $\partial F/\partial x$ is roughly the same. The term $u_s H\, \partial F/\partial x$ (in order of unity) may hence be highly influential, in particular in the fast flowing parts of the ice stream. Even with a value of $\partial F_B/\partial x$ a magnitude smaller than that derived from the Monte Carlo analysis, this term will have a significant effect. However, $\partial F_B/\partial x$ is a difficult factor to incorporate properly in the flow model due to sparse data and therefore large uncertainties.

The basal melt rates could also be allowed to change over time in response to the varying climatic conditions at the surface. To take this into account would require the incorporation of a thermo-mechanical model, which would slow down the random walker significantly. At NGRIP, however, the basal melt rates have been established to have changed only 1 mm/yr during the last 100 ka (*Dahl-Jensen et al., 2003*). This is not much compared to the large basal melt rates found in this study for along the NEGIS, and the incorporation of varying melt rates over time may therefore not improve our results significantly.

It must be kept in mind that whichever improvements we make to the flowline model, it is still a very simple flow model with its inherent limitations. The flow law of ice is completely disregarded, and also the model is unable to take into account 3D-effects such as the stress and strain fields arising from the irregular bedrock along the flight-line. Much more complicated models are required to properly represent the influence of these.

Chapter 11

Discussion

11.1. Importance of bedrock topography

The presence of the subglacial trough beneath the North East Greenland Ice Stream is often mentioned as a possible cause for the existence of the ice stream. Indeed, the significance of the trough for the flow pattern of the ice stream is undeniable. For instance, the surface velocities are observed to be enhanced over the channel area compared to the surrounding bedrock, see figure 11.1 C and D.

Yet, the channel is not fully developed along the entire ice stream. In the upper reaches of the ice stream, there is little or no evidence of any channel (figure 11.1 A and B). First around 300 km the trench has become a distinct feature, and the ice flows most rapidly here (figure 11.1 C). But the width of the ice stream is significantly larger than the channel, and the ice in the ice stream flows only 20 m/yr faster in the trench than it does where no trench exists. Even where the channel is most prominent, the ice stream is not restricted to it (figure 11.1 D). Further towards the margin, the bed becomes very rough, and at some places it is difficult to distinguish the channel. Also, in figure 11.1 E, no obvious connection exists between the bedrock topography and the surface velocity.

For these reasons, we consider the channel by itself to be insufficient for explaining the flow pattern and geometry of the ice stream, not to mention the initiation of enhanced flow very far inland the ice sheet. That the area of enhanced flow closely follows the trench may predominantly be due to the increased erosion in the area combined with the positive feed-back mechanisms hereof. These are e.g. the larger ice thickness and the impact on the water transportation below the ice sheet, which is crucial for where basal sliding takes place in response to the potentially large basal melt rates.

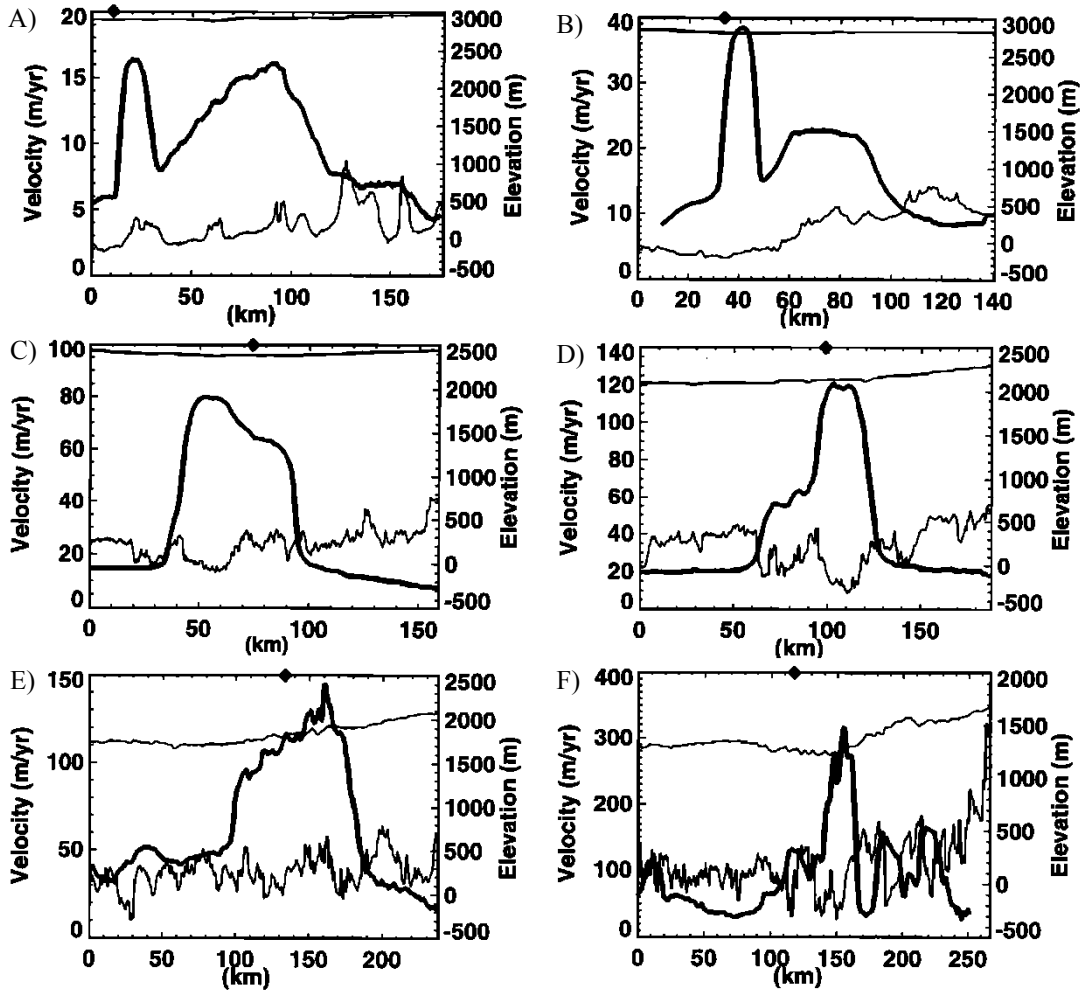

Figure 11.1: A comparison between bedrock and surface topography (thin black lines) and the surface velocity (thick black line) transverse to the ice stream. The data are from the following approximate distances from the beginning of the considered flight-line: **A)** 90 km, **B)** 130 km, **C)** 310 km, **D)** 390 km, **E)** 460 km and **F)** 540 km. The intersection of the profiles with the flight-line is marked with a black diamond at the top of each image. Figure from *Joughin et al., 2001*.

Also the large-scale topography in the area around the North East Greenland Ice Stream has an impact on the ice stream flow. Usually ice flow is divergent within the interior of an ice sheet, but in this area the highlands to the south east and north of the ice stream basin (see figure 4.4, p. 25) make the ice flow convergent. In particular the highland to the south east of the ice stream, which forms the eastern boundary of the drainage basin of the NEGIS, forces the flowlines to converge towards the ice stream. This results in increased flow velocities in the upper reaches of the ice stream.

But although the basal topography of the surroundings in this way very likely contributes to the initiation of the ice stream, it cannot explain why the ice stream begins as such a sharply defined feature.

The extent to which basal topography can explain the existence of the North East Greenland Ice Stream may be resolved by the use of three-dimensional ice sheet models. In figure 11.2 is shown the resulting surface velocities when running the ice sheet model "Elmer" without taking basal sliding into account. The model is showing fast ice motion in the area around Jakobshavn Isbræ, but less around the NEGIS. This suggests that variations in bed topography and simple mass predictions are not sufficient to explain the rapid flow in the NEGIS area. However, as the subglacial trench below the NEGIS is not adequately resolved by the employed bedrock grid, the effect shown in figure 11.2 may primarily be due to the surrounding highlands.

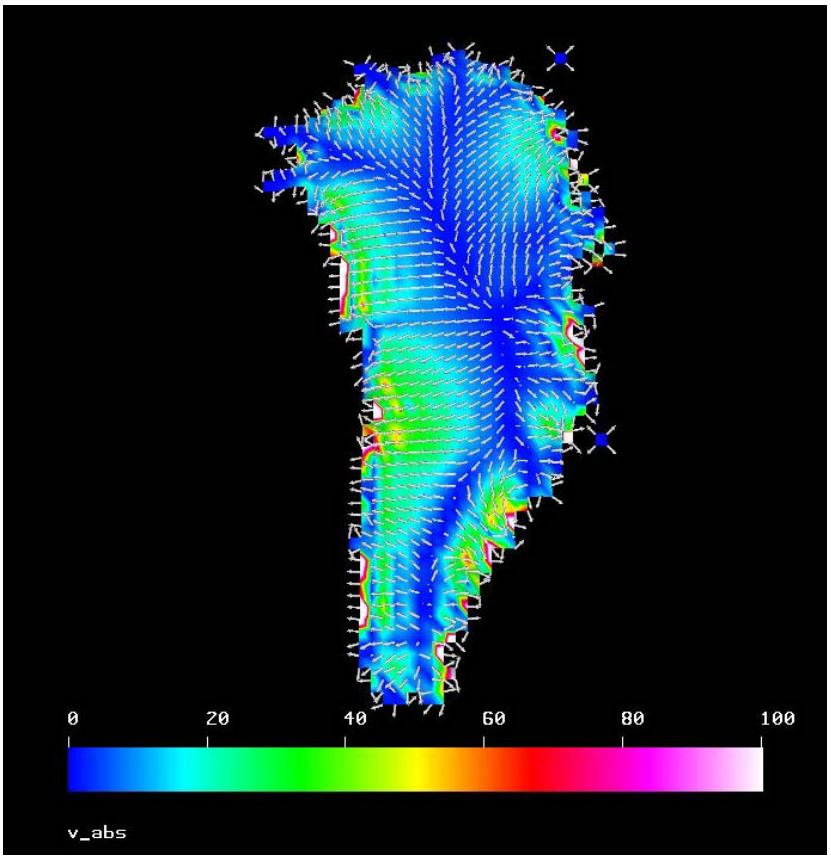

Figure 11.2: Calculated present surface velocities of the Greenland Ice Sheet when running the ice sheet model Elmer at a 40x40 km grid resolution. The model is fully coupled, but basal sliding is not taken into account. Units are in m/yr. A cut-off is introduced at 100 m/yr, with white areas denoting surface velocities larger than this. Courtesy: Thomas Zwinger and Ralf Greve.

11.2. Importance of basal melting and sliding

Many factors indicate that extensive basal melting takes place in at least some areas along the NEGIS. Basal sliding due to the presence of this melt water may hence be the most important factor for the existence of the ice stream. Though our analysis does not provide an unambiguous picture of to what extent basal melting and sliding occur along the ice stream, it still provides a hint of what may be the answer to these questions.

11.2.1. Comparison of model results

Judged from the visual appearance of the layering alone, basal melting does not seem to be a widespread phenomenon. The layering is to a large extent just following the undulating bedrock topography. Yet, in some areas – and most evidently so in the beginning of the flowline – the layering exhibits strange undulations with no bedrock counterparts, hence suggesting basal melting to occur in at least specific areas along the flowline. The results from the Monte Carlo simulation point to the same conclusion, although these suggest the basal melt rates to be even more localized.

In section 5.2, the thinning rates along the flowline were calculated by use of a one-dimensional approach. Along the first 50 km of the flowline, very small thinning rates were found. In some areas they even achieve negative values (figure 5.3). Hereafter, the thinning rates slightly increase, for again to become very small in the area from 100 to 150 km from the beginning of the flowline. Subsequently, the thinning rates are steadily increasing towards the margin, only attaining small values again in a very confined area around 300 km from the beginning of the flowline.

Attributing the presence of these small thinning rates to be at least partly caused by basal melting, a similar pattern emerges from the Monte Carlo analysis. Along the first 50 km of the flowline, the basal melt rates were determined to be around 1 cm/yr, while at 100 km from the beginning of the flowline a major peak in the basal melt rates was found. A second area with large basal melt rates was found to be situated at 275 km from the beginning of the flowline.

In this context, one should keep in mind that due to the dramatic increase in velocity along the flowline, a one-dimensional approach may be applicable in the very first part of the flowline, but it will have severe limitations elsewhere. Analogously to the analysis in chapter 7, a two-dimensional approximation as opposed to a one-dimensional approximation causes the effect of any given parameter to be distributed over a larger area, while having a correspondingly smaller effect at any place. This may be the reason why the one-dimensional model generally predicts basal melting

to occur over a larger area compared to the results of the Monte Carlo simulation. The larger velocities downstream may also explain why the influence of the very large basal melt rates at 100 km have approximately the same effect on the derived one-dimensional thinning rates as the comparably small basal melt rates in the beginning of the flowline.

In section 5.2 was also made a comparison between the derived one-dimensional accumulation rates when using respectively a kink model and a sandwich model without basal melting. From this comparison we were able to put forward the suggestion that a high degree of basal sliding may exist along the last part of the flowline, i.e. from 300 km and onwards.

The extensive basal sliding may e.g. be caused by a changing composition of the geological substrate on which the ice sheet is resting. In this area, the bed topography has become quite rough, and the existence of a sedimentary bedrock that allows basal melt water to drain away is not very likely. Consequently, basal sliding may be important even where no basal melting occurs. It is also in this area that the subglacial trench is starting to develop into a distinct feature of the bed. The implications of the trench for the subglacial water transportation in the area may also act to enhance the basal sliding.

Yet, the results of our Monte Carlo simulation do not suggest basal sliding to be important outside areas of basal melting. Instead, the results indicate basal melt water to be very influential for the amount of basal sliding. And with the occurrence of small but non-negligible basal melt rates at several locations along the last part of the flight-line, the suggested amount of sliding in this area is actually quite significant. This gives credibility that basal sliding may indeed be very important for ice flow along last part of the ice stream. The reason why the Monte Carlo simulation suggests no basal sliding to take place along some parts of the NEGIS may be that the flight-line is repeatedly crossing into and out of the subglacial trench beneath the main ice stream. It may be that basal sliding is only significant inside the trench.

The coherence between the results derived from very simple models and the more complicated three-dimensional flowline model used in the Monte Carlo simulation suggests the results from the Monte Carlo analysis to be quite reliable. Due to deficiencies of the model and the assumptions upon which the model is resting, the values of the melt rates along the flowline may not have been determined correctly. But if the assumption of a flowline is adequate, the pattern of where basal melting exists is probably nonetheless quite accurate.

11.2.2. The flowline assumption

Due to the convergent flow in the area, even a small digression of the flight-line from a true flowline may have major consequences for where the ice originated, and hence on the results of the analysis. It is therefore extra important that we are dealing with an approximate flowline. In section 5.1, the assumption of a flowline was investigated, and it was found that along its first 500 km, the flight-line is fairly close to a flowline. But the question remains whether the discrepancy is sufficiently small that the conditions of ice flow can be assumed to be the same along the flowlines as along the flight-line.

If the assumption of a flowline is not adequately fulfilled, basal melting does not have to be as highly concentrated as indicated by the Monte Carlo analysis. The ice originating from outside the flight-line may instead have experienced smaller basal melt rates over a longer distance. From the internal layering in the considered radio echogram we have little possibility of investigating this matter.

In the area around the first location of enhanced basal melt rates as found in the Monte Carlo analysis, the flight-line is slightly off the location of a true flowline. In figure 11.3 is shown a close-up of where two particles ending on this part of the flight-line truly have originated, superimposed a map of the bed topography. The particles are seen to originate west of the flight-line.

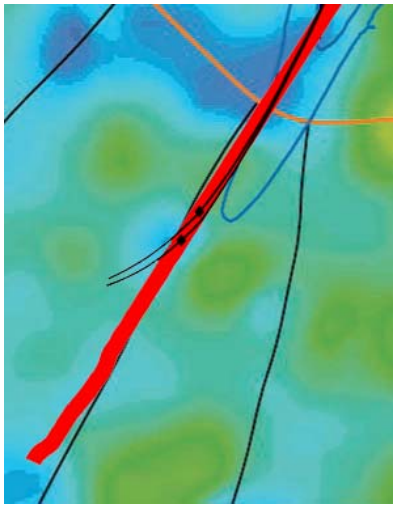

Figure 11.3: The paths of particles (thin black lines) crossing the flight-line (thick red line) in a distance of respectively 80 and 90 km from its beginning. The locations of crossing are marked by black dots. The particle paths are superimposed a map of the bed topography in the area (blue is lower elevations). Also shown are flowlines originating at the edges of the drainage basin (thicker black lines), elevation contours in the basin (orange line) and ice stream speed contours (blue lines).

By inspection of the map in figure 11.3, it is seen that the particles arriving at 80 and 90 km from the beginning of the flight-line have followed a very similar path, even though they do not follow the flight-line. The general interpretation of the bulge in the internal layering at 80 km is that exactly this area experiences no basal melting (and hence represents the layering in the usual case of no melting at the base), while

melting occurs at both its sides, dragging the layers down. At 90 km the layers are again situated in a much deeper position (see figure 9.12). As the flight-line apparently does follow a flowline between 80 and 90 km, the presence of this sudden undulation is an indication that heavy basal melting indeed takes place at this location. The same conclusion was drawn from the Monte Carlo analysis.

However, the magnitude of this bulge in the internal layering is exceptional, and we speculate whether its occurrence can be explained by other factors than basal melting in the surrounding areas. Possibly, basal topography may exert an influence, since it is able to change the flow pattern of the ice by e.g. causing material to flow around obstacles instead of over them. This process mainly affects the lowermost part of the ice, and at crests in the bedrock topography the layers may be dragged down by disappearance of material to the sides. The importance of this process is difficult to assess. Yet, by a first look on the map of the bed topography in figure 11.3 it is questionable whether the bedrock topography can offer a sufficient explanation for the existence of such a large bulge at this location.

At the second location where the Monte Carlo inversion predicts a very large basal melt rate to exist (at 275 km), the flight-line has been following a flowline very accurately for at least 100 km (figure 11.4). Hence, for the area between 175 and 275 km, the assumption of a flowline is very appropriate. However, due to the large velocities along the ice stream, some of the particles making up the lowest layers at this location may originate further upstream than 100 km, where the assumption of the flight-line being a true flowline is not quite as good. Just after around 275 km, the flight-line starts to follow a slightly different path than the flowlines, which are diverging around a small mountain at the bed. It is also in this area that the trench in the bedrock topography begins to appear on the map.

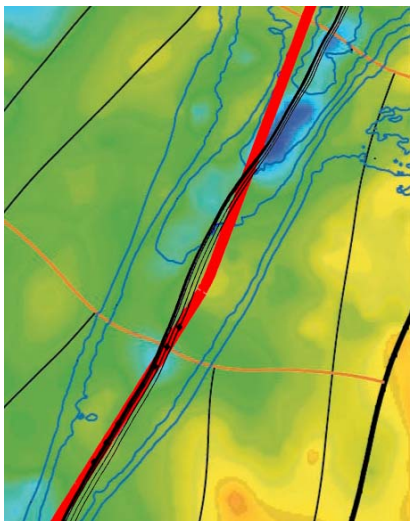

Figure 11.4: The paths of particles (thin black lines) crossing the flight-line (red) between 205 and 275 km from its beginning with a mutual distance of 10 km. The locations of crossing are marked by black dots. The paths are overlain a map of the bedrock topography in the area (blue is low elevations, yellow is higher elevations). Also shown are flowlines originating at the edges of the drainage basin (thicker black lines), elevation contours in the basin (orange line) and ice stream speed contours (blue lines).

11.2.3. Comparison between melt rates and the locations of high velocity increase

The Monte Carlo analysis indicates two locations with very large basal melt rates to exist along the ice stream. If this result is correct, the heavy basal melting at these locations is probably sufficient to explain the onset of rapid flow of the North East Greenland Ice Stream. By comparison of the results from the Monte Carlo inversion with the observed surface velocity profile along the ice stream, an agreement is seen between the two locations of enhancement of the flow velocities and the locations of large basal melt rates.

Starting shortly before 100 km, the surface velocity along the flight-line exhibits a five-fold increase (see figure 4.8, p. 31). The first major basal melt rate inferred by the Monte Carlo analysis appears in the very same area. It is hence tempting to suggest the occurrence of basal melt water to cause the onset of rapid flow in the region.

Unfortunately, this is exactly in the area where the flow model is not able to reproduce the internal layering very accurately, and we must therefore display some caution when concluding on behalf of the derived basal melt rates etc. for this area. However, the main reason why the Monte Carlo analysis is struggling to fit the layering in this area is probably the strange bulge in the layering, which is difficult to explain if not invoking large basal melt rates. Also Fahnestock proposes very large basal melt rates to exist in this area (it is the area denoted “B” in figure 3.4) (*Fahnestock et al., 2001a*).

The second increase in surface velocity along the flight-line starts around 320 km. This is somewhat later than the second major basal melt rate, which the Monte Carlo simulation predicts to be situated at 275 km. However, as described in the previous section, just after 275 km the flight-line no longer follows a true flowline. And due to the large spatial variation of the surface velocities in the area, the surface velocity profile can be very different along a flowline. In figure 11.5 is shown a comparison between the surface velocities along different flowlines, all starting at the flight-line, and the surface velocity along the flight-line for this area.

An important feature of figure 11.5 is the way the surface velocity along the flight-line (red) increases more rapidly and in a much more defined section than the surface velocity along the flowlines (black). This is due to the fact that the flight-line repeatedly moves away, towards and across the place where the velocity of the ice stream is at its maximum. Similarly to the surface velocity along the flight-line, the surface velocity along the flowlines is approximately constant from 175 km and

onwards. But when following these, the subsequent increase in velocity appears to start around 275 km, i.e. at the very same location as the second major basal melt rate. Only when the flight-line approaches the main ice stream again, an equivalent velocity rise is seen along the flight-line.

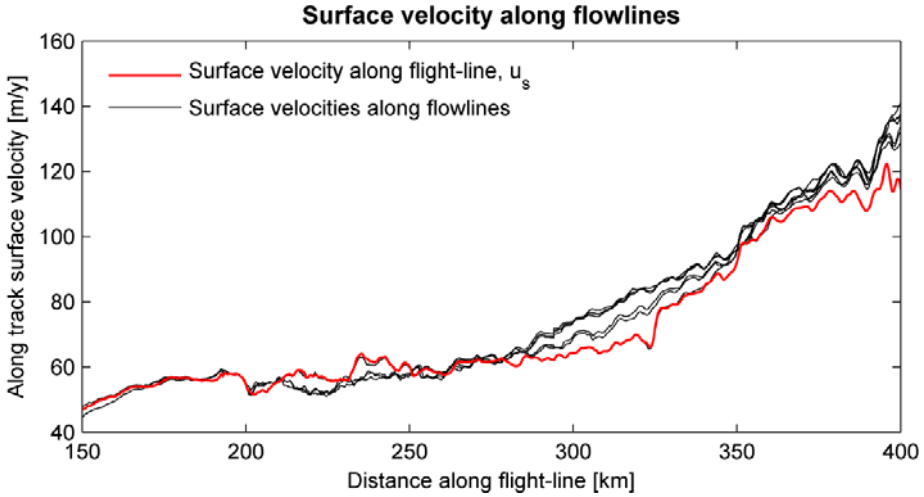

Figure 11.5: A comparison between the surface velocity profile along the flight-line and the surface velocity along some of the flowlines depicted in figure 5.2. The velocities of the flowlines have been projected onto the x-axis of the flight-line.

It must, however, be kept in mind that the calculated accumulation rates resulting from the Monte Carlo analysis turned out not to be reliable along some parts of the flight-line. For the first part of the flight-line, the calculated accumulation rates fit reasonably well with those derived from the one-dimensional approximation (figure 9.3), which again correspond well with data from other sources (section 5.2.2). Hence, no problem occurs when dealing with parameters that apply for this area, and the ill-defined nature of some of the accumulation rates does not affect the magnitude or location of the first large basal melt rate. But for this second melt rate, it may be influential.

Also from the visual appearance of the internal layering in this part of the flight-line, the existence of the second major basal melt rate is much more uncertain than the first. Not only is the layering very disturbed, but the higher horizontal velocities also cause the effect of any flow parameter to be distributed over a very large area, thus rendering it difficult to distinguish it.

The location of the second jump in surface velocity also coincides with the first major partition of the ice stream. Hence, both the division of the ice stream into two flow features and the increase in velocity may be due to three-dimensional processes.

A possible explanation may e.g. be the effects of the diverging flow around the small subglacial mountain at this location.

Three-dimensional processes due to bed topography are probably the cause of a third major velocity increase, which takes place around 500 km from the beginning of the flight-line. This jump in velocity coincides with the sudden appearance of a sticky spot in the middle of the main ice stream course (see figure 4.7). Being a major obstacle to the ice flow, the ice diverges around the spot, hence increasing the mass flux and ice flow velocity in other areas of the ice stream. Yet, this sticky spot is a much more prominent feature than the small bedrock mountain found at 300 km. Another difference is the only small basal melt rates inferred for the area around 500 km. The processes governing the increase in surface velocity at the two locations are therefore not necessarily the same.

In short, our findings point towards the conclusion that very large basal melt rates exist at specific locations along the ice stream, and that these may be responsible for some of the major velocity increases along the ice stream.

11.2.4. A volcanic origin?

The Monte Carlo inversion suggests two areas of basal melting to exist along the flight-line. These two areas have basal melt rates of respectively 18.6 and 16.3 cm/yr, and both appear to be restricted to a very small area ($<$ 50 km). Their localized nature imposes strong constraints on the cause of their occurrence, rendering it difficult to suggest other than a local heat source to be situated at the bed. In case of Jakobshavn Isbræ, very large melt rates – even higher than these – are produced in response to high deformation rates in a thick layer of ice at the pressure-melting point (*Truffer and Echelmeyer, 2003*). But such a thick layer of ice at the pressure-melting point must persist over a large area. It cannot suddenly appear and disappear within less than 50 km.

Hence, if we are to trust the results of the Monte Carlo simulation, a geological structure that is an efficient geothermal heat source must exist in some areas below the ice sheet. Such a local heat source may e.g. be of volcanic origin as suggested by Fahnestock et al. (*Fahnestock et al., 2001a*). The required energy of the large basal melt rates was calculated to be respectively 1.8 W/m^2 and 1.6 W/m^2 (section 9.1.3). In an active volcano beneath an ice sheet, the heat flux can locally reach as high values as 15-20 W/m^2 (*Bjornsson et al., 2005*).

From this study it is not possible with any certainty to propose a specific bedrock feature to be a subglacial volcano or the remnants of such one. Nevertheless, we wish

to draw attention to a previous study by Joughin et al. (*Joughin et al., 2001*), in which a bedrock obstacle, situated very close to the location of our first major basal melt rate, was given some attention. In his study, Joughin states without further elaboration that he believes this feature to play a significant role for the onset of the enhanced flow. He bases the conjecture on the fact that its location coincides with the first increase in velocity, and that its dimension transverse to the flowline equals the width of the ice stream. This subglacial mountain, along with how the surface velocity changes across it, was portrayed in figure 11.1 A, p. 110. From the derived occurrence of large basal melt rates in the exact same area, it is tempting to suggest the feature to be of volcanic origin.

Fahnestock, on the other hand, proposes a volcanic feature to be situated further south of the ice stream (*Fahnestock et al., 2001a*). This feature is, however, situated some distance away from the increased velocities of the main ice stream. But it may coincide with the origin of the so-called southern tributary, which merges with the main ice stream between 150 and 200 km from the beginning of the considered flight-line (section 4.3.3).

The large basal melt rates may also be formed by less spectacular means. They may e.g. be the response to a large geothermal heat flux due to a thinner crust in this area, possibly much like in the geothermally active areas of Iceland. And once again we will emphasize that it all rests upon the results of the Monte Carlo inversion, which may not be entirely accurate.

Chapter 12

Conclusion

Evidence for active ice sheets is mounting. Rapid changes are observed to occur in the margins of the ice sheets, and ice sheet models that are able to recreate these rapid changes are yet to be developed. Increased discharge due to fast flowing ice streams, which stretch far into the interior of the ice sheets, is one possible way in which ice sheets can quickly respond to a change in climate. However, a better insight into the processes governing ice stream flow is required before these can be incorporated into any ice sheet model.

The mechanism dominating the ice flow in the North East Greenland Ice Stream was investigated by use of simple flow models. It was demonstrated that the large horizontal velocities in an ice stream cause a one-dimensional approach to be insufficient. The limitations of this approach were revealed when using it to calculate the present accumulation rates, as the bed topography turned out to play a prominent role for the location of the upper layers.

Due to the highly convergent flow in the area also a two-dimensional approximation is insufficient for adequately representing the ice flow along the ice stream. It was therefore necessary to account for the three-dimensionality of the problem the best way as possible within the limits of a flowline model. Based on this, a three-dimensional flowline model based on a simple Dansgaard-Johnsen velocity profile was developed.

Although not unambiguous, the Monte Carlo inversion of the three-dimensional flow model does give some indications of the driving forces behind the North East Greenland Ice Stream. Our results point towards the conclusion that the fast flow in the ice stream is not a result of the basal topography of the area. Nor is it due to widespread basal melting along the flowline. In contrary, very large basal melt rates are found in certain areas, intermittent with areas where no basal melting occurs.

These surprisingly large and localized melt rates are difficult to explain without invoking the presence of some geological features which act to significantly raise the geothermal heat flux in these areas.

Unfortunately, the prescribed flow model is not able to fully represent the complicated ice flow along the ice stream, and the inherent three-dimensionality of the problem still poses serious problems. It is highly important that our flight-line, along which we make the analysis, comes very close to a true flowline. Also the bedrock topography transverse to the flowline may play a significant role for the ice flow in the area. The influence of these factors should not be overlooked, and they impose considerable uncertainties on the acquired results.

A model that is able to take the three-dimensional effects properly into account, and that is adapted to find such localized basal melt rates, has to be employed before any conclusive determination of the basal melt rates along the ice stream can be obtained. Only then may we with certainty be able to attribute the presence of the North East Greenland Ice Stream to these large and localized basal melt rates.

Appendices

Appendix I

In order to obtain the best possible layering in a RES image, the distance over which the unprocessed return signal is averaged has to be chosen carefully. In figure I.1 A is shown an idealized radio-echo sounding record from a given location, representing a sequence of ten thick layers, regularly spaced with a distance of 10 pixels. In between these layers, thinner layers exist which do not reflect as strongly as the thicker ones. The spacing and thicknesses of this layer sequence mimics the major layering observed in radio echograms from Greenland. The return signal of the individual layers decreases with depth (here represented by pixel), imitating the decreasing signal associated with signal attenuation at greater depths.

Three enhancements of the radar return signal have been applied, each using a different averaging span. From figure I.1 B, it is seen that when using a span much larger than the mutual distance between the thick layers (namely 51 pixels), the shape of the peaks is distorted. Also, the return signals from the thinner and less reflecting layers are somewhat smaller than the signal from the thicker layers. Hence, a span of this size will cause thin layers to be undetectable in the resulting RES image, and consequently it will diminish the resolution of the image.

However, if the span is smaller than the distance between two of the major layers of the radar signal, the importance of the thin layers is much exaggerated, while the thick layers almost disappear (figure I.1 D). If the span is much smaller, new layers may be created in the resulting image in between the actual layers, thus increasing the noise of the image (figure not shown).

The best size of the span is found to be approximately equal to the distance between the major layers, i.e. 11 pixels (figure I.1 C). In this case, the shapes of the peaks are preserved, and the signals from the thin layers are enhanced to be almost as significant as the thicker layers. Note, that areas with no or little layering will appear grey.

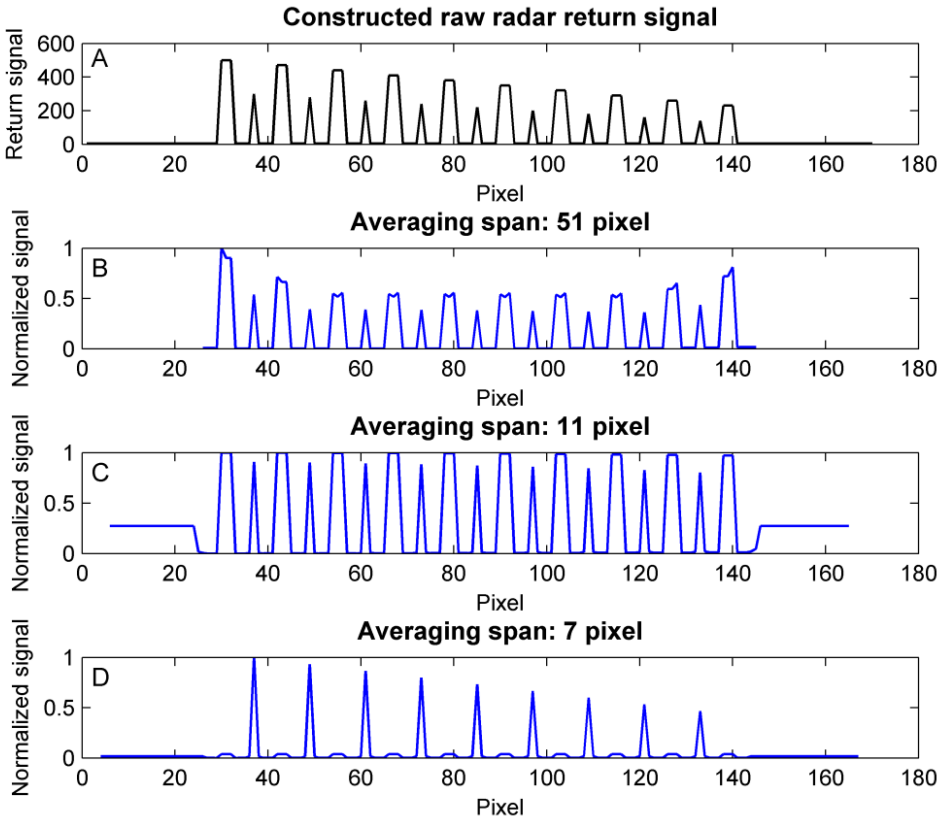

Figure I.1: A) A constructed RES signal from a layer sequence. **B)**, **C)** and **D)** Enhancements of the radar return signal when using different sizes of the averaging span. The resulting values have been normalized. A signal value of 0 corresponds to white on the RES image, while a value of 1 corresponds to black.

Using an averaging filter of this size on a real RES image produces the image, which best preserves the fine structure of the original radar return signal. Some thick layers will appear more pronounced when using a larger span, but this comes at the cost of a loss in the finer details of the layering, which are important when digitizing. Thus, an averaging filter with a span of 11 pixels has been chosen to enhance the contrast of the raw radio-echo images from along the NEGIS.

The above method is a very simple way of enhancing the contrast of RES imagery. However, as the main reason here for processing the raw RES images is to increase the visibility of some of the more prominent deeper layers, there is no need for using a highly complicated method of contrast enhancement.

Appendix II

RES image from along the North East Greenland Ice Stream

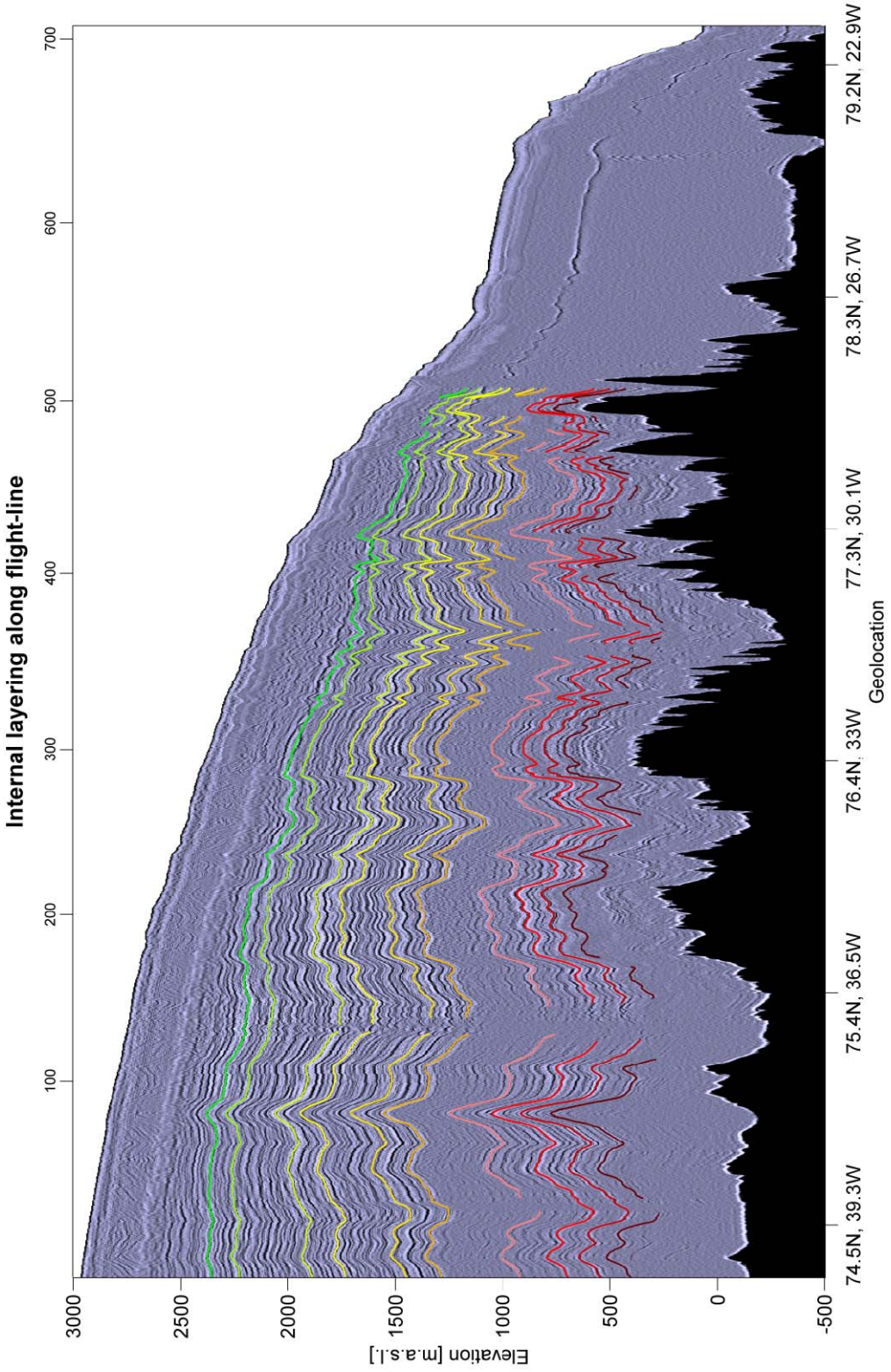
Internal layering along flight-line
Elevation [m.a.s.l.]
3000
2500
2000
1500
1000
500
0
-500
100
200
300
400
500
600
700
74.5N, 39.3W
75.4N, 36.5W
76.4N, 33W
77.3N, 30.1W
78.3N, 26.7W
79.2N, 22.9W
Geolocation

Appendix III

Assume a very simple horizontal velocity profile, which is constant with depth:

$$u(z) = u_s$$

When applying the continuity equation in two dimensions:

$$\frac{\partial u}{\partial x} + \frac{\partial w}{\partial z} = 0$$

the following expression for the vertical strain rate component, $\dot{\varepsilon}_z$, is obtained:

$$\dot{\varepsilon}_z \equiv \frac{\partial w}{\partial z} = -\frac{\partial u}{\partial x} = -\frac{\partial u_s}{\partial x}$$

From this relationship, we can conclude that as $\partial u_s/\partial x$ is independent of z, so must also $\dot{\varepsilon}_z$ be. With this knowledge, $w(z)$ can be found by integrating $\partial w/\partial z$ from a position z to the surface, S:

$$w(S) - w(z) = \int_z^S \frac{\partial w}{\partial z} dz = \int_z^S \dot{\varepsilon}_z dz = \dot{\varepsilon}_z (S - z)$$

The vertical velocity component at the surface of the ice sheet is equal to minus the accumulation rate, i.e. $w(S) = -a$. The minus sign stems from the fact that the z-axis is chosen to point upwards. The vertical velocities are then negative, as the ice is moving downwards. By inserting this relationship into the above equation, we get:

$$w(z) = -a - \dot{\varepsilon}_z \cdot (S - z)$$

In conclusion; when assuming two-dimensional flow and a constant horizontal velocity with depth, the magnitude of the vertical velocity is linearly decreasing with depth.

Bibliography

Andersen, K.K., A. Svensson, S.J. Johnsen, et al. (2006), The Greenland Ice Core Chronology 2005, 15-42 ka. Part 1: Constructing the time scale, *Quaternary Science Reviews* ***25****, 23-24*, 3246-2367.

Bales, R.C., J.R. McConnell, E. Mosley-Thompson, and B. Csatho (2001), Accumulation over the Greenland ice sheet from historical and recent records, *J. Geophys. Res.* ***106****, D24*, 33,813-33,825.

Bamber, J.L., D.J. Baldwin, and S.P. Gogineni (2003), A new bedrock and surface elevation dataset for modelling the Greenland ice sheet, *Ann. Glaciol.* ***37***, 351-356.

Bindoff, N.L., et al. (2007), Observations: Oceanic Climate Change and Sea Level. In: *Climate Change 2007: The Physical Science Basis. Contribution of Working Group I to the Fourth Assessment Report of the Intergovernmental Panel on Climate Change*, Cambridge University Press, Cambridge, United Kingdom and New York, NY, USA.

Bjornsson, H., T. Jonsson, and T. Johannesson (2005), Comment on ‘‘Iceland as a heat island’’ by D. H. Douglass et al., *Geophys. Res. Letters* ***32***, doi:10.1029/2005GL023793.

Bogorodsky, V. V., C. R. Bentley, and P. E. Gudmandsen (1985), *Radioglaciology*, D. Reidel Publishing Company, Dordrecht, Holland.

Buchardt, S.L. (2005), *Dating of the NorthGRIP Ice Core by Inversion of a Simple Flow Model*, Master Thesis, Department of Geophysics, Niels Bohr Institute, University of Copenhagen, Denmark.

Buchardt, S.L., and Dahl-Jensen, D. (2007), Estimating the basal melt rate at NorthGRIP using a Monte Carlo technique, *Ann. Glaciol.* ***45****, 1*, 137-142.

Clarke, T.S., and K. Echelmeyer (1996), Seismic-reflection evidence for a deep subglacial trough beneath Jakobshavns Isbræ, west Greenland, *J. Glaciol.* ***43***, 219-232.

Clausen, H.B., C.U. Hammer, C.S. Hvidberg, D. Dahl-Jensen, J.P. Steffensen, J. Kipfstuhl, and M. Legrand (1997), A comparison of the volcanic records over the past 4000 years from the Greenland Ice Core Project and Dye 3 Greenland ice cores, *J. Geophys. Res.* ***102****, C12*, 26,707-26,723.

Dahl-Jensen, D., N.S. Gundestrup, K. Keller, S.J. Johnsen, S.P. Gogineni, C.T. Allen, T.S. Chuah, H. Miller, S. Kipfstuhl, and E.D. Waddington (1997), A search in north Greenland for a new ice-core drill site, *J. Glaciol.* ***43****, 144*, 300-306.

Dahl-Jensen, D., Dahl-Jensen, T., and N. Gundestrup (2001), Earthquakes and Ice Cores Point to Wet Feet at NorthGRIP, Greenland, Poster.

Dahl-Jensen, D., N. Gundestrup, S. P. Gogineni, H. Miller (2003), Basal melt at NorthGRIP modeled from borehole, ice-core and radio-echo sounder observations, *Ann. Glaciol.* ***37***, 207-212.

Dansgaard, W., and S.J. Johnsen (1969), A flow model and a time scale for the ice core from Camp Century, Greenland, *J. Glaciol.* ***8****, 53*, 215-223.

Dethloff, K., et al. (2002), Recent Greenland Accumulation Estimated from Regional Climate Model Simulations and Ice Core Analysis, *J. Climate* ***15****, 19*, 2821–2832.

Dixon, T.H., eds. (1995), SAR interferometry and Surface Change Detection, Report of a Workshop held in Boulder, Colorado, February 3-4, 1994.

Ekholm, S. (1996), A full-coverage, high-resolution, topographic model of Greenland, computed from a variety of digital elevation data, *J. Geophys. Res.* ***101****, B10*, 21,961-21,972.

Ekholm, S., and K. Keller (1998), Unusual surface morphology from digital elevation models of the Greenland ice sheet, *Geophys. Res. Letters* ***25****, 19*, 3623-3626.

Fahnestock, M., R. Bindschadler, R. Kwok, and K. Jezek (1993), Greenland Ice Sheet Surface Properties and Ice Dynamics from ERS-1 SAR Imagery, *Science* ***262***, 1530-1534.

Fahnestock, M., W. Abdalati, I. Joughin, J. Brozena, and P. Gogineni (2001a), High Geothermal Heat Flow, Basal Melt, and the Origin of Rapid Ice Flow in Central Greenland, *Science* ***294***, 2338-2342.

Fahnestock, M.A., I. Joughin, T.A. Scambos, R. Kwok, W.B. Krabill, and S. Gogineni (2001b), Ice-stream-related patterns of ice flow in the interior of northeast Greenland, *J. Geophys. Res* ***106,*** *D24*, 34,035-35,045.

Fujita, S., and S. Mae (1994), Causes and nature of ice-sheet radio-echo internal reflections estimated from the dielectric properties of ice, *Ann. Glaciol.* ***20***, 80-86.

Gogineni, S., D. Tammana, D. Braaten, C. Leuschen, T. Akins, J. Legarsky, P. Kanagaratnam, J. Stiles, C. Allen, and K. Jezek (2001), Coherent radar ice thickness measurements over the Greenland ice sheet, *J. Geophys. Res.* ***106***, *D24*, 33,761-33,772.

Hammer, C.U. (1980), Acidity of polar ice cores in relation to absolute dating, past volcanism, and radio-echoes, *J. Glaciol.* ***25,*** *93*, 359 - 372.

Hempel, L., F. Thyssen, N. Gundestrup, H.B. Clausen, and H. Miller (2000), A comparison of radio-echo sounding data and electrical conductivity of the GRIP ice core, *J. Glaciol.* ***46***, 154, 369-374.

Huybrechts, P. (1996), Basal temperature conditions of the Greenland ice sheet during the glacial cycles, *Ann. Glaciol.* ***23***, 226-236.

Iken, A., K. Echelmeyer, W. Harrison, and M. Funk (1993), Mechanisms of fast flow in Jakobshavns Isbræ, West Greenland, Part I, Measurements of temperature and water level in deep boreholes, *J. Glaciol.* ***39***, 15-25.

Jacobel, R.W., and S.M. Hodge (1995), Radar internal layers from the Greenland summit, *Geophys. Res. Letters* ***22,*** *5*, 587-590.

Johnsen, S. J., D. Dahl-Jensen, W. Dansgaard, and N. Gundestrup (1995), Greenland palaeotemperatures derived from GRIP borehole temperature and ice core isotope profiles, *Tellus* ***47B***, 624–629.

Joughin, I., R. Kwok, and M. Fahnestock (1998), Interferometric Estimation of the Three-Dimensional Ice-Flow Velocity Vector Using Ascending and Descending Passes, *IEEE Trans. Geosc. Remote Sensing,* ***36,*** *1*, 25-37.

Joughin, I., M. Fahnestock, D. MacAyeal, J.L. Bamber, and P. Gogineni (2001), Observation and analysis of ice flow in the largest Greenland ice stream, *J. Geophys. Res.* ***106****, D24*, 34,021-34,034.

Joughin, I., W. Abdalati, and M. Fahnestock (2004), Large fluctuations in speed on Greenland's Jakobshavn Isbræ glacier, *Nature* ***432****, 7017*, 608-610.

Layberry, R.L. and J.L. Bamber (2001), A new ice thickness and bed data set for the Greenland ice sheet. 2. Relationship between dynamics and basal topography, *J. Geophys. Res. 106, D24*, 33,781-33,788.

Leftwich, T.E., K. van der Veen, and R.R. von Frese (2007), Crustal geothermal controls on ice sheet dynamics of Greenland, AGU 2007, C41A-0320.

Lemke, P., et al. (2007), Observations: Changes in Snow, Ice and Frozen Ground. In: *Climate Change 2007: The Physical Science Basis. Contribution of Working Group I to the Fourth Assessment Report of the Intergovernmental Panel on Climate Change.* Cambridge University Press, Cambridge, United Kingdom and New York, NY, USA.

Meehl, G.A., et al. (2007), Global Climate Projections. In: *Climate Change 2007: The Physical Science Basis. Contribution of Working Group I to the Fourth Assessment Report of the Intergovernmental Panel on Climate Change*. Cambridge University Press, Cambridge, United Kingdom and New York, NY, USA.

Millar, D.H.M. (1981), Radio-echo layering in polar ice sheets and past volcanic activity, *Nature* ***292***, 441-443.

Mosegaard, K., and A. Tarantola (1995), Monte Carlo sampling of solutions to inverse problems, *J. Geophys. Res.* ***100****, B7*, 12,431-12,447.

Mosegaard, K., and M. Sambridge (2002), Monte Carlo analysis of inverse problems, *Inverse Problems* ***18***, R29-R54.

Mosegaard, K., and A. Tarantola (2002), Probabilistic Approach to Inverse Problems. In: *International Handbook of Earthquake & Engineering Seismology (Part A)*, Academic Press, Elsevier, San Diego, USA.

Mote, T.L (2007), Greenland surface melt trends 1973–2007: Evidence of a large increase in 2007, *Geophys. Res. Letters* ***34***, doi:10.1029/2007GL031976.

North Greenland Ice Core Project members (2004), High resolution record of Northern Hemisphere climate extending into the last interglacial period, *Nature **431***, 147-151.

Oerlemans, J. (1984), Numerical experiments on large-scale erosion, *Z. Gletscherkd. Glazialgeol. **20***, 107-126.

Paterson, W.S.B (2001), *The Physics of Glaciers*, 3. Ed., Butterworth-Heinemann, Oxford, UK.

Pattyn, F. (2003), A new three-dimensional higher-order thermomechanical ice sheet model: Basic sensitivity, ice stream development, and ice flow across subglacial lakes, *J. Geophys. Res. **108**, B8*, doi: 10.1029/2002JB002329.

Pritchard, M.E. (2006), InSAR, a tool for measuring Earth's surface deformation, *Physics today **59**, 7*, 68-69.

Rasmussen, S.O., B.M. Vinther, H.B. Clausen, and K.K. Andersen (2007), Early Holocene climate oscillations recorded in three Greenland ice cores, *Quaternary Science Reviews **26***, 1907-1914.

Reeh, N., S.J. Johnsen, and D. Dahl-Jensen (1985), Dating the Dye 3 Deep Ice Core by Flow Model Calculations, In: *Greenland Ice Cores: Geophysics, Geochemistry and the Environment, Geophysical Monograph **33***, American Geophysical Union, Washington DC, USA.

Reeh, N. (1988), A Flow-line Model for Calculating the Surface Profile and the Velocity, Strain-rate, and Stress Fields in an Ice Sheet, *J. Glaciol. **34**, 116*, 46-54.

Rignot, E., and P. Kanagaratnam (2006), Changes in the velocity structure of the Greenland Ice Sheet, *Science **311***, 986-990.

Steen-Larsen, H.C. (2007), *A General Procedure to Infer Surface and Basal Mass Balance from Internal Layering in an Ice Sheet and an Application to the Greenland Ice Sheet*, Master Thesis, Department of Geophysics, Niels Bohr Institute, University of Copenhagen, Denmark.

Summerfield, M.A. (1991), *Global Geomorphology*, Pearson Education Limited, Edinburgh, UK.

Tarantola, A. (2005), *Inverse Problem Theory and Methods for Model Parameter Estimation*, SIAM, Philadelphia, USA.

Taylor, J.R. (1997), *An Introduction to Error Analysis: The Study of Uncertainties in Physical Measurements,* 2. Ed, University Science Books, Sausalito, California.

Truffer, M., and K.A. Echelmeyer (2003), Of Isbræ and Ice Streams, *Ann. Glaciol.* ***36****, 1*, 66-72.

van der Veen, C.J., T. Leftwich, R. von Frese, B.M. Csatho, and J. Li (2007), Subglacial topography and geothermal heat flux: Potential interactions with drainage of the Greenland ice sheet, *Geophys. Res. Letters* ***34***, doi:10.1029/2007GL030046.

Vinther, B.M., H.B. Clausen, S.J. Johnsen, S.O. Rasmussen, K.K. Andersen, S.L. Buchardt, D. Dahl-Jensen, I.K. Seierstad, M.-L. Siggaard-Andersen, J.P. Steffensen, and A. Svensson (2006), A synchronized dating of three Greenland ice cores throughout the Holocene, *J. Geophys. Res.*, DOI: 10.1029/2005JD006921.

Waelbroeck, C., L. Labeyrie, E. Michel, J.C. Duplessy, J.F. McManus, K. Lambeck, E. Balbon, and M. Labracherie (2002), Sea-level and deep water temperature changes derived from benthic foraminifera isotopic records, *Quaternary Science Research* ***21***, 295-305.

Walker, M.J.C., S. Björck, J.J. Lowe, L.C. Cwynar, S. Johnsen, K.-L. Knudsen, B. Wohlfarth, and INTIMATE group (1999), Isotopic 'events' in the GRIP ice core: a stratotype for the Late Pleistocene, *Quaternary Science Reviews* ***18***, 1143-1150.

Weertman, J. (1957), On the sliding of glaciers, *J. Glaciol.* ***3***, 33-38.

Zwally, H.J., W. Abdalati, T. Herring, K. Larson, J. Saba, and K. Steffen (2002), Surface Melt-Induced Acceleration of Greenland Ice-Sheet Flow, *Science* ***297***, 218-222.